# CryoEM Methods: Beam-Induced Motion Attenuation and Selective Particle Capture with Carbon Nanotubes

**Inauguraldissertation**
zur
Erlangung der Würde eines Doktors der Philosophie vorgelegt der
Philosophisch-Naturwissenschaftlichen Fakultät der Universität Basel

von

Christopher John Borsa

2020

Genehmigt von der Philosophisch-Naturwissenschaftlichen Fakultät
auf Antrag von

Prof. Dr. Jan Pieter Abrahams

Prof. Dr. Henning Stahlberg

Dr. Wai Li Winnie Ling

Basel, Oktober 13 2020

Prof. Dr. Martin Spiess

# Acknowledgements

Firstly, I would like to thank Jan Pieter Abrahams for providing me with the opportunity the join his group at the Paul Scherrer Institute (PSI) and allowing me the scientific freedom in taking on this project. If not for your trust, this work would not have happened, and I would not have gained the valuable experience and knowledge in electron microscopy of which I hope to further.

The writing of this thesis would have been impossible if not for the technical and moral support of both Elisabeth Agnes Müller Gubler and Michel Steinmetz. While starting to write my thesis during the throes of a pandemic, I certainly had some trepidation. Your guidance and faith in my abilities was paramount, I cannot thank you both enough.

Many different laboratories at the PSI directly contributed to this project. Celestino Padeste graciously offered his technical expertise upon the start of my work and continued to do so well into my later experiments, thank you. I would like to thank Christof Schneider for his early help and encouragement during the start of this project. I am very grateful to Thomas Rohrbach for performing the synthesis of the binding ligand, much of my work hinged around your efforts. During later characterization, Thomas Jung and Mehdi Heydari were instrumental in their support.

This journey could not have happened without my fellow group members at the PSI and University of Basel: Tim Grüne, Tatiana Latychevskaia, Pooja Thakkar, Thorsten Blum, Emiliya Poghosyan, Inayathulla Mohammed, Jonas Heidler, Jinghui Luo, Jinming Wu, Hongzhi Wang, Hung Tri Tran, Kai Alexander Schmitz and Eric van Genderen. Additionally, I would like to thank Petr Skopinstev, Ching-Ju Tsai, Steffen Brünle, Ved Jaimini Mehta, Agnieszka Malgorzata Olechwier, Filip Karol Pamula, Diane Cécile Barret, Maximilian Wranik, Daniel Frey and Jacopo Marino for their friendship and support during my time at the PSI.

Ludmila Leroy and Benjamin Prünster. We have been through a lot in 2020, and you have both seen me through dark times. Words can't express our experience, nor my gratitude, thank you. Katja Haas and Sean Banks,

you two provided me with unwavering support when I needed it the most, thank you.

To my Mother, Father, Sister and family back in Canada. I would have never been able to accomplish any of this if it were not for your love and support.

# Contents

# List of Figures

# List of Tables

# Acronyms

**ACN** acetonitrile. 68

**APTES** (3–aminopropyl)triethoxysilane. 27, 28

**BE** binding energy. 74, 75

**CCD** charge-coupled device. 2

**CMOS** complementary metal–oxide–semiconductor. 2

**CNT** carbon nanotube. 22, 24, 26

**cryoEM** cryogenic electron microscopy. vii, viii, 2, 3, 5–7, 10, 12, 13, 26, 30, 32, 42, 50, 51, 60, 79, 80

**CTF** contrast transfer function. 36, 37, 44, 47

**CVD** chemical vapour deposition. 22, 26

**DIPEA** N,N-diisopropylethylamine. 68

**DMF** dimethylformamide. 31, 63, 68, 71

**DNA** deoxyribonucleic acid. 61

**EDX** energy dispersive X-ray spectroscopy. 27, 29

**EM** electron microscope. 3, 36

**GFP** green fluorescent protein. 65–67, 71, 77, 86

**HCl** hydrochloric acid. 68

**HEPES** (4–(2–hydroxyethyl)–1–piperazineethanesulfonic acid). 64, 65

**HIS-tag** polyhistidine-tag. ix, 60, 65–67, 71, 77, 79

**HOPG** highly oriented pyrolytic graphite. 71

**I-TASSER** Iterative Threading ASSEmbly Refinement. ix, 65, 66

**LiOH** lithium hydroxide. 68

**MeOH** methanol. 68

**$MgCl_2$** magnesium chloride. 42

**NaCl** sodium chloride. 42

**NHS** N–hydroxysuccinimide. ix, 62, 63

**NMR** nuclear magnetic resonance. 63, 68, 69, 74, 76, 79, 87, 91

**NTA** nitrilotriacetic acid. vi, ix, 60, 63–65, 67, 68, 71–73, 75–77, 79, 87, 91

**NTA–amine** N$\alpha$,N$\alpha$–Bis(carboxymethyl)–L–lysine. 64

**PAGE** polyacrylamide gel electrophoresis. viii, 42–44

**PSI** Paul Scherrer Institute. iii, 25, 65, 68

**pyrene–NHS** 1–pyrenebutyric acid N–hydroxysuccinimide ester. 63, 64

**RBM** radial breathing mode. 26

**RSF** relative sensitivity factor. x, 74

**SDS** sodium dodecyl sulfate. viii, 26, 27, 42–44, 61

**SEC** size exclusion chromatography. 43

**SEM** scanning electron microscope. 3, 26

**STAR** self-defining text archive and retrieval. 47, 83, 84

**SWCNT** single walled carbon nanotube. v–ix, 2, 12–15, 17–22, 24–32, 35, 36, 38–40, 42–47, 50, 52, 54–58, 60–68, 71, 76, 79, 80

**TCEP** tris(2-carboxyethyl)phosphine. 42

**TEM** transmission electron microscope. v, 1, 2, 26–29, 36, 63

**THF** tetrahydrofuran. 68

**UPLC** ultra performance liquid chromatorgraphy. 68

**XPS** X-ray photoelectron spectroscopy. 63, 71, 72, 74, 76, 77, 80

# Chapter 1

# CryoEM

The term biology was first used by Carl Linneaus in his 1735 work *Bibliotheca Botanica*, which provided the first modern classification of living organisms. After several hundred years, biology has grown from its taxonomical roots and with the embrace of modern technology is probing the very depths of the atomic origins of living entities as to provide a first principle understanding of the molecular machinery responsible for all hierarchical life. Today, the study of biological molecules at near atomic resolution is known as structural biology.

The first protein diffraction pattern of the crystallized enzyme pepsin was captured with X-rays in 1934 [1], but it was not till 1958 that the complete 3D protein structure of myoglobin was solved [2]. These studies marked the beginning of structural biology and ushered in a new era in which X-ray crystallography was the principle methodology for which protein structures were explored. The transmission electron microscope (TEM) was subsequently developed after the discovery of X-rays. Unlike the first X-ray structures solved by diffracting protein crystals, the initial structures produced with a TEM were obtained through the averaging of individual images of protein particles fixed in contrast enhancing heavy metal stains [3]. In 1975, 2D purple membrane crystals were diffracted within a TEM to produce the first protein structure obtained via electron crystallography [4].

Throughout the past century crystallography using X-rays and electrons was the predominant method in which to solve protein structures. Protein crystals provide a natural means of signal amplification. By coordinating identical molecules into a confined volume, the superimposed signal coming from each protein particle will outweigh erroneous signals manifested from the surrounding buffer thus increasing signal to noise ratio coming from the protein. These enhanced signal to noise ratios make crystallography a potent tool but come with the difficulty of producing protein crystals which repre-

sents the biggest bottleneck within the protein crystallography pipeline.

The difficulties in obtaining large, well diffracting protein crystals provided the impetus to re-explore single particle averaging in conjunction with newly discovered cryogenic plunging methods rather than previously used metal staining [5], [6]. During this time, Henderson published his seminal paper comparing the differences in radiation damage on biological specimens from electrons, neutrons and X-rays [7]. Henderson argued that electrons were superior in terms of their ability to elastically interact with matter when compared to amount of radiation damage ensued. While electrons were deemed to be superior to X-rays and neutrons, structures that were attained during this period suffered from resolutions well below theoretical limits. At that time charge-coupled device (CCD) cameras were used as an alternative to traditional film and it was proposed that direct electron detector utilizing complementary metal–oxide–semiconductor fabrication methods and specifically optimized for use in TEMs could increase both pixel number and readout speed and thus improve resolutions [8].

By 2012 three direct electron detector prototype designs were developed [9]. The exceptionally high frame rates of these devices made it possible to observe beam-induced motions that produced a drum-like displacement of the vitreous ice sheet [10]. The subsequent development and usage of motion correction alignment algorithms and phase plates have led to astonishing improvements in resolution providing 1.2Å structures [11]. The accounting of beam-induced motion played a large role in the advancement of cryogenic electron microscopy (cryoEM), propelling it to a bona fide tool capable of near atomic resolution studies.

While accounted for, beam-induced motion still remains one of the biggest causes of information loss in cryoEM [12] and has been the subject of ongoing research that has led to the development various different TEM grid technologies [13]–[16]. This thesis investigates the use of single walled carbon nanotubes as a support network for the attenuation of beam-induced motion and selective particle capture of cryoEM specimens.

# Chapter 2

# Beam-Induced Motion

Within the electron microscopy community it is common knowledge that electrically insulating specimens manifest deleterious charging effects and beam-induced movement which impede analysis. In the second edition of the textbook *Scanning Electron Microscopy and X-Ray Microanalysis* it is written that "Nonconducting samples invariably need some sort of treatment before they can be examined" [17].

The treatment of electrically insulating specimens for EM consists of coating the specimen in a conductive material such as gold or carbon and is depicted in Figure 2.1 whereby a spider is sputter coated in gold for scanning electron microscope (SEM) imaging. These conductive coatings have been long known to prevent charging of the sample by allowing trapped charges to migrate away from the irradiated area. Such conductive films are standard practice in SEM and definitively prevent burning while anecdotally prevent beam-induced motion of insulating specimens. While conductive coatings prevent beam-induced effects in many EM samples, the physiologic, and high-resolution nature of structural biology specimens make such interventions difficult if not impossible.

Beam induced motion was first observed in early electron diffraction experiments with 2D purple protein crystals mounted on paraffin[18] and while these movements hamper analysis, crystalline diffraction patterns are largely invariant to specimen movement. The same cannot be said for cryoEM data where weakly contrasting per-particle images are individually averaged throughout the entire exposure, with any drift serving to obfuscate and skew the signal coming from the specimen. With beam-induced motion having detrimental consequences specifically in cryoEM, it has only recently been explicitly studied by structural biology groups. The following chapter will briefly describe the known origins of beam-induced motion within the context of cryoEM.

Figure 2.1: A spider sputter-coated in gold in preparation for SEM imaging [19].

## 2.1 CryoEM Specimens

Modern day cryoEM utilizes standard 3mm TEM grids in conjunction with perforated support films seen in Figure 2.2a. TEM grids are made from a wide variety of highly conductive metals such as gold, copper, molybdenum, and many others. Support films are fixed atop the grid and typically are comprised of carbon or gold, although less common alternatives such as silicon oxide and other silicon derivatives do exist. These films provide a rigid structure for protein solutions to adhere to when the applied to the grid as is seen in Figure 2.2a. Traditional support films such as *lacy* or *holey* carbon consist of amorphous carbon that is treated with acid as to randomly open sections within the amorphous carbon layer. Nowadays it is common practice to use support films with engineered perforations with uniform diameters and spacing as seen in Figure 2.2a. Such engineered films provide an inherently predictable platform for tuning preparatory protocols as the protein meniscus layer will be of identical size and shape. Machined support films also streamline data collection as the regions of interest can be automatically mapped based on repeating features within the film.

CryoEM samples are typically prepared using the unassuming methodologies pioneered by Jacques Dubochet [5]. Prior to protein application, TEM grids are subjected to ultra-violet or plasma treatments that remove superficial hydrocarbons rendering its surface hydrophilic. After pre-treatment protein solution is pipetted onto the treated grid and blotting papers draw away excess buffer to form a meniscus within the openings of the support film. Immediately after blotting, the grid is rapidly plunged into liquid ethane thereby vitrifying and fixing the meniscus layer in place as is illustrated in Figure 2.2.

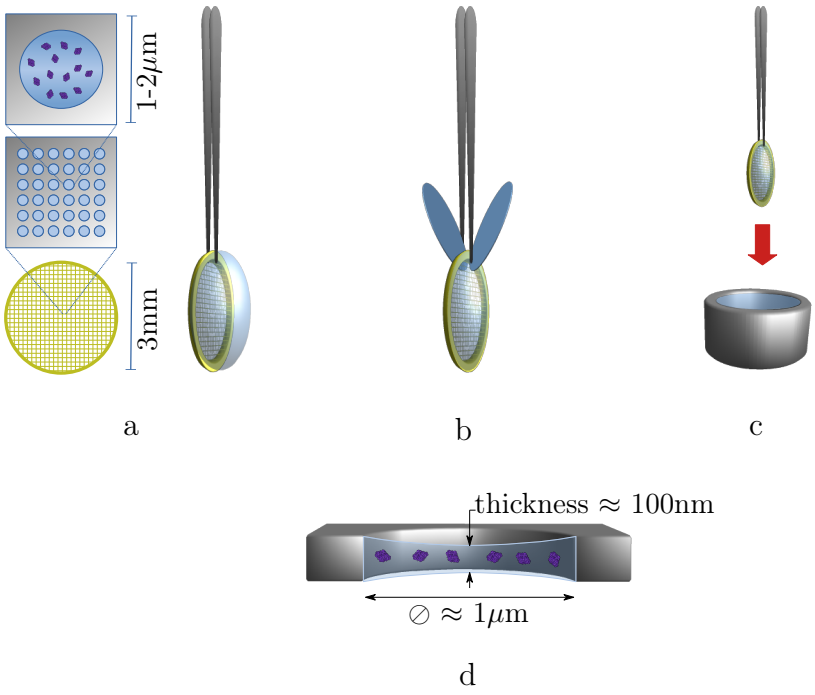


Figure 2.2: cryoEM specimen and plunging schematic. a) Initial protein application. b) Grid blotting. c) Plunging in liquid ethane. d) Typical meniscus of vitreous protein buffer.

## 2.2 Beam-Induced Effects

At present there exists no complete understanding of beam induced motion or charging, and while not explicitly linked to one another, these two phenomenon are often connected in context and researched simultaneously. Without empirical models for motion or charging, the current body of knowledge is largely based on phenomenological findings. The following section briefly describes 5 distinct epochs of beam-induced charging and motion throughout a typical sample irradiation from the perspective of the current literature and experimental data.

The first epoch is represented by a specimen prior to irradiation in a neutral charge state. This intial condition is depicted in Figure 2.3(I) which shows a single section of a Quanti-Foil ® film. The initial irradiation of the sample marks the second epoch where low energy secondary electrons are ejected from the beam's footprint. These electrons are redistributed on the sample outside of the beam footprint creating a net positive charge within the beam area [20]. Dr. John Berrimen is widely cited as the first person to discover this effect thus many refer to such phenomenon as the "Berriman effect" or "Berriman phases". In contrast, negative static charges are known as "inverse Berriman phases". Charging of the sample takes place almost instantaneously upon irradiation, with appreciable charge intensities being measured at fluences of $10^{-3}$ $e^{-}/\text{Å}^{2}$ [21]. Additionally, Berriman phases within the beam spot have been estimated to have a potentials of approximately $1V$. The inverse Berriman phases surrounding the spot have an approximate potential of $-0.4V$ with charges having a radial intensity degradation of approximately $1/r$ where $r$ is the radius of the primary irradiation area. Berriman phases both in and outside the beam footprint are known to be static within the sample, only being neutralized with additional radiation. The third irradiation epoch seen in Figure 2.3(III) is marked by the onset of a rapid vertical acceleration in which the specimen forms a hemispherical cavity or drumming motion. This movement was first discovered in 2012 with the advent of high frame rate detectors and reaffirmed that beam-induced motion was largely responsible for the lack of resolution which plagued first generation cryoEM structures [22]. With a beam diameter of 1.6µm, the central region of the sample can translate up to 150–250Å producing a radius of curvature of 12–25µm. The direction of these translations is random with respect to the sample plane and hence not a direct consequence of the beam momentum. Figure 2.3 displays the average lateral particle speed of 5nm gold fiducials that were nominally vitrified and imaged with a typical electron dose. Each region of the plot is coloured and labelled according to

its corresponding irradiation epoch, details on collection of these data are presented in Chapter 4. At roughly 35 $e^{-}/\text{Å}^{2}$ the rapid initial motion of the specimen dampens to a steady state shown in the fourth epoch. This region displays non uniform acceleration or vibrations that are superimposed throughout this constant speed region. The possibility of molecular radicals generated by radiolysis has been postulated as one causes of beam-induced motion [23] and while anecdotal, it does seem plausible that the vibrations seen in this region are the tell-tale of gaseous entities escaping from the ice surface. The fifth and final irradiation epoch is denoted by another large progressive particle acceleration only seen at large fluences and is most likely the result of sample sublimation.

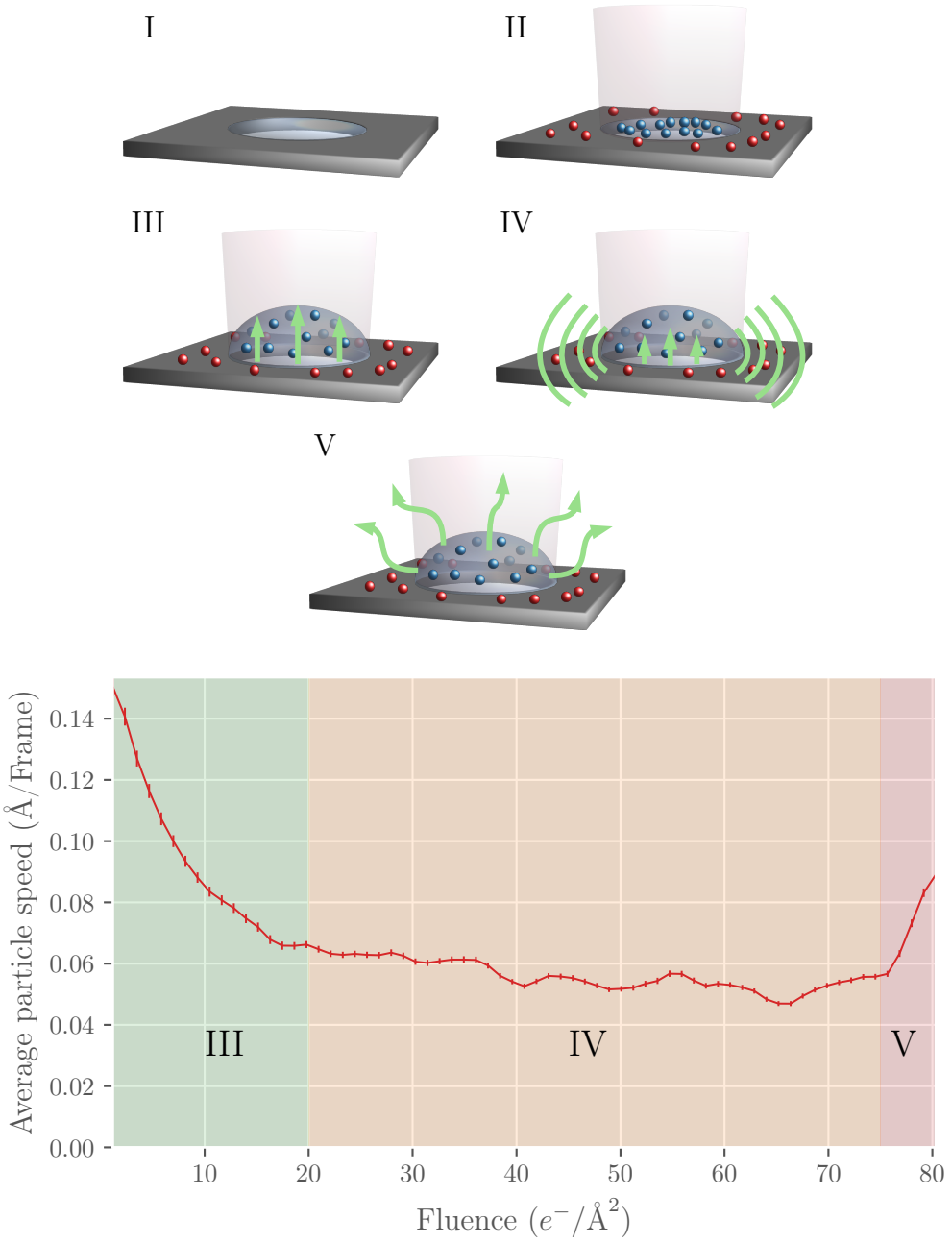


Figure 2.3: cryoEM sample irradiation epochs

## 2.3 Beam-Induced Motion Interventions

With an overview of the phenomena seen throughout in a typical cryoEM exposure, it can be seen there necessarily exists an interplay between various mesoscopic forces within vitrified cryoEM specimens under irradiation, these forces being: electrical, mechanical, thermal and physiochemical. While authors have began to account for charge potentials and physical motion of specimens, there has yet been an exhaustive dimensional analysis via Rayleigh's method or the Buckingham $\pi$ theorem as to parse out the possible driving forces within the system.

Dr. Robert Glaeser, an early pioneer in beam-induced motion research was the first to argue that specimen motion could be the result of Coulomb dipole forces resulting from Berriman's phases [24]. The concept of controlling motion through a charge limiting mechanism was realized with the development of an integrated all gold membrane-grid concept now commercially known as UltrAuFoil® [13]. UltrAuFoil® grids have been shown to decrease the average root-mean-square particle displacement by half, and are widely used in high resolution cryoEM studies. As gold is highly conductive at cryogenic temperatures it is thought that increased conductivity will result in reduced specimen charging and thus, beam-induced motion. It is also supposed that UltrAuFoil® grids reduce beam-induced motion by preserving tension in the ice sheet during plunging. As the grid is composed of a single element, it will not suffer from non-uniform cooling due to materials with differing thermal coefficients. Mechanical studies of UltrAuFoil® grids revealed that their gold foils are less mechanically rigid than nominal amorphous carbon and thus rule out movement reductions on account of mechanical stabilization [25]. Recent theoretical studies of cooling and vitrification rates have indicated that even all gold UltrAuFoil® will suffer from non-homogeneous shrinking as a result of thermal mass differences between the membrane and grid bars. Upon plunging, the thin membrane will cool quicker as result of having less thermal mass than the grid bars which remain cool and uncontracted initially placing the membrane under tension. This uneven cooling results in ice formation prior to the grid bars fully cooling/shrinking, thus the sheet will be compressed by the grid once reach its final thermal state. It's argued that radiation induced creep of ice in a compressed state will result in the formation of a concavity as means to reduce stored compressive energy [26].

Although not widely used, additional grid membrane materials utilized for further prevention of beam-induced motion. These materials almost exclusively consist of carbon allotropes such as graphene [14]–[16], graphene

oxide [27], [28] and buffer dispersed carbon nanotubes [29]. Such materials are both highly electrically and thermally conductive and thus aid in the prevention of charge build up and heat dissipation during vitrification, they also have low atomic density providing minimal electron scattering and signal attenuation. Said membrane materials are suspended within the perforations of the primary support film and providing a physical support on which proteins to directly vitrified. Such physical support is sometimes necessary for larger membrane proteins which contain flexible domains.

## 2.4 The Ideal Sample Support

With all that is known on beam-induced effects, what comprises the optimal sample support? From both the physical phenomena previously discussed and beneficial affects seen in state of the art grid technologies the following attributes constitute the ideal sample support:

- Electrically conductive: Prevent charging.
- Mechanically rigid: Mechanically dampen motion.
- Minimal atomic density: Minimal disruption of image signal.
- Non-planar geometry: Minimize preferential particle orientation.
- Chemically amenable: Attachment of chemically selective probes.

With insights taken from the criteria listed above, it becomes apparent that utilizing support films consisting of single walled carbon nanotubes would address all the aforementioned points. SWCNTs are among the most electrically conductive materials presently known, they are also one of the most thermally conductive materials. Unlike a monolayer graphene layer, SWCNTs have axial thickness which provide a substantial area moment to resist sample bulging. Like graphene, the atoms with SWCNTs are bound via $sp^2$ bonds, the strongest chemical bond in nature, thus providing enhanced geometric and material strength with which to dampen beam induced movement. Preferential particle orientation is an issue with cryoEM were particles lie in a single orientation thus skewing the overall structure with images of these orientations, this is a common issue when utilizing fully continuous support films such as amorphous carbon and graphene. Utilizing cylindrical shaped SWCNTs in theory may help prevent preferential orientations by providing a 360° radial bonding area. With regard to chemical amenability, there presently exists an array of functionalization tools for SWCNTs in which probes with selective binding affinities can be attached.

While SWCNTs have been utilized as a buffer additive that has successfully reduced beam-induced motion there is not yet a protocol or methodology for fabricating a SWCNT network grid that is universally compatible such as now standard UltrAuFoil® or Quanti-Foil® grids. The subsequent chapters of this thesis outline the fabrication, functionalization, and qualification of SWCNT grids for beam-induced motion attenuation and selective particle capture for cryoEM studies.

# Chapter 3

# Sample Support Fabrication

With an understanding that both increasing the electrical conductivity, and structural rigidity of the cryoEM support materials, the beam-induced motions can be attenuated thereby providing higher quality images and ultimately better resolution structures. The reduction of beam induced motion through the use of highly electrically conducting materials. At present the use of gold membranes or UltrAuFoil® grids along with graphene are the most popular alternatives to standard amorphous carbon membranes such as Quanti-Foil® or C-Flat® grids. At project onset it was known that carbon nanotubes are compatible within the protein buffers [29] hence it was sought out to develop a single walled carbon nanotube grid network that could be universally used in a standard cryoEM preparation pipeline with the need to alter native protein buffers. SWCNTs are both highly conductive and their morphology provides them with appreciable mechanical buckling characteristics [30] that are not native to planner films. During the course of project similar works were published [31] and while unfortunate this points towards the value in such concepts. The following sections will first provide a fundamental background as to the physical principals of carbon nanotubes, their handling, and network deposition experiments.

## 3.1 Carbon Nanotubes

Since antiquity, novel materials have continuously shaped humankind; the Stone age, Bronze age, and the Iron age. It has been said that we currently live in the Silicon age and based on the research in the past twenty years, the 21 century might be known as the Carbon age. Of all novel carbon allotropes, fullerenes were the first discovered in the 1980's by Sumio Iijima and Harold Kroto [32], and confirmed previous quantum-chemical predications of a stable 60 carbon icosahedral cage structure [33]. These molecules were given the name "buckyballs" in homage to the architect Buckminster Fuller who popularized geodesic domes in modern architecture.

SWCNTs came to prominence when discovered in 1991 by Iijima and Ichihashi [34], likewise graphene was first isolated and characterized in 2004 by Geim and Novoselov [35]. While these materials have both seen a meteoric rise in their study during the past decades, their development was long in coming and humble in nature. The concept of 2D carbon sheets was first incepted by Wallace as a base case whilst developing tight binding atomic models in 1947 [36], at the time the possible existence of 2D materials was in question as it was thought that reduced dimensional materials were thermodynamically unstable [37]. Throughout the 20th century epitaxial carbon films were studied and referenced as mono-layer or ultra-thin carbon [38]–[40]. However, it was the work of Geim and Novolsev in which mechanical exfoliation was utilized to produce free-standing graphene sheets that allowed the science community to explore this material with great rigour. Similarly, Raduchkevich and Lukyanovich were the first to publish images of 50nm diameter carbon nanotubes in the Soviet Journal of Physical Chemistry in 1952. However, the spectre of the Cold War made it difficult for western science to access Russian research leaving this discovery largely unnoticed [41].

## 3.2 Carbon Nanotube Structure

SWCNTs are an extension of the graphene and fullerene crystal structures whereby a graphene sheet is rolled up along a Bravais lattice vector of the graphene lattice to form a hollow tube. With carbon having six electrons, the $s$ orbital will be completely filled and strongly bound to the nucleus with the outer energy shell consisting of a hybridization of $s$ and $p$ states. These outer energy states give rise to hybrid $sp^2$ covalent C–C bonds ($\sigma$ bonds) that make up the honeycomb lattice. At present, $sp^2$ binding represent the strongest bonds found in nature [42]. Electrons remaining in the half filled $2p$ energy level form delocalized $\pi$ orbitals.

$$\underset{1s}{\uparrow\downarrow}\ \underset{sp^2}{\uparrow}\ \underset{sp^2}{\uparrow}\ \underset{sp^2}{\uparrow}\ \underset{2p}{\uparrow}$$

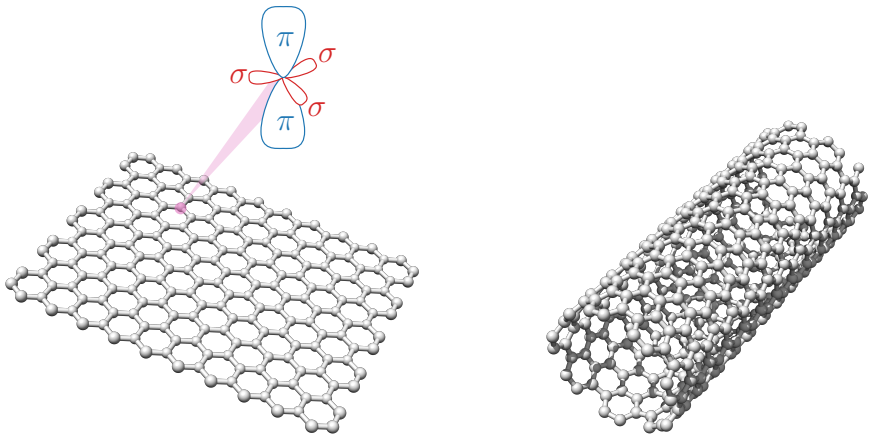


Figure 3.1: Graphene sheet and SWCNT

SWCNTs will drastically vary in length that is often not reported and will vary greatly with different synthesis methods with tubes of up to half a meter length being reported [43]. SWCNT diameters will vary depending on the chirality of their crystal structure which is defined by the roll-up vector $C_h = na_1 + ma_2 = (n, m)$ that connects equivalent sites of a 2D graphene sheet were $n$ and $m$ are integers and $a_1$ and $a_2$ are the primitive graphene lattice vectors. Chiralities of $(n, 0)$ and $(n, n)$ represent the two limiting vectors known respectively as zigzag and armchair structures and are shown in Figure 3.2. SWCNTs will have a diameter that is typically constrained by their chiral vector $C_h$ [44] and can be approximated by Equation 3.1 and is visualized in Figure 3.3, with average diameters of ≈1nm.

$$d(picometers) \approx \ 78.2\sqrt{(n+m)^2 - nm} \tag{3.1}$$

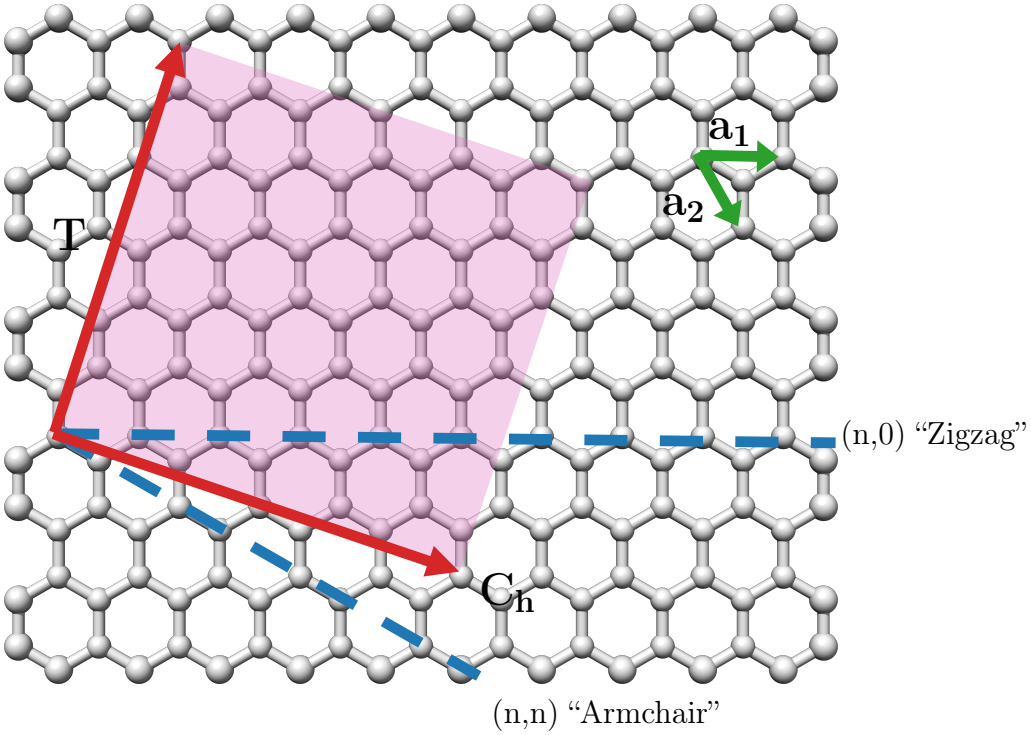


Figure 3.2: Graphene sheet with lattice vectors $a_1$ and $a_2$ in green and roll-up vector $C_h$ in red. Blue dashed lines represent achiral limiting cases $(n, 0)$:zigzag and $(n, n)$:armchair. The translation vector T shown in red represents the axis defining the 1D unit cell of the nanotube, the magenta sheet represents the unfolded unit cell of vectors formed by T and $C_h$.

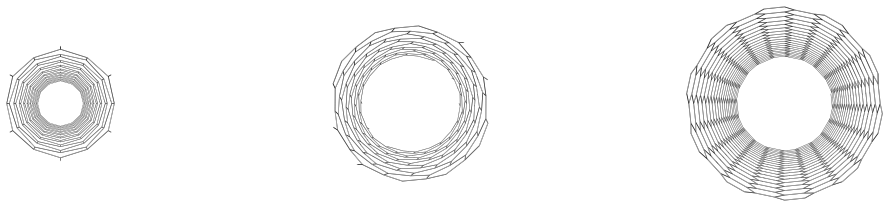

Figure 3.3: SWCNT axial views (from left to right) Metallic-Zigzag $(6-0)$: $\oslash = 0.47$nm, Semiconducting $(10-2)$: $\oslash = 0.87$nm and Metallic-Armchair $(10-10)$: $\oslash = 1.35$nm.

## 3.3 Carbon Nanotube Electrical Conduction Theory

With carbon atoms in SWCNTs having the same electronic states as graphene, the electronic band structures of the two materials share many common characteristics. Graphene's band structure contains six degenerate states or Dirac cones at the corners of the first Brillouin zone that are often referred to as K points. If the unit cell of the SWCNT allows an energy state that crosses one of the above K points, the SWCNT crystal structure will be metallic in nature, otherwise it will be semiconducting. The conduction modality of a SWCNT is determined by its chirality with metallic having $(n-m)/3$ equal to an integer, with all other chiralities being semiconducting. Figures 3.4 through 3.6 illustrate the band structures and density of states for zigzag, armchair and semiconducting SWCNTs.

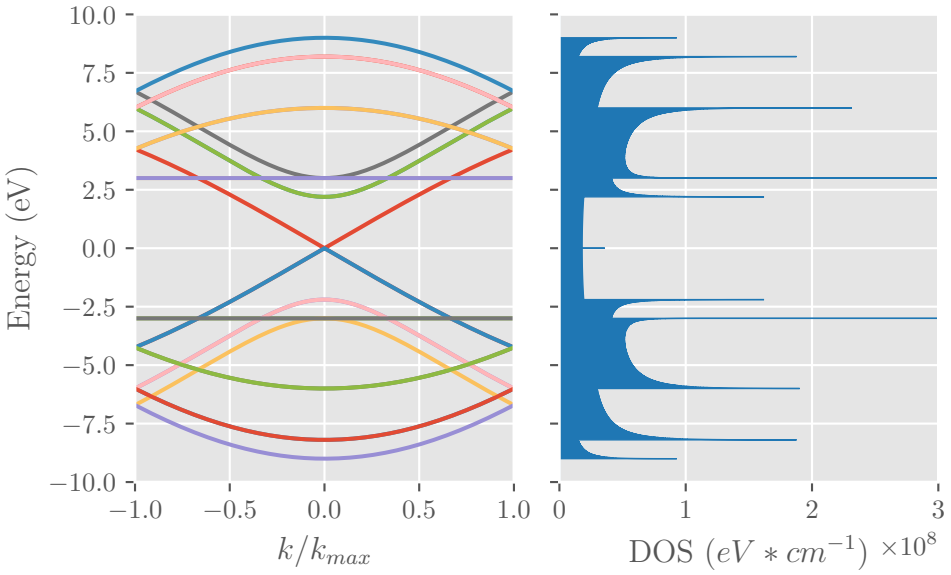


Figure 3.4: Metallic Zigzag $(6-0)$ band diagram (left) and Density of States (right) simulated via tight-binding with CNTbands [45].

The linear regions of the conduction bands or Dirac cones are the most striking feature seen in the both metallic SWCNT and graphene due to their linearity. Equation 3.2 defines the Drude model for direct-current electrical conductivity, where $n$ is carrier density, $q$ is electron charge, $\overline{\tau}$ is average mean free time between collisions and $m^*$ the effective mass of the carrier. Effective

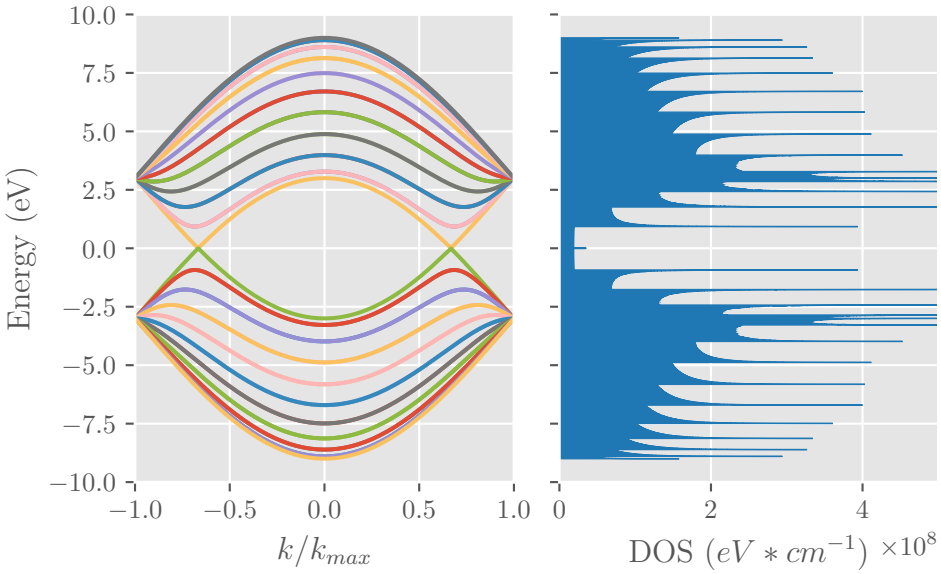


Figure 3.5: Metallic Armchair $(10-10)$ band diagram (left) and Density of States (right) simulated via tight-binding with CNTbands [45].

mass is further defined in Equation 3.3 whereby the second derivative of the electrical dispersion is in the denominator. Thus, materials having a linear conduction band such as metallic SWCNTs and graphene will have carriers with zero rest mass, otherwise known as massless Dirac fermions.

$$\sigma = \frac{nq^2\overline{\tau}}{m^*} \tag{3.2}$$

$$m^* = \frac{\hbar^2}{\left(\frac{d^2E}{dk^2}\right)} \tag{3.3}$$

$$n = \int_{E_C}^{\infty} DOS(E) * f(E)dE \tag{3.4}$$

$$f(E) = \frac{1}{e^{(\varepsilon_i - \mu)/k_bT} + 1} \tag{3.5}$$

At lower temperatures the Fermi distribution (Equation 3.5) provides appreciable carrier concentrations and combined with larger mean free paths (Equation 3.3) measurable amounts of massless Dirac fermions can be theoretically observed. Graphene conductivity experiments carried out by Novolsev and Geim at temperatures of 4°K revealed charge carriers mimicking

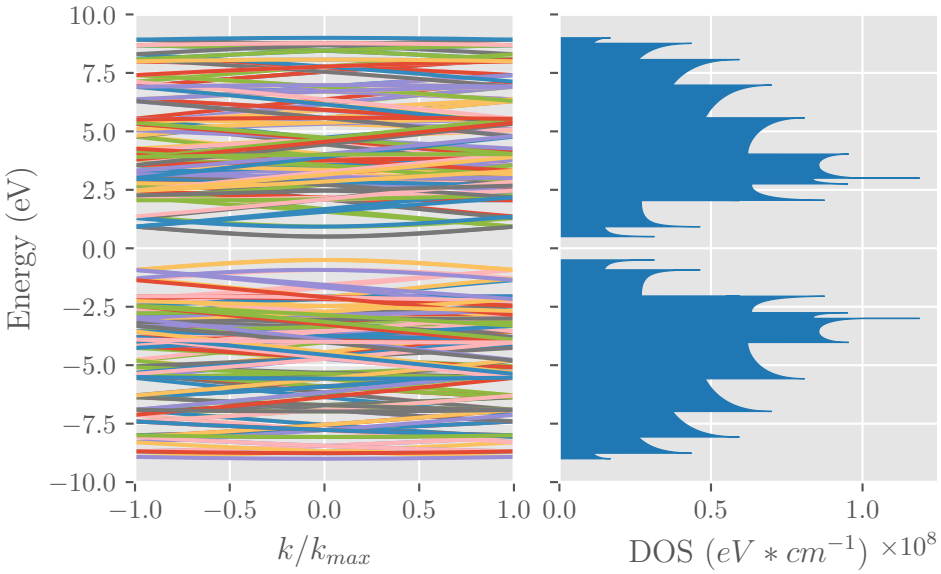


Figure 3.6: Semiconducting $(10-2)$ band diagram (left) and Density of States (right) simulated via tight-binding with CNTbands [45].

relativistic particles with zero rest mass and an effective speed of light of $c^* \approx 106$ m/s [46]; these experiments validated linear band structure predictions previously calculated by Dresselhaus [47]. With exceedingly high carrier mobilities in part due to the linear region of conduction band, the resistivity of both SWCNTs and graphene will be dominated by phonon and defect scattering. Thus, ambient temperature, defects, and intrinsic substrate phonons will play a large part in the measured resistivity of graphene. With free-standing graphene, the effects of intrinsic substrate phonons are reduced which results in lower resistances [48]. The situation with SWCNTs is even more complicated than is the case with graphene, not only will resistivity be dependent on both thermal and substrate properties but also on the intrinsic band structure and the tube-tube crossings within the network of the SWCNT film being measured. The room temperature resistivity of individual SWCNT of unknown chiralities have been measured to be on the order of $10^{-6}$ Ωm ranking them along the most conductive metals [49]. Later temperature dependant resistivity studies on purified metallic and semiconducting SWCNT thick films provided higher resistivities to order of $10^{-1}$ and $10^{-5}$ Ωm for semiconducting and metallic networks respectively [50]. The films in the aforementioned study were black and opaque indicating considerable thickness, and yet had higher resistivities. These resistivities should be

lower with increasing thickness as is the case with typical metals or semiconductors; this highlights the dependence on inter-tube and defect scattering effects, and how they overshadow the native electrical properties of pristine individual materials. Like traditional semiconducting materials, semiconducting SWCNTs exhibit decreasing electrical conductivity with decreasing temperature with metallic SWCNTs being largely temperature invariant.

## 3.4 Carbon Nanotube Synthesis

There exist multiple and ever-expanding methods for growing carbon nanotubes with the two most common being arc-discharge and chemical vapour deposition (CVD). Arc discharge was the first method to produce CNTs and like its name entails, CNTs are produced through plasma discharge between an anode and cathode. Carbon precursor is loaded in either the anode or cathode with the opposing terminal usually consisting of a pure graphite rod, deposition nominally takes place in an inert gas environment. When discharging, high temperature plasmas will sublime the precursor carbon whilst traveling the 1-2mm distance from anode to cathode. This method is known for producing SWCNTs that are longer and straighter than most other methods. CVD is a traditional semiconductor epitaxy method where precursor and carrier gases are passed along a target substrate at reduced pressures and specified temperatures such that atoms from the precursor are deposited on the substrate. To synthesize CNTs via CVD, the target substrate is first seeded with metallic catalyst particles such as nickel, cobalt or iron. Carbon rich precursor gasses such as acetylene or ethylene are passed along the substrate at elevated temperatures of $\approx 700°C$. These gases will decompose along the surface of the nanoparticle and solidify into CNTs growing upward [51]. In this way dense CNT forests can be grown on various substrate materials.

The above methods will grow various different morphologies of CNTs all with differing chirality, diameter and length alongside various catalytic metal contaminants. The use of strong acid etchants removes most catalytic materials with the remaining nominally being fractions of a weight percent. To be utilized as an engineering material, SWCNTs must also be separated by chirality. Chirality sorting is to date a vast field of study with novel methods relying on physical separation methods such as dielectrophoresis, gel column chromatography and density gradient centrifugation [52]. These physical methods in large rely on the already mentioned fact that chirality will influence the diameter of a SWCNT and thus its density. By sorting differential densities of tubes, chirality selection can be achieved as seen in Figure 3.7. It can also be seen in Figure 3.7 that lighter semiconducting tubes comprise the uppermost supernatant and refract magenta light when in solution. The second supernatant layer in blue is made up of metallic SWCNTs with remaining darker layers being comprised of bundled tubes of mixed chirality. Current state of the art methods in SWCNT rely on selective binding of either polymers or DNA whereby the physical methods already discussed can be utilized with greater fidelity than with raw non-conjugated tubes. These novel methods not only make definitive selection for chirality

possible, but also handedness [53].

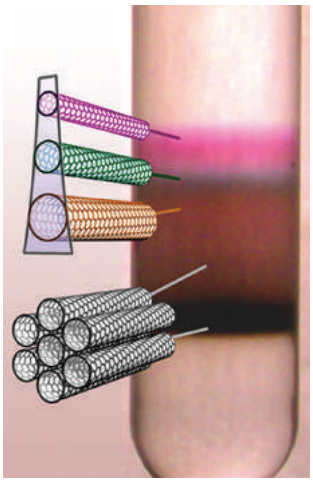

Figure 3.7: Multiple SWCNT species separated with density gradient centrifugation [54].

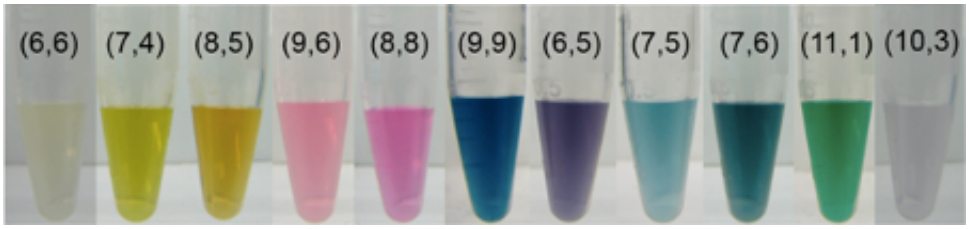


Figure 3.8: Various SWCNT species separated via DNA conjugation [53].

## 3.5 Carbon Nanotube Handling

As CNTs are a relatively novel material, little is known as to the long-term health affects this material can impose. However, animal CNT exposure studies which serve as benchmarks for predicting potential human risk have shown that exposure to this material has adverse pulmonary effects when inhaled. In response, governing bodies such as Schweizerische Unfallversicherungsanstalt (SUVA) in Switzerland and the National Institute for Occupational Safety and Health (NIOSH) in the United States have respectively established an "indicative limit value" of 0.01 fiber/mL, and 8-hour time weighted average (TWA) exposure limit of 1 $\mu g/m^3$ [55], [56]. In order to mitigate the health risks of CNT inhalation, specific technical, organizational and personal protective actions are to be taken when working with even the small amounts of CNTs called for in this experiment. These regulations make working with bulk, dry SWCNT powders very difficult and require the use of specified nanoparticle powder rooms where lab workers must dawn disposable Tyvek overalls and full face respirators as can be seen in Figure 3.9 which was taken during nanoparticle safety training.

Figure 3.9: Nanoparticle safety training at Lausanne University Hospital

While the regulations concerning SWCNTs are conservative, they do not impact the research within this project greatly. The amount of SWCNTs

needed to cover on TEM grid can be approximated as tens of nanograms, and thus handling large quantities of SWCNTs in bulk powder is somewhat unnecessary as commercially available chirality sorted and dispersed solutions of SWCNTs are commercially available. The use of SWCNT dispersions was approved for experimentation at the PSI with several specific pre-emptive safety measures to abide by. Technical measures include the use of fume hoods for drop casting and blotting. As well, all SWCNT contaminated waste, including nitrile gloves are to be first sealed in air-tight "mini-grip" bags, before being disposed of in regular laboratory waste. Organizational protective measures include keeping facility managers and personnel working within close proximity informed as to the nature of working with SWCNTs and providing proper personal protective equipment when necessary. Protective measures include the use of P3 filter masks and nitrile gloves.

## 3.6 SWCNT TEM Grid Fabrication

While SWCNT-TEM grids are not at present widely used in within the TEM community at large, there has been limited research into their development. The most notable was the work of Jiang whom developed a method of synthesizing SWCNT films from CVD grown forests [57], [58]. While very promising this work could not be easily currently replicated in part due to health and safety concerns of working with bulk tubes. Additional issues include large heterogeneity of tube diameters and chiralities found in bulk CNT forests; these material uncertainties would make subsequent cryoEM analysis complicated and less robust. Several authors have also experimented with directly growing CNTs on TEM grids [59], [60] and while interesting, these works produced grid coverings that were less then compelling and at the same time were very difficult to fabricate and without the possibility to select for chirality. Armed with literature of past experiments it was clear that future experimentation should focus specifically on the deposition of purified SWCNT on TEM grids rather than synthesizing them from scratch. Once a repeatable SWCNT deposition protocol for TEM grids was established further studies could be carried out on beam-induced attenuation with biological samples as well as selective particle capture.

The most logical starting point for experimentation was to simply drop-cast metallic SWCNTs solubilized in water with sodium dodecyl sulfate (SDS). The metallic SWCNT conductivities and water solvent make such a system the ideal first deposition candidate. 10 μL of NanoIntegris IsoNanotubes-M SWCNTs were pipetted and allowed to dry on a copper Quanti-Foil® R3/3 TEM grid that was supported by anti-capillary reverse grip tweezers. Images were obtained with 10keV electrons on a Zeiss Supra VP55 SEM.

SEM images revealed that the deposited material was heavily agglomerated. Such behaviour is typical of SWCNTs in general as Van de Waals forces are known to strongly pull tubes together as seen in Figure 3.10. These initial micrographs begged the question whether or not these bundles were indeed true SWCNTs and not random debris from within the suspension. Such chemical questions were addressed through Raman spectroscopy. The Raman spectrum in Figure 3.11 was collected using an excitation wavelength of 514nm. Striking G′ and G peaks at 2700 and 1582 $cm^{-1}$ indicate long range $sp^2$ carbon binding thus indicating the above covering was indeed bundled, but intact SWCNTs. The presence of a 1550 $cm^{-1}$ radial breathing mode (RBM) indicates metallic SWCNTs. Lastly, the considerably small defect peak at 1350 $cm^{-1}$ when compared to the G peak intensity is indicative of

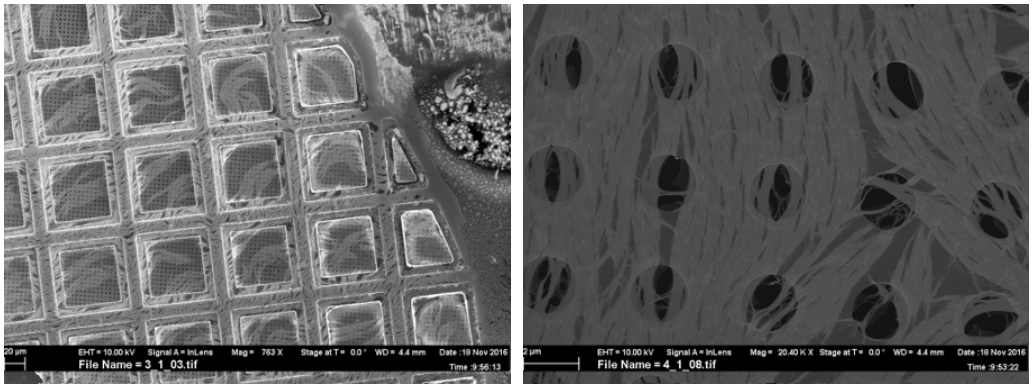


(a) 763x magnification (b) 20kx magnification

Figure 3.10: Initial SWCNT depositions

very few defects within the SWCNT crystal structure [61].

Continued examination with a 100 keV TEM reveals that the SWCNT network was thick with nematically aligned tubes and darker patches on the very top of the network as is seen in Figure 3.12a. Energy-dispersive X-ray spectroscopy (EDX) was performed on these dark patches. The resulting spectrum is depicted in Figure 3.12c and indicates high amounts of elemental iodine. While at first surprising, this was found to be the remains of surfactant used in density gradient ultracentrifugation used for tube purification. Higher magnification (Figure 3.12b) also reveals that individual tubes covered with a surfactant (possibly SDS) were segregating from the main network layer. Overall, initial experimentation demonstrated that the acquired tubes are in fact structurally intact but suffer from agglomeration. The solubilized SWCNTs refracted light blue indicating that while in solution they were in an unbundled state before being applied to the grid. This knowledge along with Raman confirmation of metallic SWCNT structures it was understood that tubes were agglomerating either upon contact with TEM grid or while the solvent was drying.

Throughout the early stages of this project the majority of experimentation focused on obtaining what could be considered a subjectively adequate dispersion state of SWCNTs on a TEM grid, this task was exceedingly difficult. It was initially thought that tube coverage could be controlled through surface functionalization of either the grid itself or the membrane support. Within the transistor development community it is common to adhere SWCNTs to silicon or titanium oxide surfaces through salinization-amine linkers such as (3–aminopropyl)triethoxysilane or APTES. Surface functional groups like APTES will bind to oxidized metal surfaces such as silicon and titanium

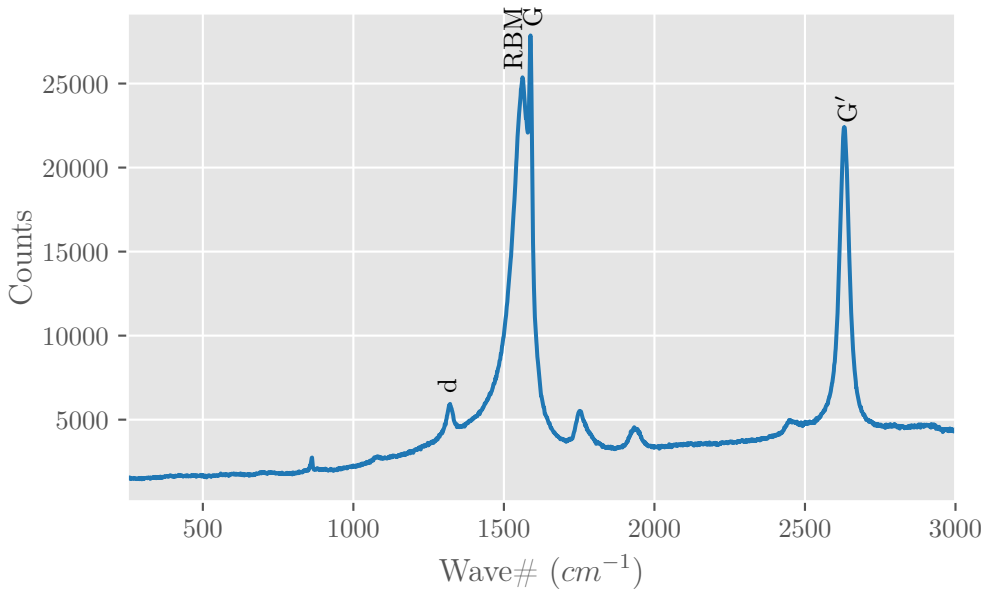


Figure 3.11: Raman spectrum of deposited metallic SWCNTs

with basal silane moieties allowing the highly reactive amine group free to bind with subsequent organic particles. The use of APTES in conjunction with titanium TEM grids was initially used and while not graphically documented, the conjugation of the SWCNTs to the titanium grid was so great that black tube bundles visible to naked eye formed on the grid. Care was taken to quickly dispose of these samples and no photo was taken before cleanup and disposal.

From initial experiments it was readily apparent that lack of tube coverage was not the issue but instead controlling the solvent evaporation was problematic, as the tubes were visibly suspended in solution but would align in a nemetic fashion while the solvent dried. With this information in mind, experiments were carried out that tried to control evaporation by various means. The initial experimentation phase of SWCNT deposition methods was extensive with many different experimental trials were performed using a variety of chemical and physical fixation methods. The most conclusive experiments are reported in the following text.

Inspired by graphene deposition procedures, it was thought perhaps a polymer substrate could act as an anchoring agent for the SWCNTs to initially settle on. After the SWCNT network was formed, the polymer substrate could then be dissolved away thus yielding a SWCNT network mounted on a TEM grid. The above procedure was carried out in several trials using

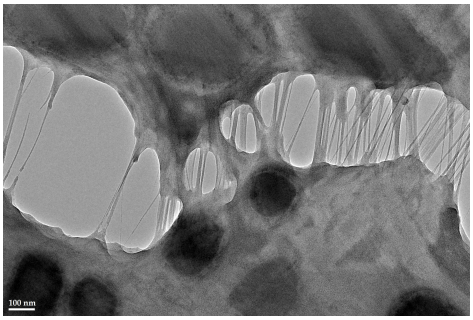

(a) Agglomerated tubes

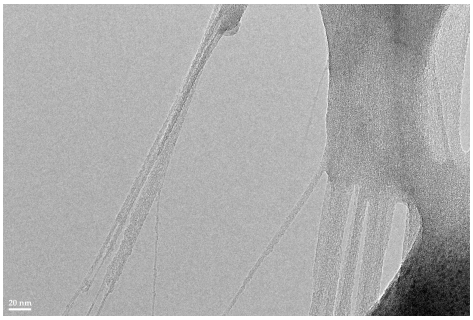

(b) SDS on SWCNTs

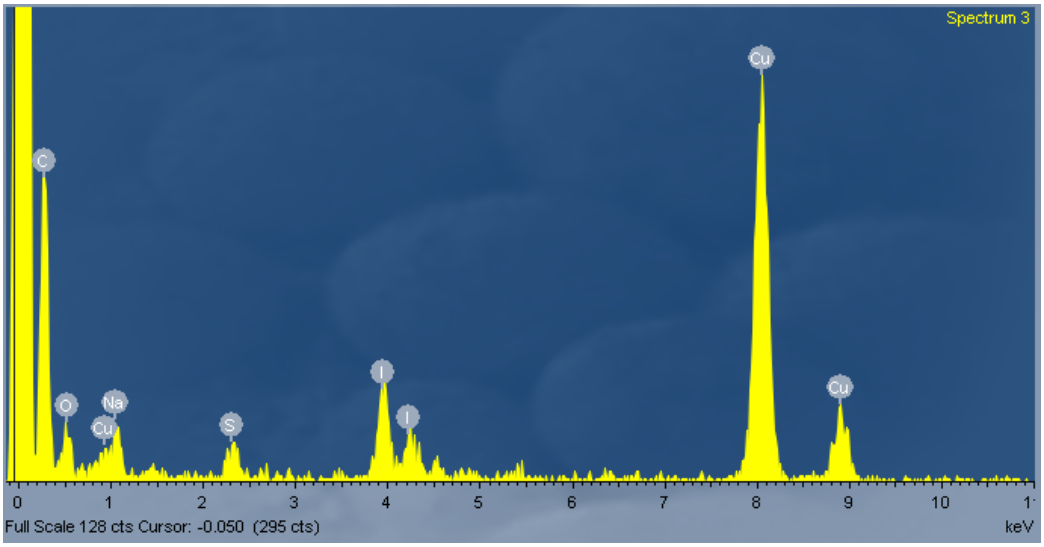


(c) EDX spectrum

Figure 3.12: TEM analysis of initial deposition.

NanoIntegris IsoNanotubes-M and 300 mesh Formvar covered copper grids. 3µL of SWCNTs were pipetted on the lower surface of the Formvar grid such that the tubes were directly touching the grid-bar/Formvar surface. The solvent was allowed to dry in place, once dry the grids were gently dipped in chloroform for 20min and allowed to air dry. This protocol was experimented with multiple times with very low repeatability. Figures 3.13 and 3.14 illustrate a successful deposition imaged with 200keV electrons on a Jeol 2200 TEM.

From 3.14 it can be seen that when successfully forming a SWCNT network, the individual tubes will lay flat without much protrusion from the network plane. While successful, it was exceedingly hard to replicate the results seen in the above tomograms. These difficulties in obtaining reproducible results called for more experimentation.


Figure 3.13: Metallic SWCNTs deposited atop of lacy carbon - Formvar grids followed by chloroform etching.

Under the premise that one could physically restrain the tubes before they agglomerate in the drying solvent it was thought to use SWCNT membrane protocols directly from Nanointegris where aqueous SWCNT suspensions are pumped directly through micro-cellulose filters then abutted against the target substrate and immersed in a refluxed methanol bath that dissolves the micro-cellulose filter. In such a system it was presumed that the physical state of the indivudule nanotube would be fixed in place upon making contact with the cellulose filter thus avoided agglomeration. The results from this experiment can be seen in Figure 3.15, and while it was possible to obtain reproducible SWCNT coverage of the grid, remnant cellulose would remain fixed to the SWCNTs. The success of making a SWCNT network with appreciable area density and overall coverage was overshadowed by the fact that there are large amounts of cellulose covering the grid. This cellulose makes creating a cryoEM dataset difficult if not impossible, thus it was deemed that a fresh approach was necessary.

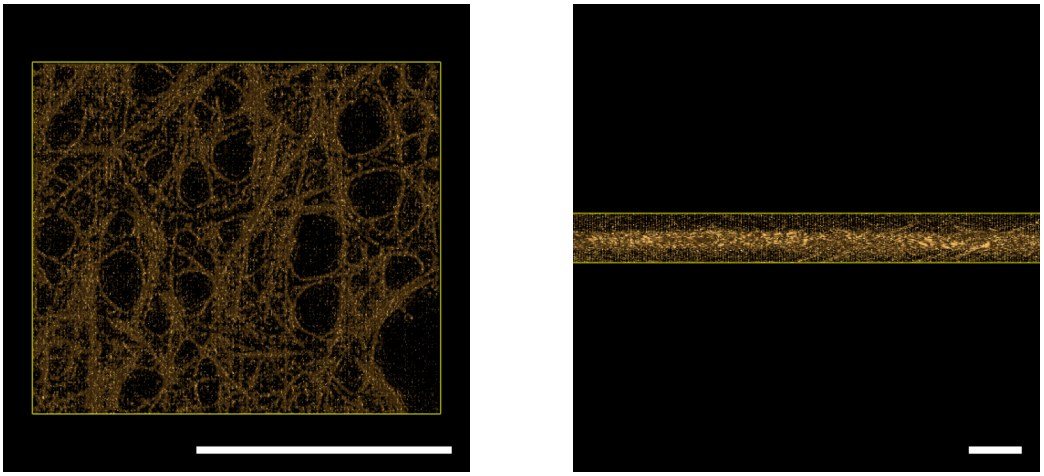

(a) Top-view (scale bar equals 250nm)

(b) Side-view (scale bar equals 25nm)

Figure 3.14: Electron tomogram of Formvar SWCNT deposition.

Rather than physically capturing SWCNT in place either with a micro-cellulose filter or polymer support, it was thought that using a highly volatile organic solvent would produce the desired effect by quickly evaporating before agglomeration of the tubes could take place. Final deposition experiments utilized metallic SWCNTs solubilized in DMF and also semiconducting SWCNTs in a proprietary steric polymer wrapping. 3μL of metallic NanoIntegris IsoNanotubes in DMF were pipetted and allowed to dry on lacy carbon grid with the results displayed in Figure 3.16. 3μL of semiconducting NanoIntegris IsoSol-S100® Polymer-Wrapped Nanotubes in toluene were allowed to dry on lacy carbon grids. The polymer wrapping was then removed by a sequentially washing in tetrahydrofuran, toluene, and isopropanol for two minutes each, the results of these experiments can be seen in Figure 3.17. Comparing Figures 3.16 and 3.17 it can be seen that the agglomeration state of SWCNTs in DMF was far greater than that of the toluene solution. This can be attributed to two different factors, the first of which being that the DMF is far less volatile a solvent than toluene. In the extended amount of time that it takes for the DMF to evaporate the tubes inside the solution have will be more likely to agglomerate. Toluene on the other hand is among one of the most volatile organic solvents which provides less time for the SWCNTs to agglomerate before the solvent evaporates. Secondly, the polymer wrapping of the tubes will naturally provide a steric barrier which hinders inter-tube interactions.

Overall, the use of polymer wrapped SWCNTs in toluene was seen to

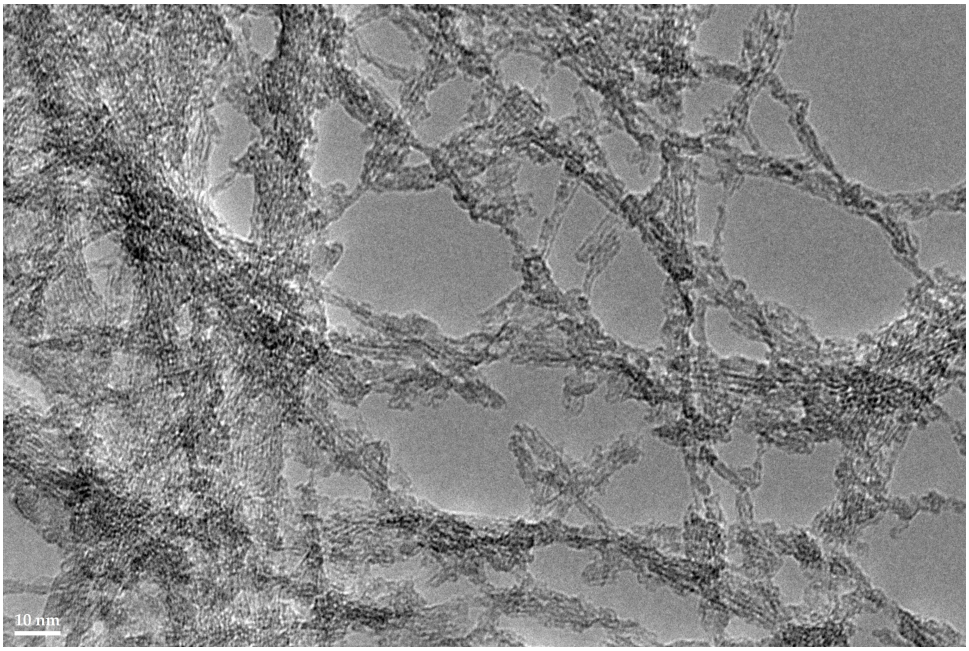


Figure 3.15: SWCNT and remnant cellulose residue

be the most stable system that could reproducibly create large area, non-agglomerated SWCNT networks. This platform was used to pursue further cryoEM and selective capture experimentation.

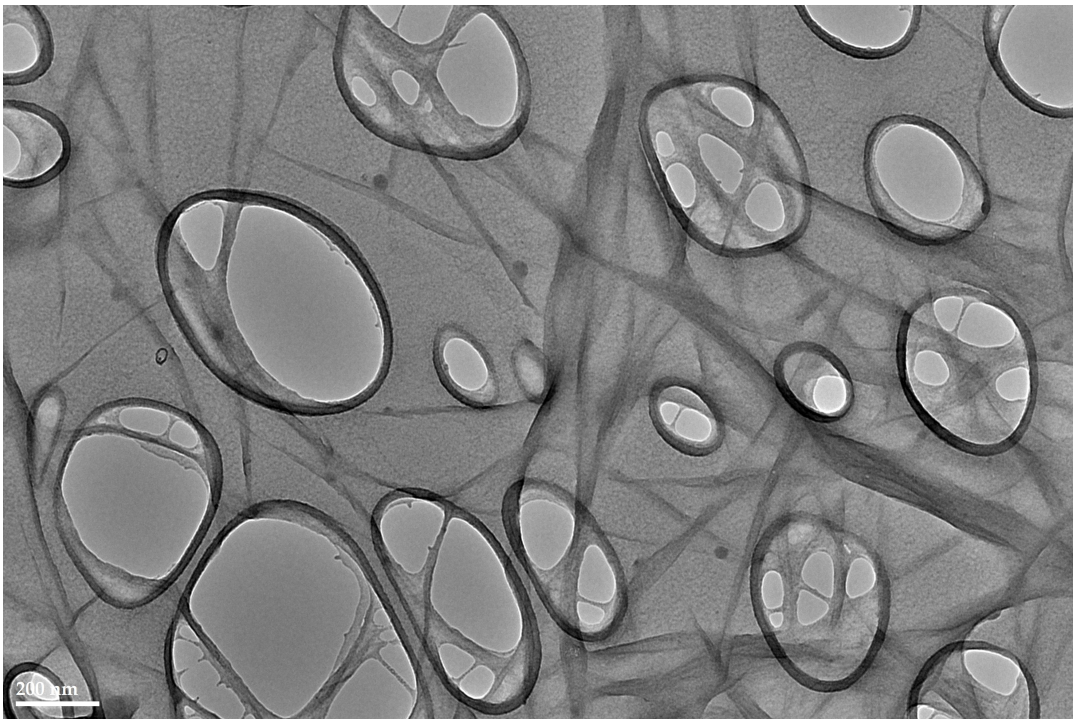


Figure 3.16: Metallic SWCNT network drop cast from DMF solution.

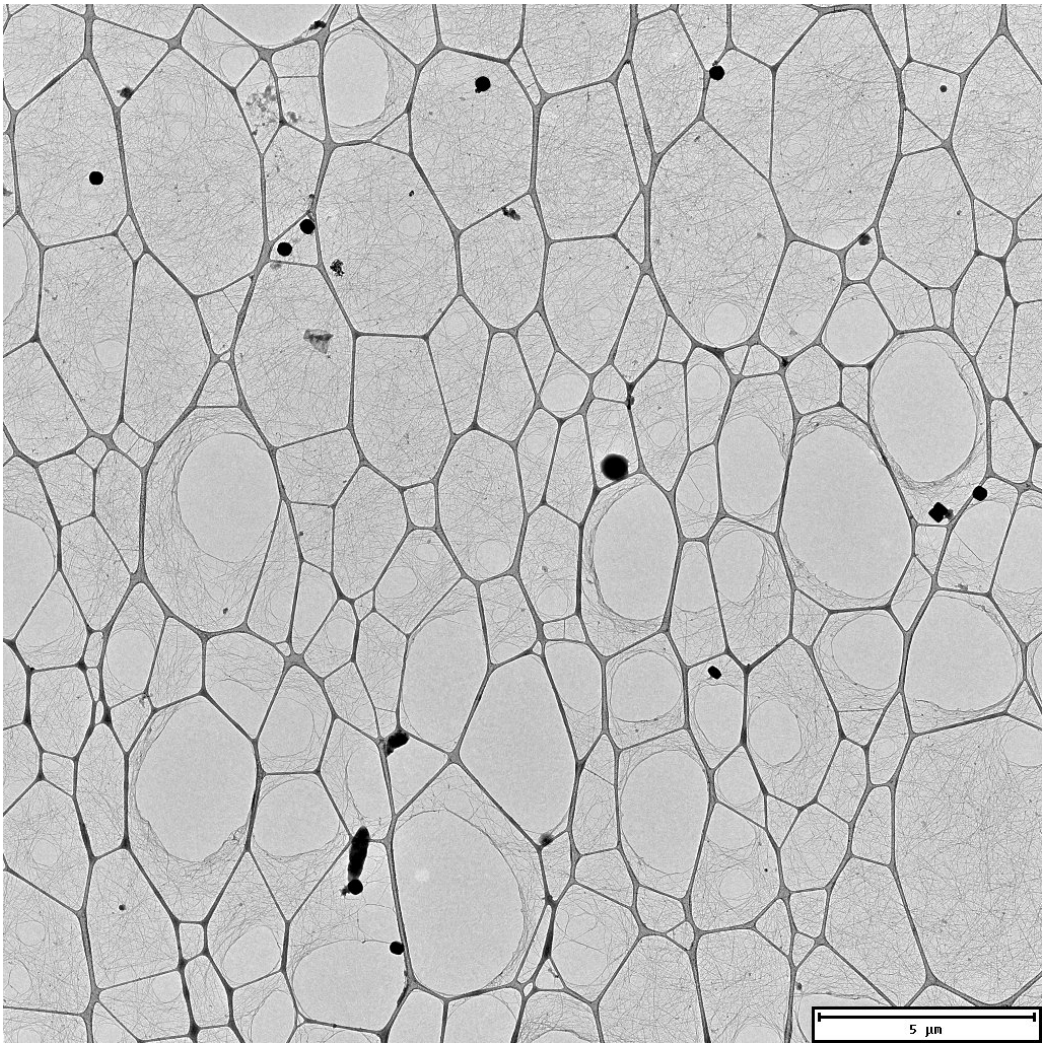


Figure 3.17: Semiconducting SWCNT network from drop casting NanoIntegris IsoSol-S100® Polymer-Wrapped Nanotubes. Faceted/round Zeolite crystals can be also seen on the grid and were deposited after SWCNT deposition.

# Chapter 4

# CryoEM with SWCNT grids

To validate the ability of SWCNT networks to attenuate beam-induced motion, proof of principle experiments were carried out utilizing gold nanoparticles which are nominally used as fiducial markers in cryotomography. Using a non-biological target simplifies both sample preparation and processing as gold fiducial markers come already solubilized in aqueous solution and more importantly exhibit high contrast against the background of ice and SWCNTs allowing for easier particle picking and subsequent processing. The principal disadvantage of using fiducials come by virtue of the fact that nanoparticles are only roughly spherical with large heterogenicity. This makes it impossible to assign Euler angles and determine if the SWCNT network influences particle orientation and also doesn't allow for the calculation of the ice surface's drumming motion of the via changes particle tilt throughout each movie frame.

## 4.1 Fiducial Experiment

The experimental preparation of SWCNT EM grids can be carried out in any structural biology laboratory and starts with SWCNT deposition. 3 μL of 0.01 mg/mL toluene suspended NanoIntegris IsoSol-S100® Polymer-Wrapped Nanotubes were pipetted onto a copper Quanti-Foil® R3/3 TEM grid that was supported by anti-capillary reverse grip tweezers. Similar to a negative stain preparation, the solvent was allowed to dry from the grid whilst being held in place with tweezers. Once dry, the polymer wrapping which prevented the SWCNT suspension from agglomerating was dissolved by sequentially washing the grid in tetrahydrofuran, toluene, and isopropanol for two minutes each. The SWCNT network that formed on the grid was qualitatively seen to be extremely stable as repeated imaging of the same area over several weeks yielded no changes in the network. As such, grids containing SWCNT networks could be nominally handled and stored.

Application of the gold fiducial markers was carried out in the same manner as that of a typical cryoEM grid plunging. The grid containing the SWCNT network was glow discharged in 100W air plasma at 0.4 millibars for 20 seconds. 3μL of 10nm gold fiducials stabilized in a citrate buffer from Sigma Aldrich were pipetted on the grid then plunged into liquid ethane with an FEI Vitrobot at 22°C and 100% humidity using blot force #1 with a 3 second blot time. The above protocols provide adequate SWCNT coverage and fiducial densities that are both highly reproducible and readily available for most structural biology laboratories, as seen in Figure 4.1. As to control for the presence of the SWCNT network, identical Quanti-Foil® grids were plunged with fiducials using the same procedures as above but without SWCNTs. Imaging of the grids was carried out on an FEI Polara TEM at 300keV using a Gatan K2 direct electron camera operated in super-resolution mode with a raw pixel size of 0.51 Å/pixel. A total radiation dose of 81.5 $e^{-}/\text{Å}^{2}$ over 70 frames were used to acquire each image stack. In order to observe sample behaviour typically seen in cryotomography, image stacks with tilt angles of 0° and 60° were each taken on separate grids thus yielding a total of 4 experimental trials.

Data processing was carried out using cryoSPARC v2; this was chiefly since no protein structures were to be ascertained, only the particle trajectories. CyroSPARC conveniently calculates local particle trajectories before the cross-correlation of 2D averages. In contrast, RELION will correct both local motions and CTFs as the penultimate processing step and require that initial 3D structures are calculated. The large heterogenicity Au of nanoparticles do not facilitate structural determination; thus, using cryoSPARC was

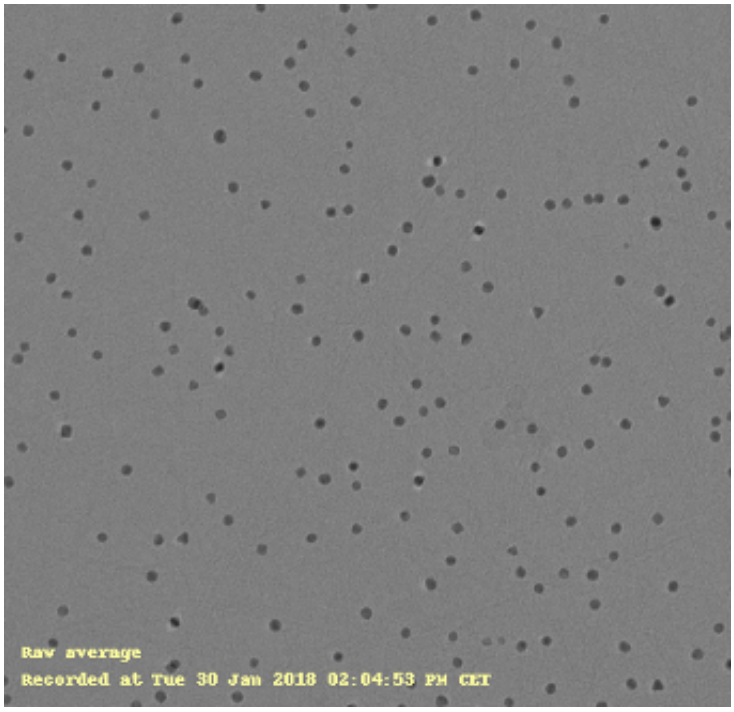


Figure 4.1: 10nm Au fiducial markers on a SWCNT network imaged with 300keV electrons.

deemed most appropriate.

All raw movie stacks and gain references were imported into cryoSPARC v2 with all aforementioned micrograph parameters. Full frame motion correction was carried out through the MotionCor2 wrapper within cryoSPARC using only one patch. While better drift correction can be achieved with MotionCor2 using smaller patches, it is desirable in this case to maintain the original spacing between the fiducials and correct the global drift with one trajectory as to not skew the local particle trajectories. CTF correction was then carried out using CTFFIND4 within cryoSPARC for ease of processing but is not explicitly required for this experiment as trajectories are to be calculated through frame by frame cross-correlation using very low spatial frequencies of provided by the fiducials. Particles were then picked using Gaussian blob templates followed by a brief 2D classification to remove fiducials that are directly touching one another. Local motion correction was then carried out on particles from selected 2D classes.

CryoSPARC v2 doesn't allow direct data manipulation within its graphical interface; however, global frame motion and particle tracks throughout each movie frame are conveniently provided in NumPy arrays for each movie.

Utilizing Python scripts seen in Appendix A, both global and local motion trajectories were harvested from their respective directories. Each local particle trajectory was corrected for its respective global motion and then amalgamated into one single NumPy array such that multiple datasets can be subsequently manipulated and compared.

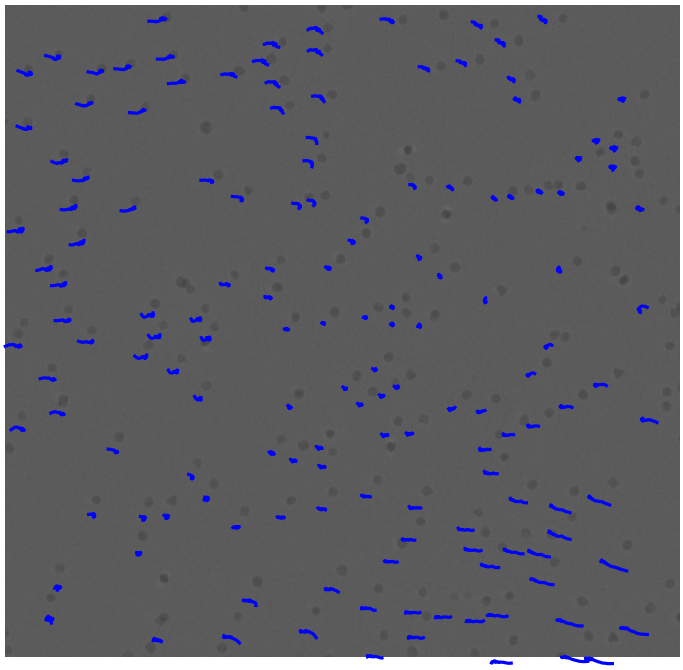

Figure 4.2: 10nm Au fiducial markers on a SWCNT network with particle movement tracks. Movement tracks are scaled by 30 times for viewing clarity. This micrograph was taken with 0° tilt.

Figure 4.2 shows fiducial marker motion tracks on a grid that was imaged at 0° tilt and contains SWCNTs. The motion tracks in blue are scaled up by 30 times for enhanced viewability and then superimposed onto the micrograph from which they were calculated. It should be noticed that the absolute track lengths in the middle of the field of view are relatively smaller than those seen at the periphery of the frame. Such behaviour is indicative of the circular bulging or drumming effect that has been described by both Brilot and Glaeser [10], [62]. Coordinates from the particle trajectories seen in Figure 4.2 were amalgamated for every micrograph in each respective dataset. The in-plane motions were then described by separately calculating every particle's absolute distance from its initial position, the per-frame speed and path length throughout each individual particle movie stack.

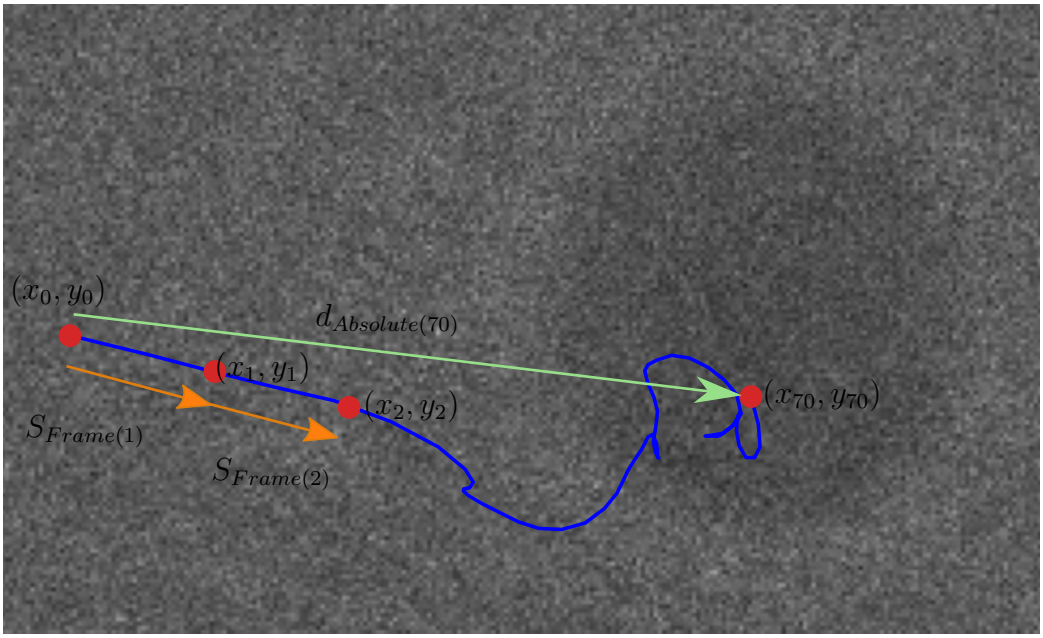


Figure 4.3: Individual particle movement track taken from data collected on SWCNT grids with 0° tilt.

$$d_{Absolute}(i) = \sqrt{(x_i - x_0)^2 + (y_i - y_0)^2} \tag{4.1}$$

$$d_{Path}(i) = \sqrt{(x_i - x_{i-1})^2 + (y_i - y_{i-1})^2} + d_{Path}(i-1) \tag{4.2}$$

$$s_{Frame}(i) = \sqrt{(x_i - x_{i-1})^2 + (y_i - y_{i-1})^2} \tag{4.3}$$

Each of the three descriptive metrics in Equations 4.1–4.3 were calculated for all particles in every frame. Average values for each respective frame were then plotted against the electron fluence. The standard error mean for all particle movement in each frame was calculated via the SciPy statistics toolbox in Python.

Upon visual inspection of both raw particle tracks and their associated plots, it is readily apparent that the majority of the motion exists in within the first quarter of the movie, this behaviour is in line with current literature. Absolute motion plots are also readily comparable to similar plots provided by Russo and Passmore [13]. Data collected at 60° exhibited a marked increase in both speed and displacement compared to those collected at 0°, this is a consequence of out of plane motion. The particle tracks seen in Figure 4.2 are strictly in-plane motions, the out of plane motion exists perpendicular to the viewing angle and as such is not visible. At high tilt angles, the out of

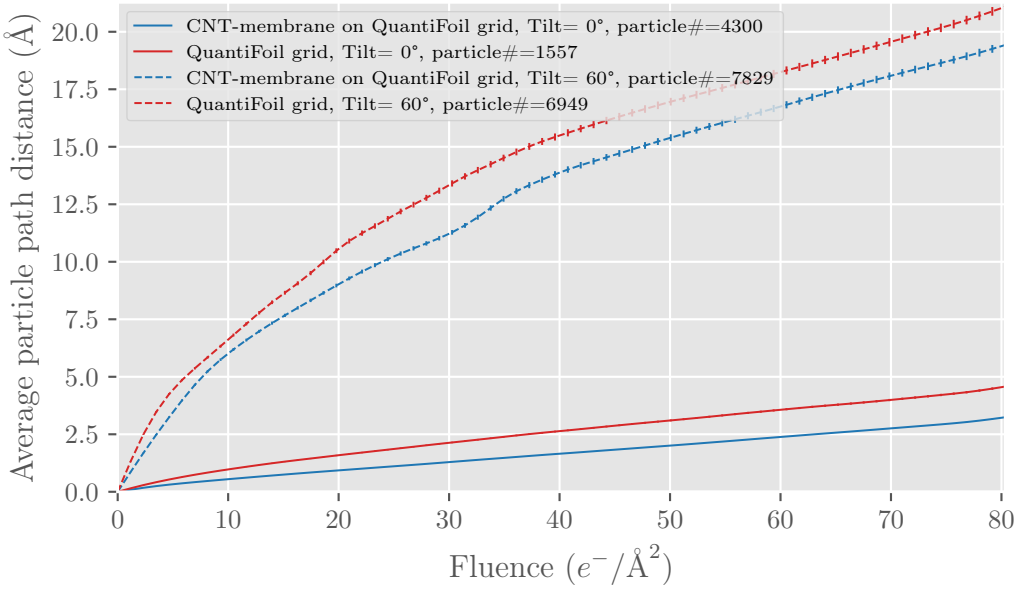


Figure 4.4: Average fiducial path distance. Error bars show standard error mean.

plane motions will become apparent, and thus the particle tracks will start to represent both in-plane and out-of-plane motions. Additionally, the specific dose per cross-section of specimen will be higher for tilted samples, thus resulting in additional in-plane and out-of-plane motions. Strictly speaking, the 60° data can't be directly compared against the 0° data as it contains additional motion vectors not seen in the 0° data. However, these results are all explainable and do fall within general expectations. An interesting phenomenon can be seen in the 60° data at fluences of approximately 20 $e^-/Å^2$ and 35 $e^-/Å^2$, where there appears to be an increase in displacement followed by relaxation. While it is difficult to say with certainty the cause of these peaks, one could guess that they are related to an unforeseen discharging of the sample through preferential electrically conductive pathways built up in the vitreous ice, or perhaps the expulsion and degassing of radiolysis products from the sample. In general, it can be seen that using the SWCNT networks did reduce the in-plane motions at both tilt angles. Such movement and displacement decreases can be attributed to both to increased thermal conductivity and structural rigidity in the vitreous ice sheet granted by the SWCNT network.

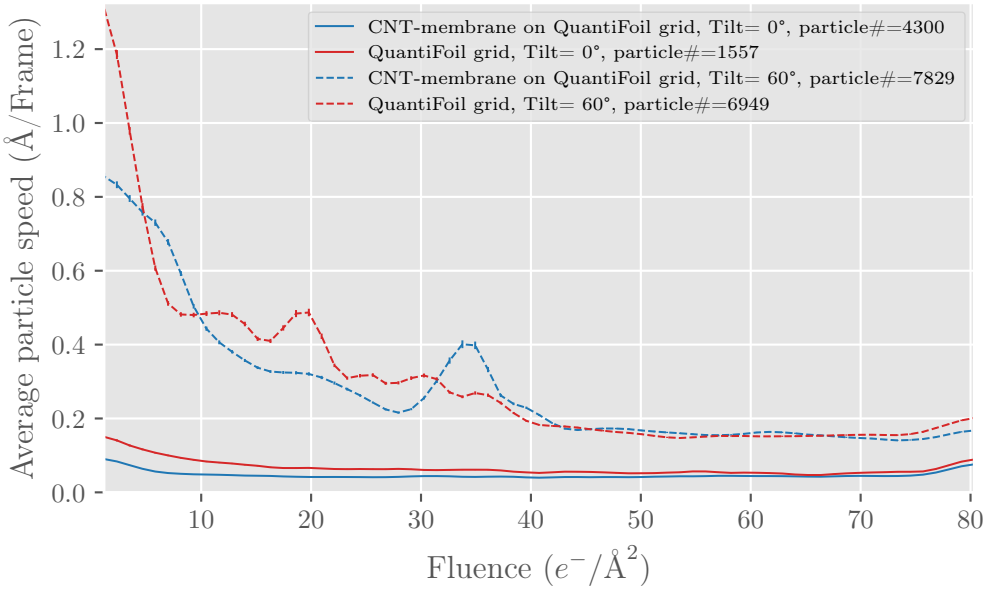


Figure 4.5: Average per-frame fiducial speed. Error bars show standard error mean.

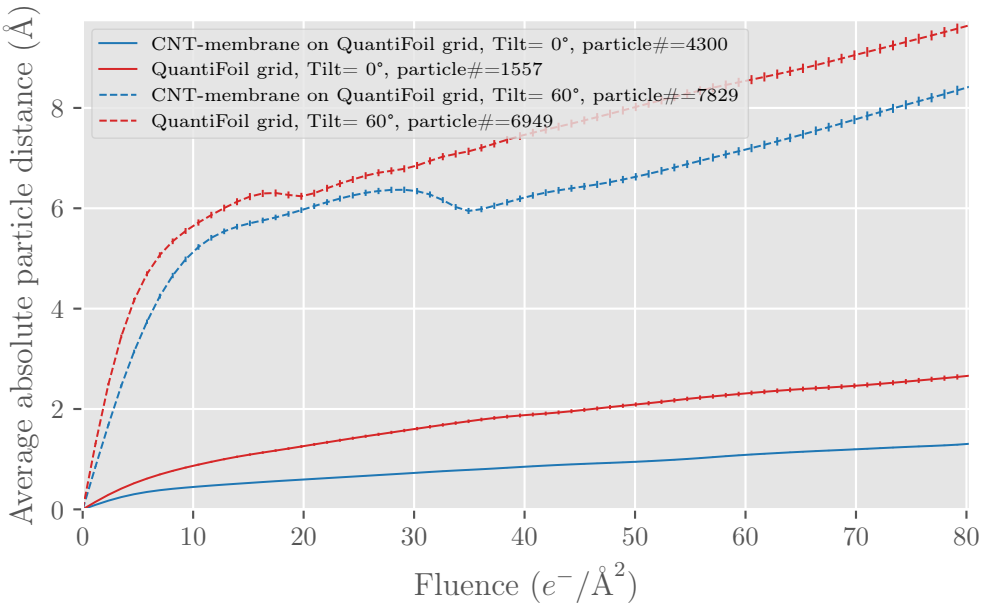


Figure 4.6: Absolute fiducial displacements for each frame. Error bars show standard error mean.

## 4.2 β-galactosidase Experiment

With the proof of concept experiments with fiducials validating the efficacy of SWCNTs in attenuating beam-induced motion, go-head experiments with proper biological targets were carried out utilizing the de facto standard test protein for cryoEM; β-galactosidase. β-galactosidase is a widely studied enzyme responsible for the hydrolysis of glycosidic bonds allowing for the breakdown of lactose to galactose and glucose. β-galactosidase forms a 426 kDa diamond-shaped tetramer as seen in Figure 4.7 and is widely available as a lyophilized powder from several commercial sources. As a modestly sized protein that is tightly packed without many externally flexible domains, β-galactosidase is very stable, easy to purify and has served as a benchmark protein in which many state of the art cryoEM techniques have been demonstrated [63]–[66].

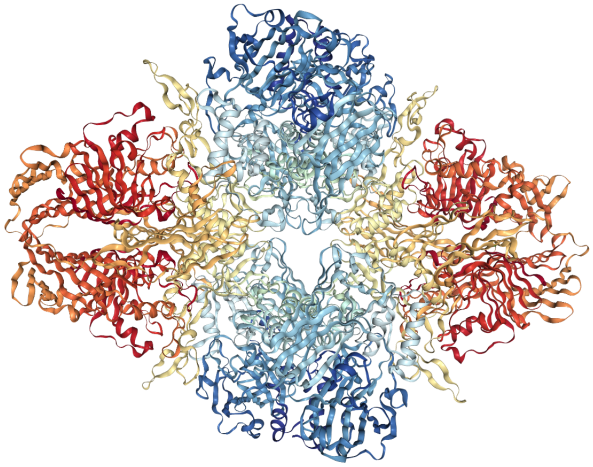

Figure 4.7: β-galactosidase tetramer model derived from a from 2.2Å cryoEM density map [67].

Protein preparation begins by dissolving lyophilised β-galactosidase protein purchased from Sigma Aldrich (G3153-5M) overnight at 4°C in a buffer consisting of pH 7.5 25mM Tris, 10mM $MgCl_2$, 100mM NaCl, 1mM TCEP. The protein solution was then concentrated and injected into a Superdex 200 size exclusion column for purification. The resulting chromatograph is shown in Figure 4.8 (left) and has a clean first peak for which fractions A7, A8 and A9 where collected. An SDS-PAGE of the collected fractions was performed with Nu-Page Tris running buffer and PageRuler Plus pre-stained protein ladder Figure 4.8 (right). It can be seen that all three fractions in the

PAGE are all approximately the same size and smaller than 130 kDa without any further smaller impurities in the sample. This indicates that SEC purification was successful and that only denatured 126 kDa β-galactosidase proteins were in the PAGE. The entire sample was then concentrated with an Amicon cut-off filter to 3 mg/mL and portioned in 150µL aliquots, and flash-frozen in liquid nitrogen for later use.

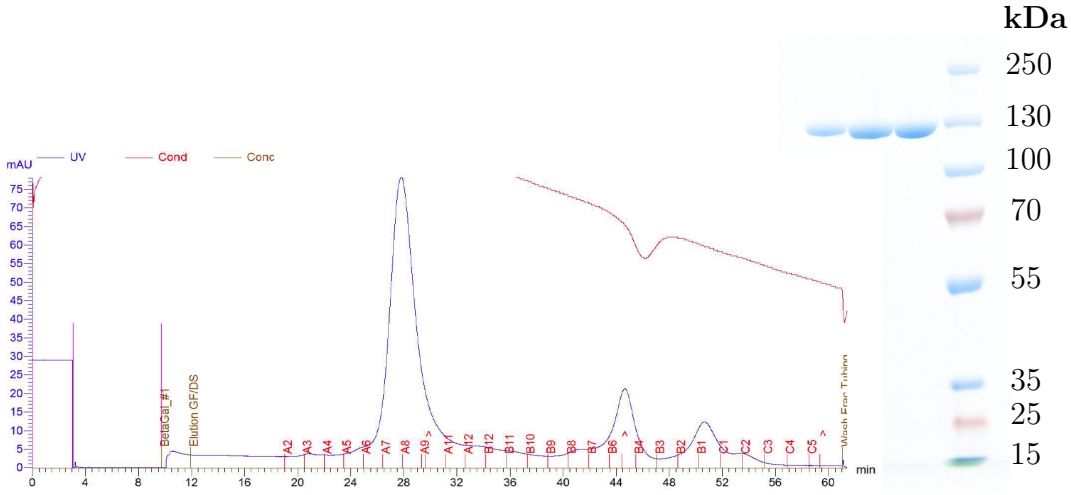


Figure 4.8: Chromatagraph from Superdex 200 size exclusion purification (left). SDS-PAGE of fractions A7, A8, A9 (right).

Preparation for plunging began with the drop-casting of 3µL of NanoIntegris IsoSol-S100® Polymer-Wrapped Nanotubes onto R1/3 UltrAuFoil® gold EM grids. The polymer jackets surrounding the SWCNTs were then dissolved by sequentially rinsing the grid in tetrahydrofuran, toluene, and isopropanol for two minutes each and allowed to air dry. Prior to plunging the grid was glow discharged in 100W air plasma at 0.4 millibars for 20 seconds, 3µL of β-galactosidase protein was then pipetted on the grid and plunged into liquid ethane with an FEI Vitrobot at 22°C and 100% humidity using blot force #1 with a 3 second blot time. An R1/3 UltrAuFoil® without SWCNTs was also plunged with the same protein sample to serve as a control. Both grids were imaged with FEI Krios Titan using a K2 camera operating in 4k counting mode. The two grids were imaged during different sessions; the experimental grid with SWCNTs was imaged with a pixel size of 0.51Å for 20 frames with a dose of 3.1125 $e^-/Å^2$. The control grid was imaged with a pixel size of 0.64Å for 80 frames with a per-frame dose of 1.0375 $e^-/Å^2$. All control micrographs were subsequently re-averaged to a per-frame dose of 3.1125 $e^-/Å^2$ then truncated to 20 frames in total such that dose-dependant movement and B-factors can be compared against the

other dataset.

All datasets were processed entirely in RELION 3.0-beta within nominal processing pipelines. Global motion correction was carried out with RELION's version of MotionCor2. Specifically using RELION's motion correction was necessary for carrying local motion correction or Particle Polishing in subsequent processing steps. Both datasets were left un-binned, dose-weighted and corrected by a single patch as to obtain accurate local motion tracks in later processing. CTF correction for both datasets was performed with CTFFIND4.1 after which, processing pipelines for both datasets were handled separately.

Control data not containing the SWCNT network were picked using RELION's Laplacian-of-Gaussian blob detection with a minimum radius of 180Å and a maximum radius of 250Å. These particles were then extracted with a 448 box size and binned four times. 2D classification was performed with 50 classes, of which the best 26 were selected, re-centred and re-extracted at full resolution. Nominal 2D classes can be seen in Figure 4.9.

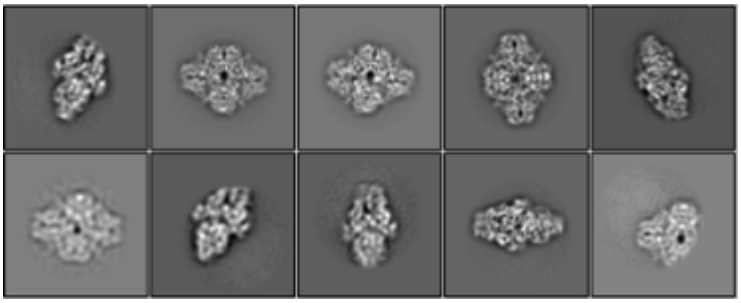

Figure 4.9: Selected 2D classes following Laplacian-of-Gaussian particle picking.

The abundance of good classes from a single round of 2D classification and picking gives further credibility the positive SDS-PAGE results. 3D classification using six classes was performed using the previously extracted full resolution images along with a standard reference map from the protein data bank [67]. For consistency of results, the same reference was utilized for all 3D classifications and refinement jobs in both experimental and control data with only the pixel size being altered to match the respective data.

From the 3D classes that were selected and shown in Figure 4.10, there existed 45821 particles. While this would only be considered a very modest particle population in a nominal cryoEM pipeline, however, issues with the SWCNT data forced the random de-selection within RELION to obtain a particle population of 5209 as to accurately compare resolutions and B-factors without skewed results due to increased particle counts. After initial

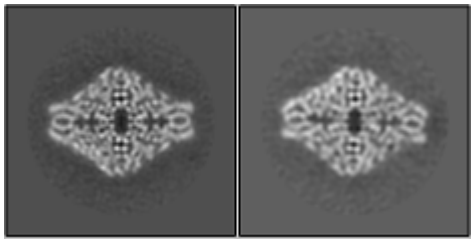

Figure 4.10: Selected 3D classes following 2D classification.

3D refinement utilizing the same reference density used for classification, CtfRefine and Bayesian polishing was carried out. Postprocessing utilizing the solvent mask created from the initial 3D refinement yielded a resolution of 3.18Å as seen in Figure 4.11.

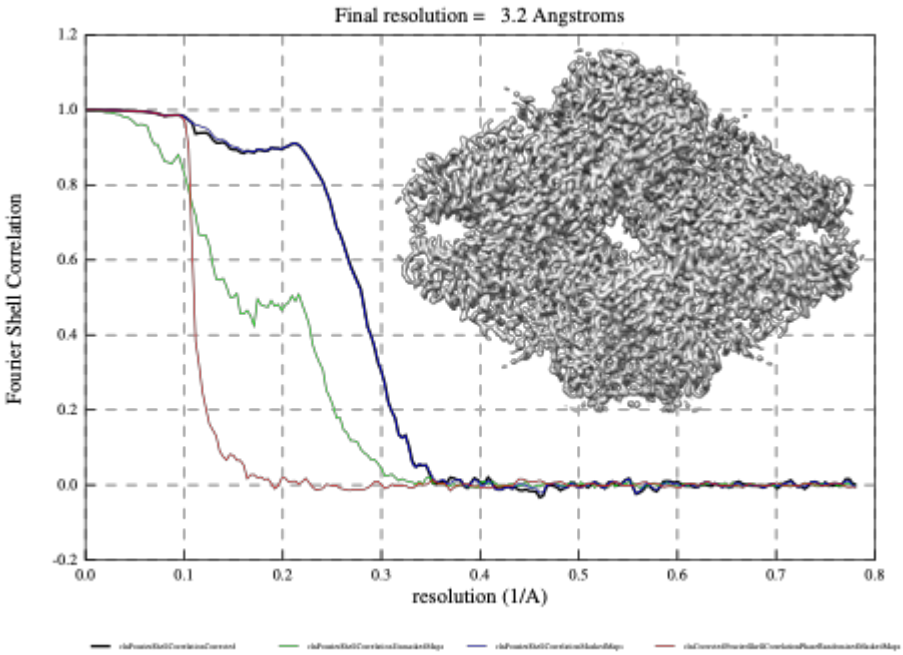


Figure 4.11: Fourier shell correlation and gold standard cut-off resolution β-galactosidase control sample. Inset: β-galactosidase structure.

Processing of the control data, especially that of a known entity like β-galactosidase was very standard; however, the processing of the experimental SWCNT dataset did present several challenges. Automated particle picking of the experimental data was carried out with GAUTOMATCH and utilized the standard reference density map used prior were made in cryoSPARC as a template. A small population of 40720 particles were picked and extracted

for 2D classification within RELION. 2D classification was carried out with particles binned by a factor of four and 50 classes. As can be seen in Figure 4.12, there exist both isolate particles and particles that are conjugated to the surface of the SWCNTs. With a nominal 1.3nm diameter and high aspect ratio, SWCNT will often be the driving factor in initial 2D averaging. Figure 4.12 illustrates how averages will contain a high degree of alignment along the edges of the SWCNTs with blurred central intensity pixels in the middle of the average that are presumable randomly oriented β-galactosidase particles. Several different strategies were employed in an attempt to clean up the below averages; these include the use of large class numbers and small angular searches for both 2D and 3D classes. These attempts were largely unsuccessful in separating the conjugated β-galactosidase from the SWCNTs to which they were attached, at present, there are several theories to explain this behaviour. The outer edges of the SWCNTs may exhibit such a high contrasting signal as to always drive alignment regardless of the orientation of the protein touching it. Confounding the point as well, the sigma bonds making up the SWCNT are less prone to radiation damage than the peptide bonds comprising the protein and as such will have a more prominent signal throughout the entire movie whereas the target protein will exhibit a degrading signal. It also may be the case that the central densities in the conjugated averages are dust or possibly the remnants of stubborn polymer that couldn't be completely removed from the SWCNTs through solvent washing.

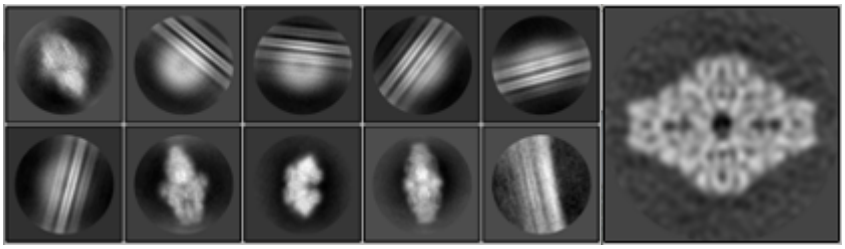

Figure 4.12: 2D classes from experimental SWCNT data. Both isolated and conjugated particles were classified (left). 2D projection of the lone 3D average obtained from non-conjugated proteins found within SWCNT networks (right).

With attempts to properly align the conjugated particles having failed, only the clean untethered proteins were considered for further processing. The particles from the non-conjugated 2D class averages were selected for further 3D classification against a common reference that was utilized in the previous dataset. Unfortunately, only a single class was obtained from 3D

classification can be seen on the right in Figure 4.12. With just a single class in an already limited particle population, only 5209 particles were ultimately selected for further processing. To fairly compare these experimental data against that of the control, particle populations of both data sets were both set to 5209. Following final classification, the selected particles were then subjected to local motion correction via RELION 3.0's Bayesian polishing routine followed per-particle CTF refinement using CTFrefine. Unlike cryoSPARC, local movement data obtained from RELION's Bayesian particle polishing are stored in STAR files within each respective polishing job. Movement data from this experiment were analysed in the same manner as done before with fiducial data with the exception that the raw data was taken from STAR files. Parsing of STAR files was carried out in Python by the cif.read() method of the GEneral MacroMolecular I/O (GEMMI) library. Data blocks coming from the cif.read() were passed as JSON files into Python dictionaries and finally saved as panadas dataframes which were then manipulated and plotted as necessary. Code for these processes is further described in Appendix A.2.

From Figures 4.13, 4.14, and 4.15 it can be seen that proteins within the SWCNT networks exhibited considerably less in-plane lateral motion than proteins in the control population. These results are comparable to those seen with the fiducial data indicating that reductions in lateral drift can be alone attributed to the SWCNTs and are independent of the sample, whether it be a nanoparticle or a protein. Fascinating phenomena can be seen in Figure 4.15, where a spike in per-frame speed can be seen at a fluence of 31 $e^-/\text{Å}^2$ which approximately corresponds to similar spikes in speed with the previous data presented in Figure 4.5. As these events are witnessed roughly at similar electron fluences within their respective movies, it would be astute to consider that said phenomenon is related to the total dose deposited on the grid regardless if caused by electrical discharging or release of radiolysis products.

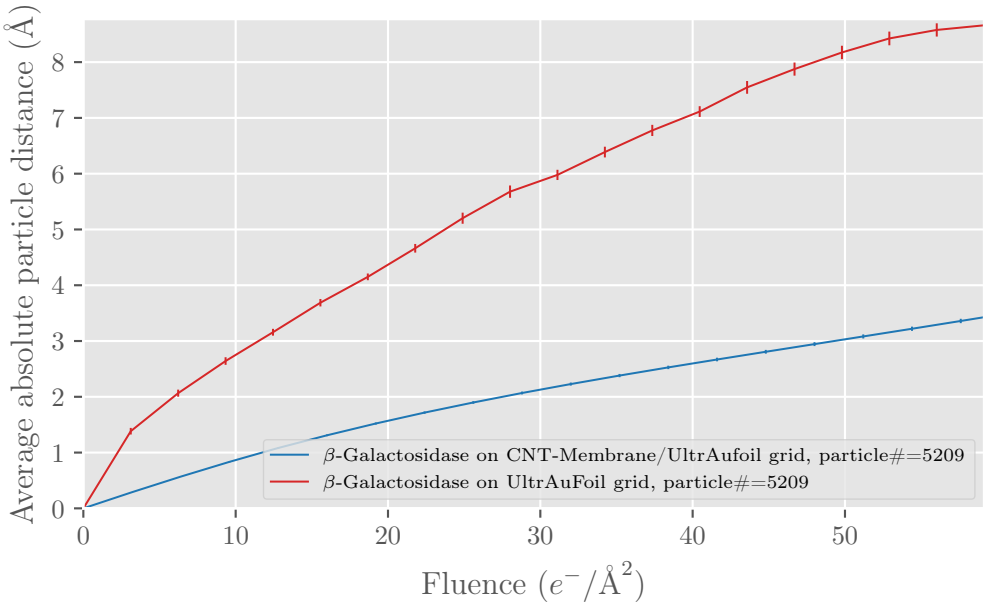


Figure 4.13: Absolute β-galactosidase displacements for each frame. Error bars show standard error mean.

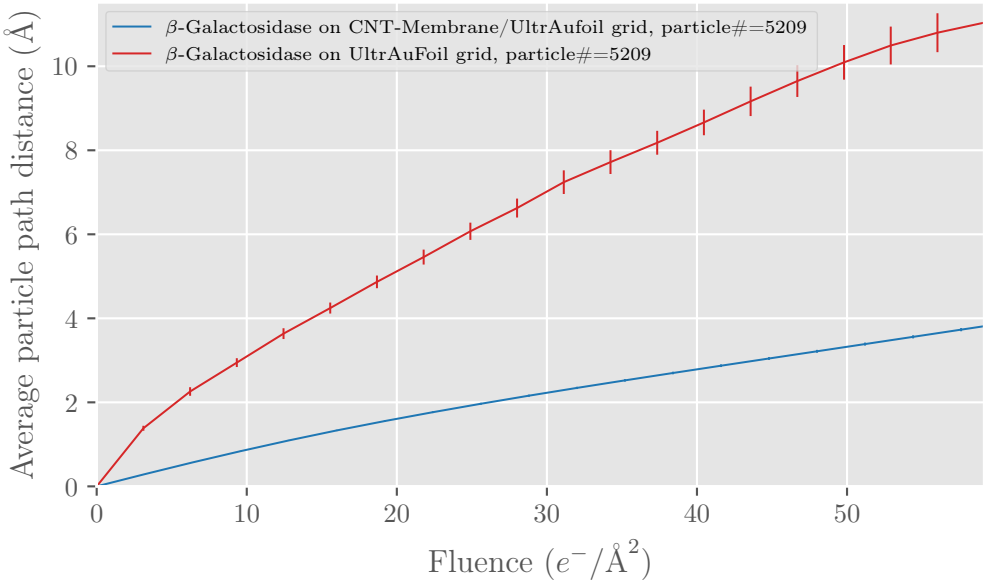


Figure 4.14: Average β-galactosidase path distance. Error bars show standard error mean.

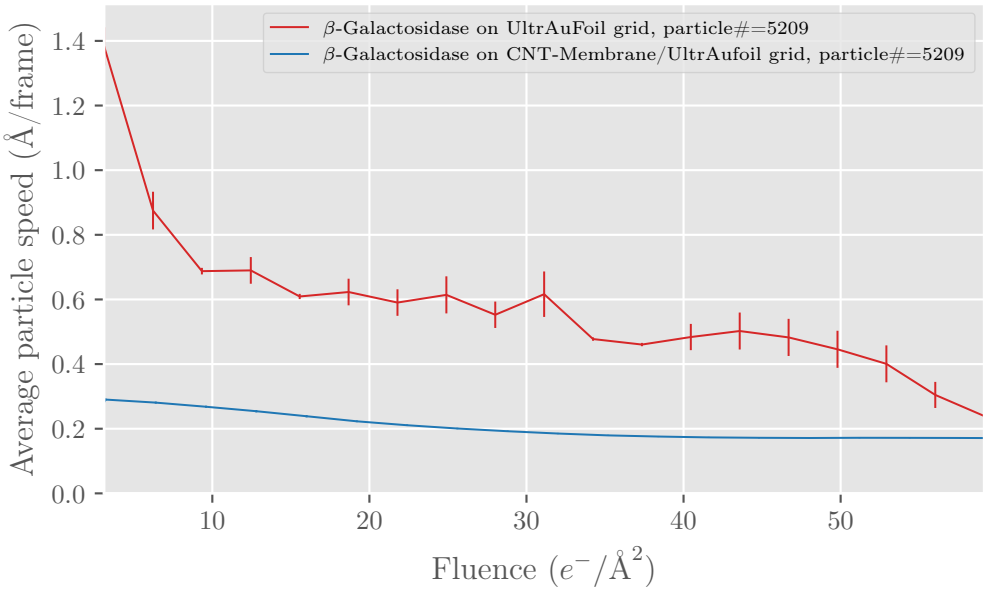


Figure 4.15: Average per-frame β-galactosidase speed. Error bars show standard error mean.

## 4.3 B-Factor Analysis

In order to obtain high-resolution maps, it is necessary to correct for the loss of contrast caused by radiation damage, imperfect images and errors in particle alignment during processing. While it has been shown that beam-induced motion is indeed hindered by the use of SWCNTs, how the motion reduction translates into higher quality images is best described with the use of B-factors, specifically frame weighted B-factors that describe how much data is being obtained from each movie frame within a specific movie. B-factor weighting is often mentioned in the common literature, but only in passing. The following section briefly describes cryoEM B-factor theory and how it is used to evaluate contrast image improvements seen from reducing beam-induced motion.

The theory which addresses contrast loss in cryoEM was developed by Rosenthal and Henderson [68] and utilizes concepts from X-ray crystallography, mainly the exponential loss in structure factor intensity from temperature which is modelled with an exponential component known as a B-factor. Within this framework, both the terms structure factor and B-factor are used analogously to the crystallographic origins from which they were derived, however, in reality, these terms have an explicitly different meaning within cryoEM analysis. Crystallographic structure factor refers to the diffracted beam intensity which is the result of the $\Delta$k = G criterion being satisfied where $\Delta$k is the difference between the incoming and outgoing scattering vectors and G is the reciprocal lattice vector of a specific crystal basis. This beam intensity is proportional to the atomic scattering potential or atomic form factor of the atom responsible for diffraction at the given crystallographic plane. Within a cryoEM context, structure factor describes the contrast or intensity difference between the protein and solvent it surrounds a defined in Equation 4.4 where $(\rho - \rho_0)$ is the difference in scattering between the protein and the crystal and surrounding solvent, $R_g$ the radius of gyration and $d$ the resolution.

$$F = (\rho - \rho_0) V_{protein} e^{-(2\pi^2 R_g^2/3d^2)} \tag{4.4}$$

$$F = ((\rho - \rho_0)/\rho)(\sum_i n_i f_i) e^{-(2\pi^2 R_g^2/3d^2)} \tag{4.5}$$

The solvent contrast term is nominally approximated by 0.28, assuming typical a protein buffer and ice densities. At zero angle or backscattering condition where the resolution is very large, all the atoms within the protein volume will scatter in phase equal to the solvent contrast term $(\rho - \rho_0)/\rho$ as described in Equation 4.5 and seen in Figure 4.16 where the mean structure

factor will become asymptotic in the y-axis. As seen in Figure 4.16, much of the larger dimension structure factor signal is due to the bulk protein shape within the solvent. At 10 Å and below, individual alpha-helices will become responsible for the mean structure factor signal with low dimension structure factors decaying exponentially according to Wilson scattering statistics. Note that the average image noise signal is plotted on the right y-axis and how this noise signal compares to the structure factor on the left y-axis; this cuts to the very heart of cryoEM methodology. Keeping in mind the structure signal (denoted in red) is essentially competing against the average image noise (denoted with vertical dotted lines) and that the structure factor signal must be boosted by averaging many images in order to overcome the structure factor losses due to both scattering and noise. Assuming perfectly contrasted images, one image can hypothetically produce a 20 Å map. Likewise, with approximately 5000 perfectly contrasting images, an atomically resolved map could be produced according to theoretical structure factor decay predicted by Wilson statistics. Within the X-ray crystallography community deviations from the structure factor predicted from Wilson statistics are primarily caused by temperature-induced vibration within the crystal lattice. These temperature-induced fluctuations are taken into account by an exponential correction value or B-factor. The judicious application of structure factor correction with an appropriate B-factor allows for non-biased map sharpening. In cryoEM, deviations in structure factor come from several mechanisms such as beam-induced motion, radiation damage, conformational flexibility, multiple scattering, and computational errors due to poor particle alignment. At present there is no rigorous and published methodology for deciphering the multiple sources of error that comprise the gross calculated B-factor from a cryoEM dataset; however, such investigations are currently in progress with specimen motion or beam-induced drift being regarded as a primary source of information loss [12].

In RELION 3.0, both lateral motion correction and map sharpening are carried out within its Bayesian particle polishing routine [69]. By motion correcting individual particles prior to sharpening, B-factor sharpening can best correct for radiation damage and computational errors alone. However, particle movement and especially that of the first frame is usually so great that computation motion correction is unable to correct for image blurring [70] hence the need for physical stability interventions. With the release of RELION 2.0, images within each movie stack were sharpened via a dose weighted relative B-factors of each frame within the stack [70]. Relative B-factors are utilized as single-frame images don't contain enough signal to estimate the entire structure factor. Relative B-factors describe how fast or slow the signal in reconstructions from individual frames drops with fre-

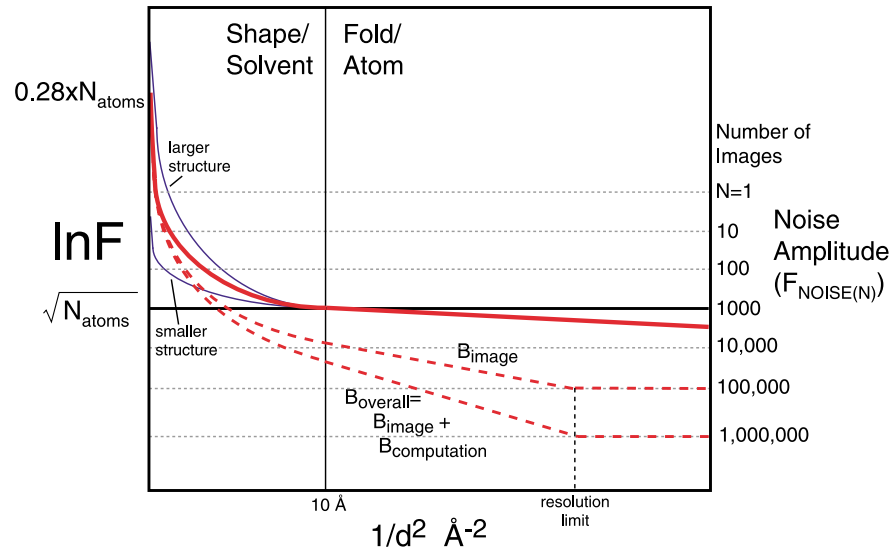


Figure 4.16: Guinier plot of the spherically averaged structure factor amplitude for a protein [68].

quency compared to the average reconstruction signal from all frames, and hence they can be positive or negative values. Relative B-factor weights for each frame are calculated with Equation 4.6 were $C_f$ is the y-axis intercept of the Fourier shell correlation and $B_f$ is the relative B-factor each for a given frame. Both values are explicitly provided from RELION whereby the relative weight envelope is computed with Equation 4.6.

$$w_f(v) = \frac{exp\left(\frac{B_f}{4}v^2 + C_f\right)}{\sum_{f'} w_{f'}(v)} \tag{4.6}$$

Comparing Figures 4.18 and 4.17 it can be clearly seen that the relative weight of the first frame highlighted in green is greater within the SWCNT dataset than in the control, thus indicating that more signal from first unirradiated is being utilized in for the maps reconstruction. As it was earlier confirmed that local movement for all frames was reduced by the use of SWCNTs, it could be assumed that the increase in the relative weight of the first frames is at least in part due this reduced movement and blurring. After initial 3D refinement utilizing the same reference density used for classification, CtfRefine and Bayesian polishing was carried out. Utilizing a solvent mask created from the initial 3D refinement postprocessing yielded a resolution of 3.5Å shown in Figure 4.19.

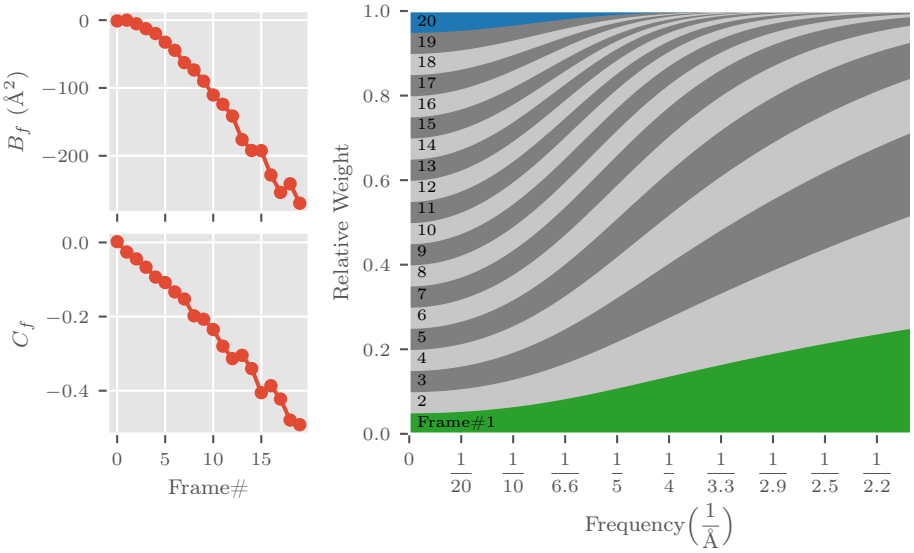


Figure 4.17: Relative B-factor weighting for β-galactosidase on SWCNT networks.

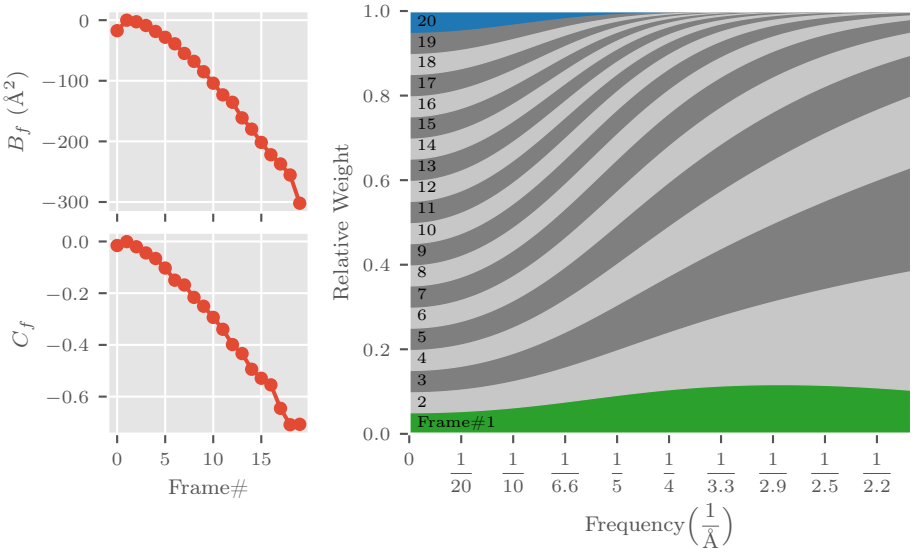


Figure 4.18: Relative B-factor weighting for β-galactosidase on a nominal gold UltrAuFoil® grid.

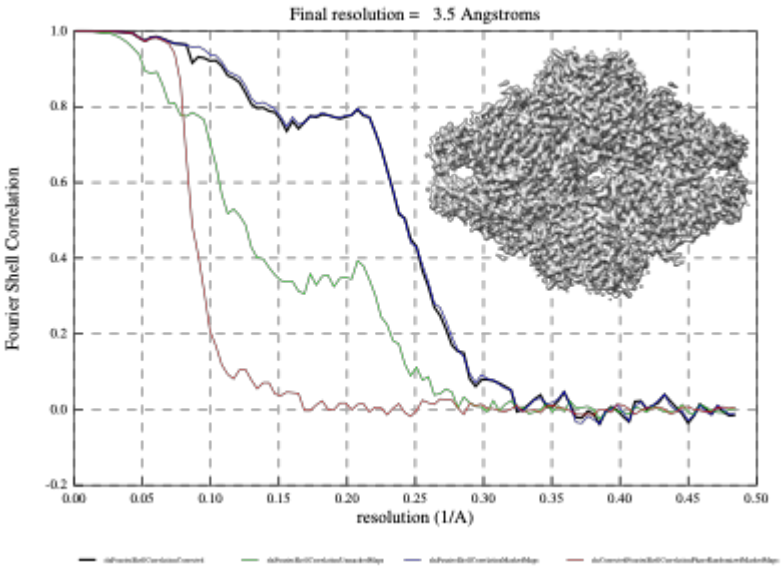


Figure 4.19: Fourier shell correlation and gold standard cuttoff resolution of β-galactosidase on SWCNTs. Inset: β-galactosidase structure.

## 4.4 Discussion

Many different factors and variables must be taken into consideration to obtain an optimal density map resolution, these include sample preparation protocols, microscopy protocols, and prudent data processing. The use of a SWCNT grids introduces a whole host of additional variables which alter both the sample itself and how it behaves under irradiation. With many variables in play, correlating differing experimental parameters to resulting resolutions is difficult.

Structures from the control and SWCNT grids are both presented with a fitted model from [63] in Figures 4.20a and 4.20b. The model from Bartesaghi was derived from a 3.2Å density map similar in resolution to those found in this study. Both maps correspond well to the fitted model with external loop densities being found in the higher resolution control map. Resolution maps were generated with ResMap 1.1.4 utilizing a 2-5Å resolution range and are shown in Figures 4.21a and 4.21b. Both maps display well behaved resolution contrast with nominal fidelity loss in the external flexible domains.

Importantly there exists no directional anisotropy or aliasing in either the density or resolution maps which indicates well balanced particle orientations within the ice meniscus. Euler angle distributions for both data sets are presented in Figure 4.22 and show SWCNT data to have distinctly different angular distributions than that of the control data. The control data display two very prominent arcs extending from the upper pole extending towards the 70° and 120° longitudes along with two separate diffuse lobes at the both extents of the bottom latitude. The SWCNT data orientations lay in a large diffuse region in the upper latitudes of the plot. The diamond shape of the β-galactosidase tetramer is not especially prone to preferential orientation, thus judging the degree of randomness between the two data sets is difficult.

Statistical metrics such as the Pearson correlation coefficient nominally used to detect linear correlations between two variables are not well suited to handle the non-linear nature that is expected in orientation data seen in Figure 4.22. A newer statistical measure known as the distance correlation can effectively measure both linear and non-linear correlations [71]. Similar to the Pearson correlation, a distance correlation of 0 indicates independent vectors while a value of 1 will indicate dependant vectors. Distance correlations on both SWCNT and control data sets were calculated with the dcor Python library and found to be 0.175 and 0.319 respectively. Thus it would seem to be that the degree of correlation is greater in the control data indicating that SWCNTs improve preferential orientation for β-galactosidase. As the particle population of the SWCNT data contains only non-conjugated

proteins the improvements in Eurler angle distributions cannot be attributed to circumferential bonding of the proteins around the SWCNT. It is more likely that the SWCNT imparts variable ice thickness which encourage the β-galactosidase particles to adopt more random orientations.

Both Figures 4.15 and 4.15 clearly demonstrate a reduction in beam-induced motion within the standard error of the measured particle populations. With such reduction in motions it should be the case that data coming from the SWCNT grids should provide improved particle contrast yielding higher a resolution given equal particle populations, which is not the case. With control and SWCNT data respectively providing 3.2Å and 3.5Å density maps in spite of favourable beam-induced motion vectors, it can be surmised that additional variables are contributing to the lack of resolution in the experimental data.

Inspection of defocus lengths and maximum resolution values shown in Figure 4.23 reveals the troubling truth behind the lack of resolution coming from the experimental dataset. With control data having a median defocus value of 0.577μm compared to the experimental data having a value of 1.24μm there is no doubt as to the principal cause of the apparent discrepancy in overall resolutions. This experimental error is a result of having to compare data collected during separate sessions and in doing so overlooking this one critical value. From the defocus value histograms, it can be seen that the SWCNT data have considerably less outliers then that of the control data, this is a consequence of motion attenuation from the SWCNTs.

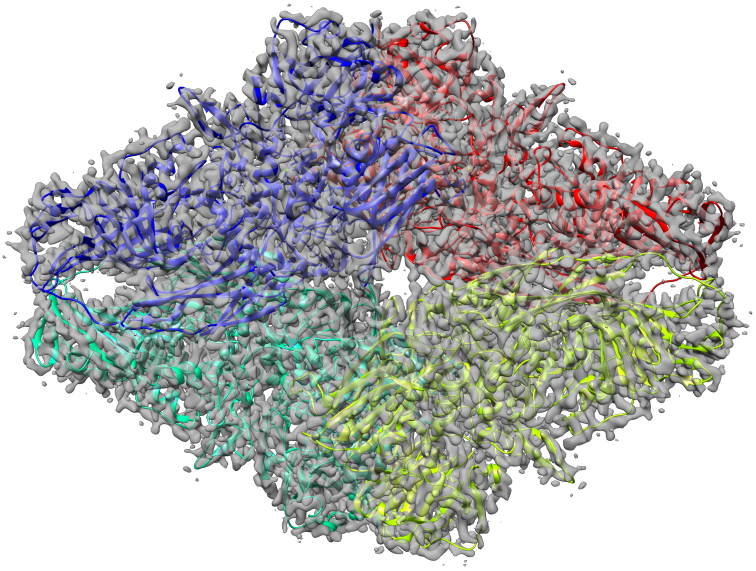

(a) Control data

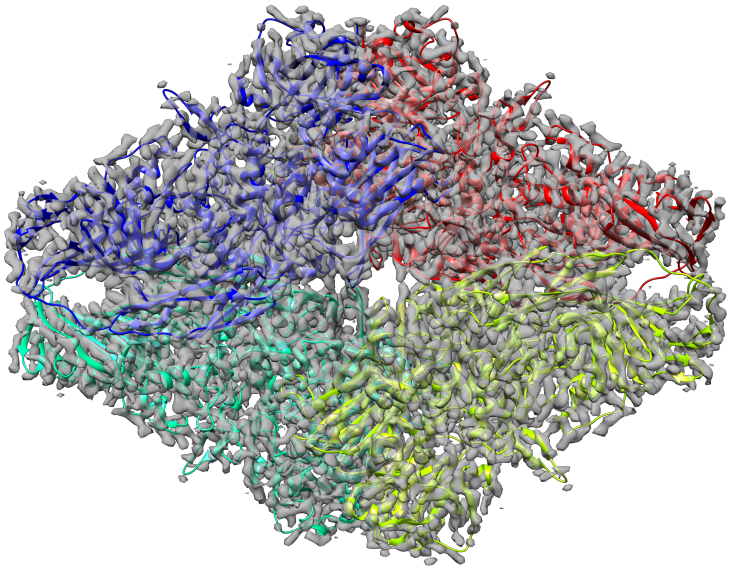

(b) SWCNT data

Figure 4.20: Final density maps fitted with model from [63].

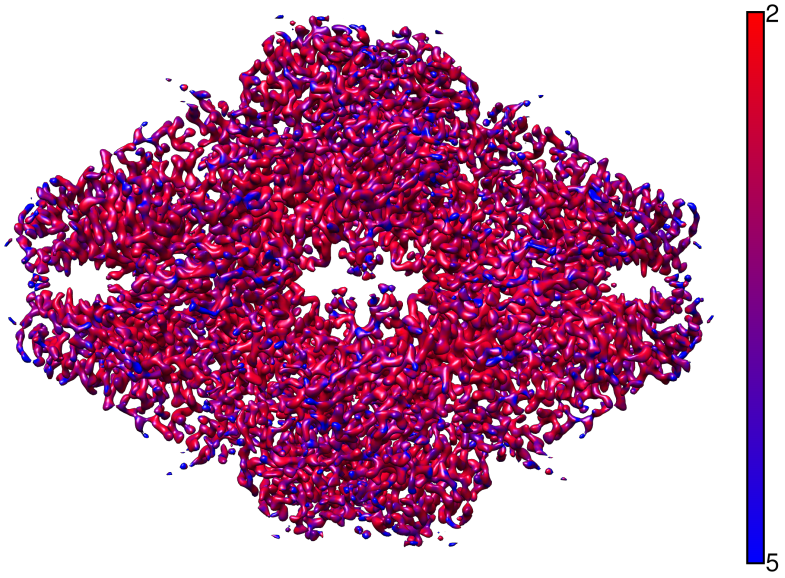


(a) Control data

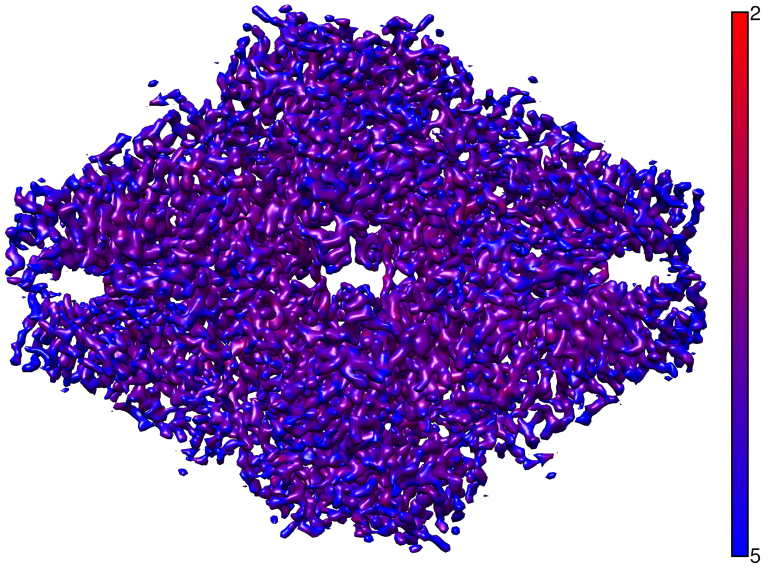


(b) SWCNT data

Figure 4.21: Final local resolution maps (scale in Å)

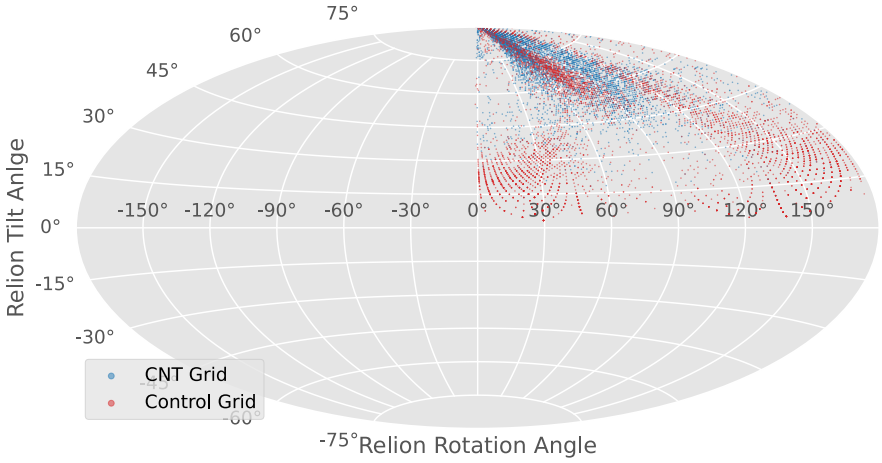


Figure 4.22: Particle orientation distribution

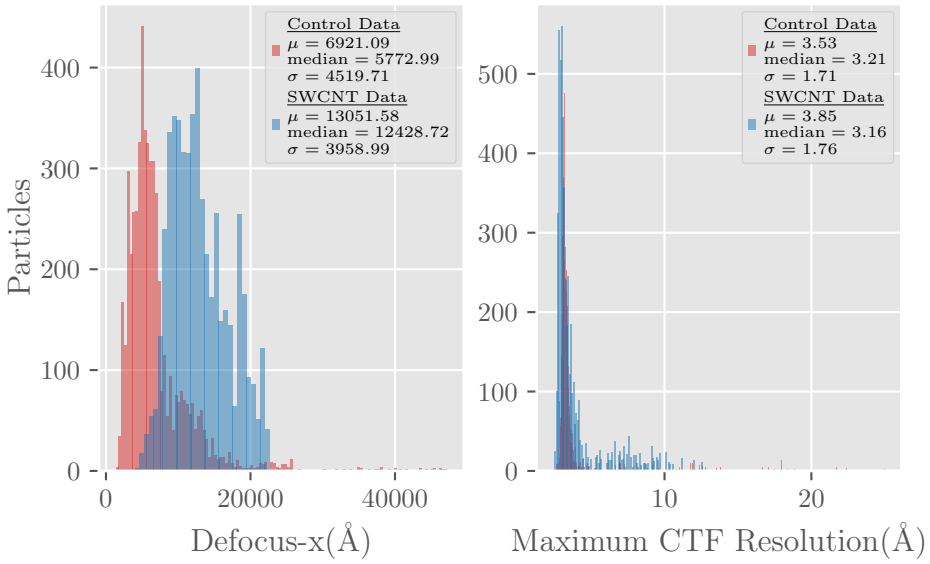


Figure 4.23: Per-particle defocus and maximum resolution histograms

# Chapter 5

# Selective Particle Capture with SWCNTs

## 5.1 Background

Initial proof of concept experimentation was designed with the intent of developing an affinity grid for on-grid purification of proteins or targets already in wide use. The polyhistidine-tag (HIS-tag) is one of the most regularly used tagging systems, thus it was deemed appropriate to design a SWCNT grid with a nitrilotriacetic acid NTA moiety that will bind with HIS-tags when charged with nickel ions. Selective bioconjugation with novel materials such as nanoparticles, SWCNTs or graphene has been vastly researched within the context of novel biological sensing [72], [73], but only recently in cryoEM [14]. Affinity grids are relatively unused and without well-known preparatory protocols as exists with more common fixation methods like glow discharging prior to cryo-plunging or poly–L–lysine treatments for optical microscopy. The chemical functionalizations developed herein revolve around methodologies used in biosensing and are intended to be pragmatic in nature as to be easily deployed within a typical structural biology laboratory. Without the facilities to handle and manipulate bulk powder SWCNTs in an appropriate manner, the application of anchoring moieties on SWCNTs was the first and primary concern. Since being first discovered in 1991, SWCNTs have had an array functionalization strategies developed to augment their utility [74].

Most literature of the past makes of use of covalent modification of the lattice of the nanotubes themselves with use of the acids or non-ambient annealing with various gasses as can be seen in Figure 5.1. Refluxed acid treatments and annealing were likely first used in initial functionalization methods as similar protocols were already commonly used to grow and purify SWCNT

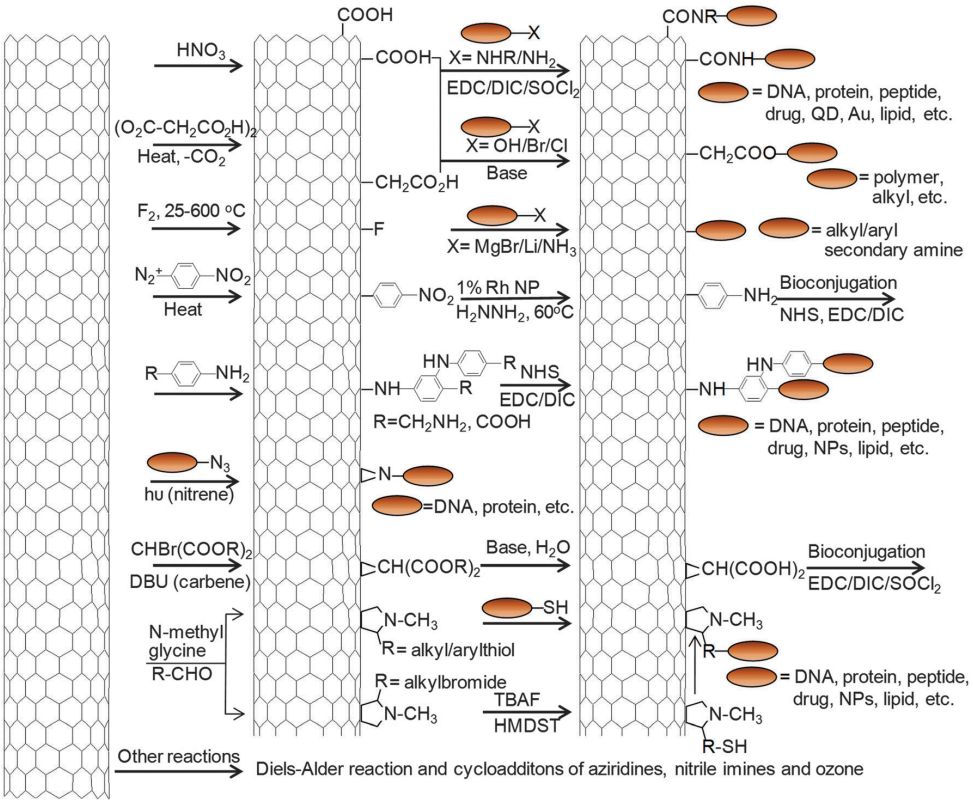


Figure 5.1: Carbon nanotube functionalization methods [74]

from bulk powder [75], needless to say many these techniques are not readily available to most structural biology labs. As well as being inconvenient to deploy, covalent functionalization also modifies the native crystal structure of the SWCNT thereby degrading their inherently high electrical and thermal conductivity [76], [77]. With the ever-growing use of carbon nanotubes within industry and academia alike, functionalization has as of recent focused on non-covalent methods for enhancing solubility within various solvents or polymer matrixes. Common methods of functionalization for enhanced solubility include the use of steric stabilization using agents that non-selectively wrap around the tube such as SDS, Tween, DNA, or proprietary polymers as is the case the SWCNTs utilized in this project. Non-covalent SWCNT functionalization can also be carried out with aromatic moieties through $\pi - \pi$ interactions that maintain the native crystal structure of the SWCNT. As described in Chapter 3, the extraordinary electrical properties of SWCNT are native properties of their hexagonal carbon lattice. Thus any alteration of the underlying crystal will serve to limit or altogether shunt native electrical properties. Non-covalent functionalization has be achieved with a variety of

different aromatic compounds such as pyrene [78], triptycene [79], triphenylene [80] along with others. Among the various aromatic compounds utilized for SWCNT sidewall functionalization, pyrene was seen as logical starting point for initial experimentation as it is both widely used and commercially available with many different terminal ligands that allow further functionalization.

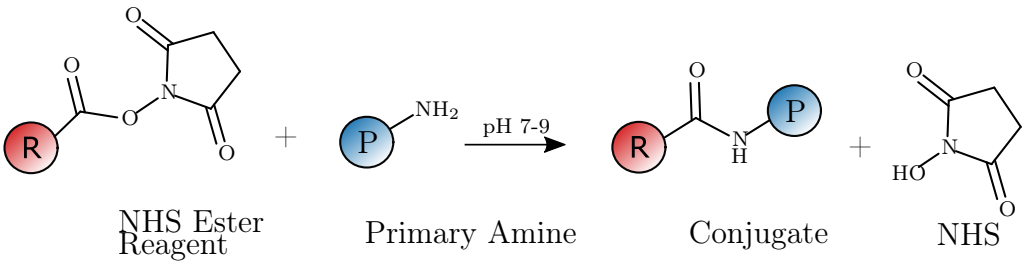


Figure 5.2: Generic NHS reaction scheme

## 5.2 On-Grid SWCNT Functionalization

Basic pyrene constituents offered by Sigma Aldrich include amine, carboxylic and N–hydroxysuccinimide (NHS) esters as terminal tags. NHS reactive chemistry is one of the most common methods of conjugating amine containing compounds or the N-terminus of a protein in aqueous physiological conditions. As is shown in Figure 5.2, NHS crosslinks with active amines within slightly alkaline conditions to produce a stable amide bond which releases a hydrolysed NHS molecule. In order to use NHS chemistry to create a pyrene anchored nitrilotriacetic acid ligand, one of the reactive species must contain pyrene. In this project, 1–Pyrenebutyric acid NHS ester constituted the NHS Ester Reagent seen in Figure 5.2 while the Primary Amine is represented by N$\alpha$,N$\alpha$–Bis(carboxymethyl)–L–lysine hydrate. The principle concern with using NHS chemistries with our reagents is that pyrene molecules are not water soluble, thus the ligand can't easily be synthesized in a one pot reaction. A solution to this problem can be found in the fact that this ligand is intended specifically to alter SWCNTs for EM grids, thus the pyrene–NHS can be first bound to SWCNTs that are already deposited atop a grid and then removed from the pyrene–NHS solution. This allows for sequential reactions that build the ligand on the SWCNT surface as seen in Figure 5.3 without the need to solubilize reagents such that they can react in a common solution. While sequentially functionalizing SWCNT is conceptually easy and efficient, it makes precise chemical characterization of the assembled ligand extremely difficult. It is preferential to have the isolated conjugate such that nuclear magnetic resonance (NMR) can verify the ligand's chemical composition. With ligands built up in situ quantitative characterization techniques like NMR are impossible however surface characterization methods such as X-ray photoelectron spectroscopy (XPS) can qualitatively indicate the presence of surface functional groups.

Fabrication of NTA–SWCNT affinity grid started with the dropcasting of 15$\mu$L NanoIntegris IsoNanotubes–M® metallic SWCNTs on a nominal 400 mesh gold TEM grid. It was critical to utilize a bare grid without any carbon networks as these surfaces may also adsorb pyrene moieties. Using gold grids is also a necessity as NTA moieties will be exposed to nickel salt to form the NTA–$Ni^{+2}$ complex, typical copper grids will to some extent be oxidized in the presence of these reagents. 1–pyrenebutyric acid N–hydroxysuccinimide ester (pyrene–NHS) obtained from Sigma Aldrich was dissolved in dry DMF to form a 5mM solution in which SWCNT grids were incubated at room temperature for two hours. After incubation the grids were rinsed in fresh DMF to remove excess reagents and allowed to air dry.

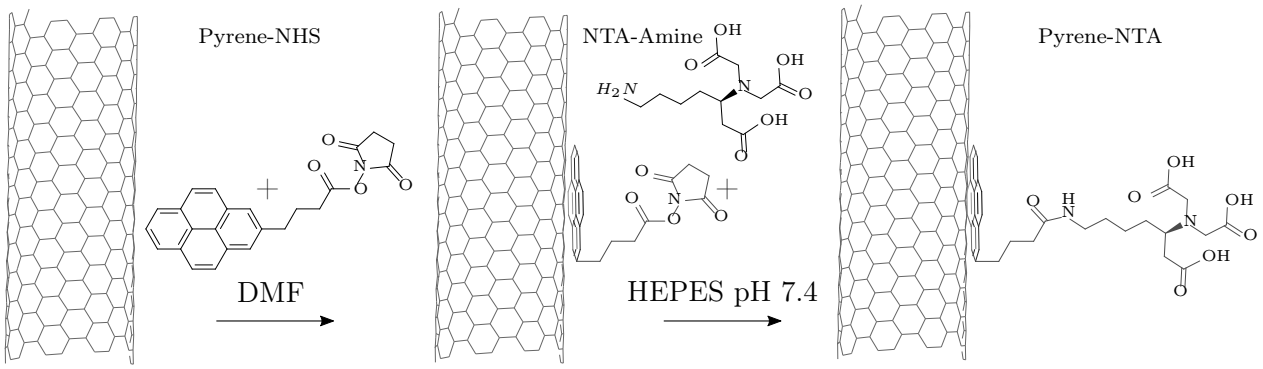


Figure 5.3: Non-covalent SWCNT–NTA functionalization scheme

N$\alpha$,N$\alpha$–Bis(carboxymethyl)–L–lysine (NTA–amine) also from Sigma Aldrich was dissolved in a 0.3mM HEPES pH 7.4 buffer to form a 7mM solution. The pyrene–NHS SWCNT grids were incubated in the NTA–amine–HEPES solution for 5 hours at room temperature after which they were rinsed with pure HEPES buffer. The above two reaction protocols were adapted from previous publications [81], [82]. With the desired NTA moiety anchored the SWCNTs, the grids were further incubated in a 0.1M $NiSO_4$ solution for 20 minutes to form the final NTA–$Ni^{+2}$ complex, after which the grids were washed in and stored in HEPES buffer until further use.

## 5.3 Particle Capture Characterization

As mentioned previously, obtaining a quantifiable structure of a surface bound ligand is not possible and with this in mind, fast-track experimentation with HIS-tagged proteins was seen as the best avenue for demonstrating selective target capture. Within the Laboratory for Biomolecular Research at the PSI many different groups will often produce HIS-tagged proteins as by-product from expression and purification. At the time of this experiment, green fluorescent protein (GFP) was freshly cleaved and available. GFP is a 26.9 kDa protein isolated from the jellyfish *Aequorea victoria*. When exposed to light in the blue-ultraviolet range, GFP exhibits a bright green fluorescence, several other marine organisms also produce such similar proteins. In molecular biology GFP is often use as reporter of expression. By mutating proteins that are to be cloned with GFP genes, one can monitor the desired protein throughout its expression via fluorescence microscopy. The GFP obtained for further experimentation was the by-product from the work of Jaeger et. Al [83] and was cleaved from its primary expression target with human Rhinovirus 3C protease. Figure 5.4 illustrates a model of GFP used in the following experiment, its genetic sequence is provided in Appendix B. The model shown in Figure 5.4 was predicted by Iterative Threading ASSEmbly Refinement (I-TASSER) from the Yang Zhang lab of the University of Michigan, Ann Arbor [84]. A hefty deca-histidine sequence was expressed on the N-terminus of the GFP to ensure proper binding to the NTA–$Ni^{+2}$ complex is depicted in red within the bottom left corner of Figure 5.4.

With a molecular probe capable of selective binding the SWCNT–NTA–$Ni^{+2}$, a fluorescent microscopy assay was developed to validate selective capture of HIS-tagged targets. Affinity grids were first taken from solution storage, briefly blotted as to remove the storage buffer and then incubated for 10 minutes with 4 µL of GFP–his. After incubation, the grid was manually agitated a in 0.1M HEPES buffer to remove GFP particles that are not selectively bound. Imaging was carried out on a Leica SP5 Confocal Microscope with a laser excitation wavelength of 485nm whilst viewing emissions at 520nm. A grid containing only functionalized SWCNTs without GFP was also imaged to control for autofluorescence that might result from the pyrene–SWCNT complex. After initial imaging both experimental and control samples, the experimental grid was washed with 1M imidazole in order to elute the bound HIS-tagged GFP and then re-imaged.

In Figure 5.5a, NTA–$Ni^{+2}$ functionalized SWCNTs are suspended between each grid bar with conjugated GFP–His. All the grids definitively show the fluorescent presence of GFP indicating successful conjugation which with-

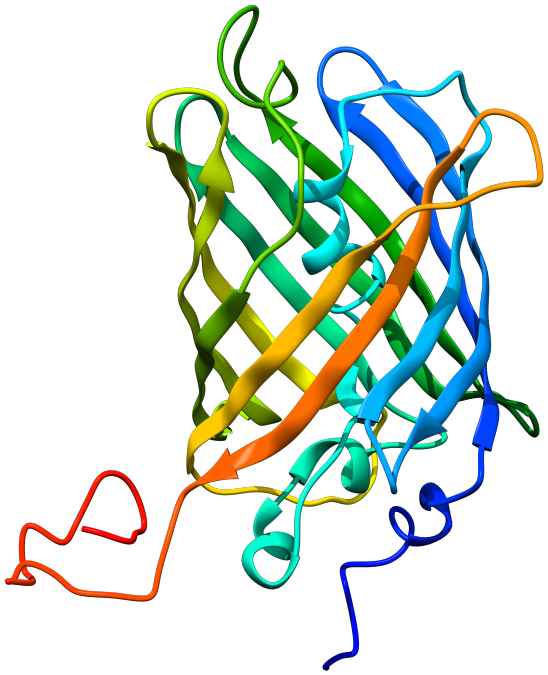

Figure 5.4: HIS-tag GFP model predicted by I-TASSER.

stood multiple washes in native buffer. The same GFP proteins were then successfully eluted in the presence of 1M imidazole which further validates selective protein capture. With negative control samples containing only functionalized SWCNTs displaying no autofluorescence it can be assumed that all fluorescence originates from the GFP alone.

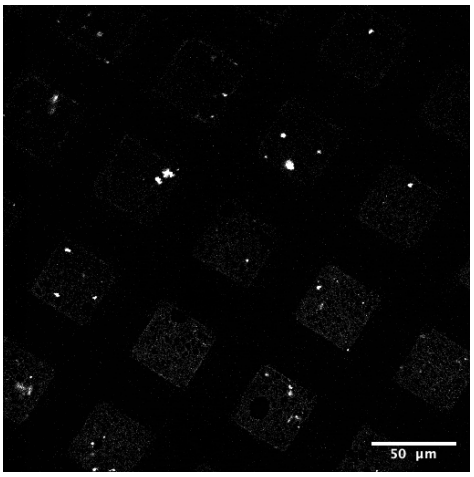


(a) Fluorescence image of HIS-tagged GFP protein on functionalized SWCNT–NTA–$Ni^{+2}$.

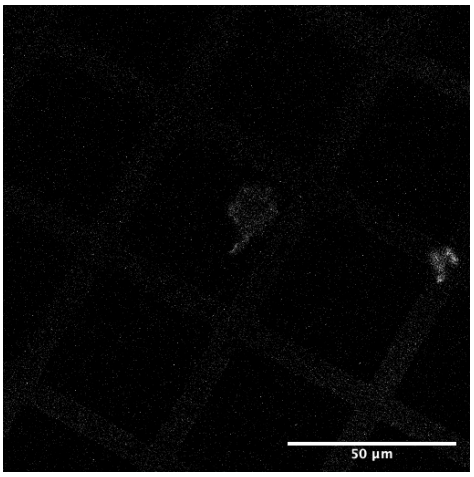


(b) Fluorescence image of negative control grid with only functionalized SWCNT–NTA–$Ni^{+2}$ without GFP.

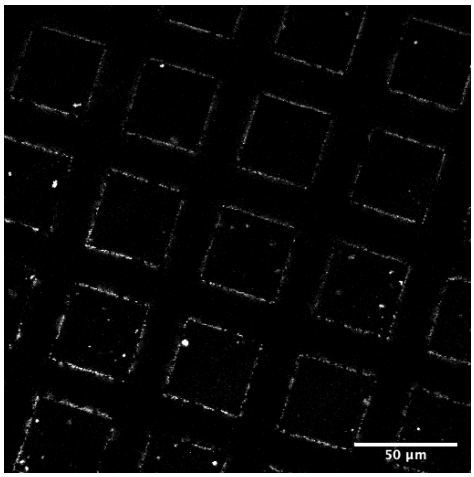


(c) Fluorescence image of HIS-tagged GFP protein on functionalized SWCNT–NTA–$Ni^{+2}$ eluted with 1M imidazole. The bright edges outlining grid meshes is likely the result of agglomerating GFP.

Figure 5.5: Optical flourescent microscopy images

## 5.4 Pyrene–NTA Conjugate Synthesis

The "on-grid" functionalization of SWCNTs previously shown was carried out primarily for deploy-ability; the above protocol can be carried out with the minimal reagents and lab equipment. It would be reasonably easy enough to synthesize a linker that is water soluble, however with pyrene being extremely polar the above reaction requires equipment not readily available in biochemistry laboratory. Hence, the following protocol and experiment was developed and carried out by Thomas Rohrbach of the Laboratory for Catalysis and Sustainable Chemistry at the PSI.

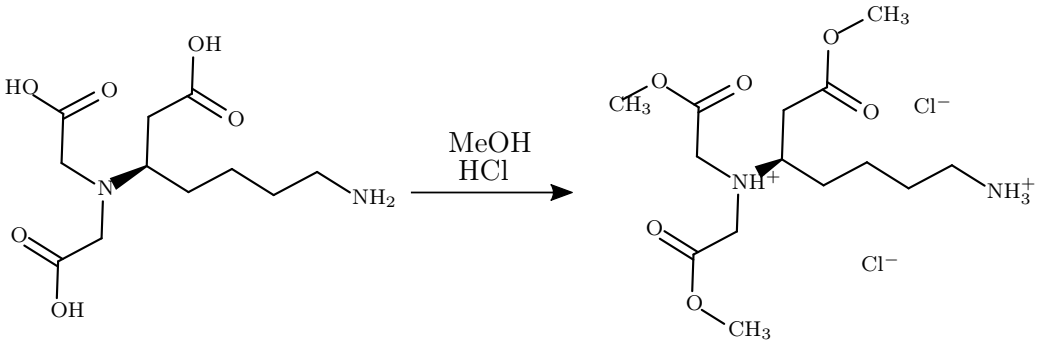


Figure 5.6: NTA–amine methylation.

Synthesis begins in earnest with the methylation of carboxylic groups of the NTA–amine as to protect them from reacting in subsequent synthesis steps. NTA–amine was mixed together with 10% HCl in methanol (MeOH). The mixture was stirred at 100°C for 45min in a Biotage microwave.

The methylated NTA moiety was seen to be the only product detected by ultra performance liquid chromatorgraphy (UPLC) and subsequently evaporated in acetonitrile (ACN). The methylated NTA salt was then reacted with pyrene–NTA in the presence of N,N-diisopropylethylamine (DIPEA) in dimethylformamide (DMF) for 1 hour at 23°C. DIPEA or triethylamine is a required as a basic catalyst in order to achieve efficient amine acylation. Methylated NTA–pyrene was the only reaction product detected with ultra performance liquid chromatorgraphy and was purified by CombiFlash® Rf+Lumen™ 50g-RediSep Rf Gold High Performance C18 columns. Collected fractions were then combined and evaporated. The synthesis was completed with the demethylation of protected carboxylic groups with a mixture of 2.2mM aqueous lithium hydroxide (LiOH), tetrahydrofuran (THF) and MeOH in a 1:2:1 ratio at 23°C for 16 hours. With no starting material detected by ultra performance liquid chromatorgraphy, the solution was precipitated drop-wise with 2N HCl (pH 1-2) and washed with ACN. Proton NMR

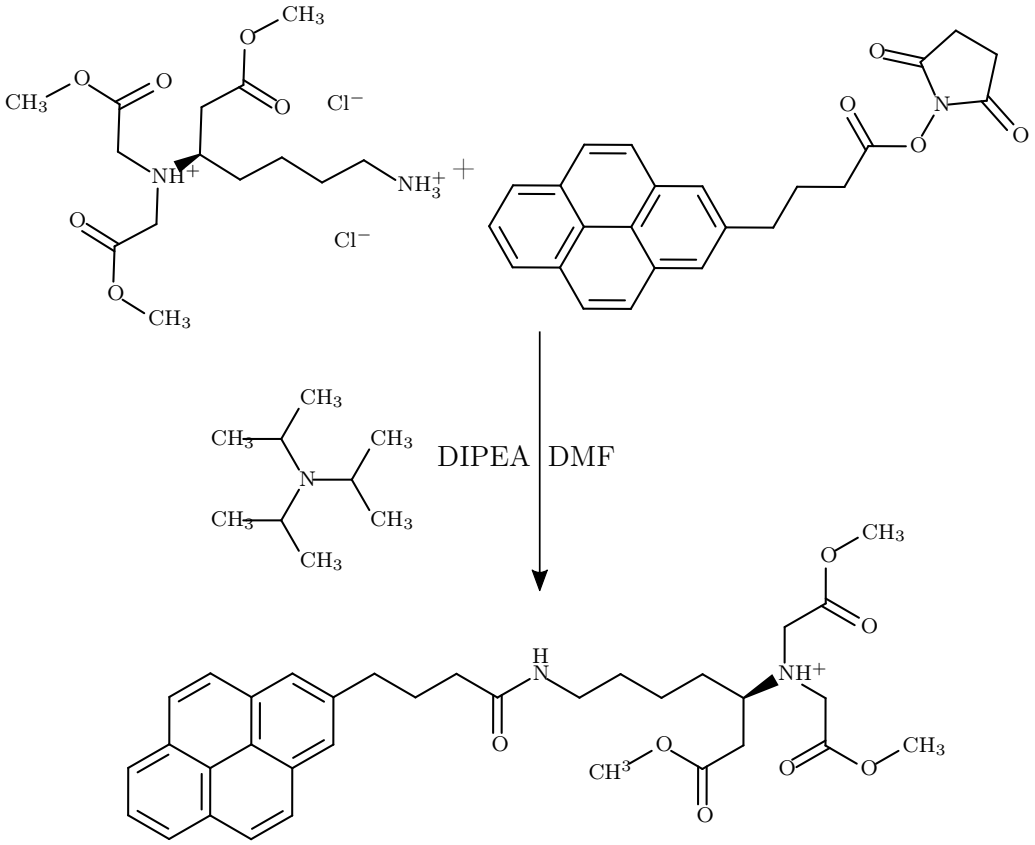


Figure 5.7: Succinimidyal acid ester reaction in DMF.

was carried out with the final product dissolved in deuterated dimethylsulfoxide. The NMR spectrum obtained was in good agreement with that which was simulated with the ChemNMR estimation tool in ChemDraw Professional 16. Both experimental and simulated spectra are shown in Appendix C.

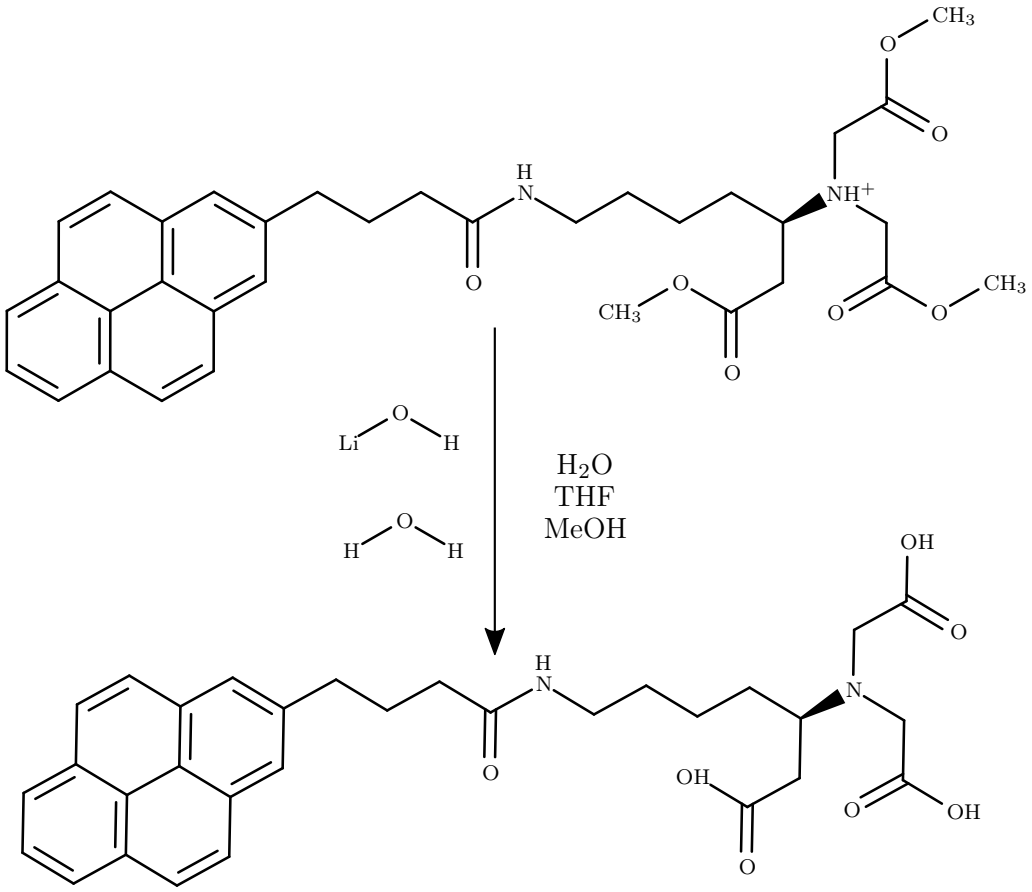


Figure 5.8: Removal of protection groups from final pyrene–NTA moiety.

## 5.5 Surface Functionalization Characterization

In the first on-grid conjugation and fluorescence assay of a pyrene–NTA moiety it was seen that the given chemical functionalization resulted selective capture of a HIS-tagged GFP protein. However, the exact nature of the selective can only be alluded as no chemical structure of the moiety was obtained prior to experimentation. By synthesizing a pure pyrene–NTA conjugate, the structure itself could be determined. Thus, the last chemical information required to assure a properly behaving selective binding system is to address the degree of binding of the pyrene–NTA moiety to the SWCNT. Herein the functionalization of aromatic carbon surfaces via $\pi - \pi$ stacking of the previously synthesized pyrene–NTA is characterized via XPS. While XPS is the most promising method for demonstrating surface functionalization, it is not without pitfalls, especially when functionalization carbon allotropes. As the X-rays given off in an XPS spectrum are proportional to the chemical bonds from which they were emitted, carbon will make up the bulk majority of the background signal coming from SWCNT and this signal must be contrasted against the predominately carbon-based signal coming from the pyrene–NTA itself.

While deciphering the two carbon signals isn't impossible, care must be taken and with this in mind initial experimentation began using highly oriented pyrolytic graphite (HOPG) as a substrate. It was thought that flat, ordered HOPG surface would provide a cleaner background with less intrinsic disorder than that of a SWCNT network which is random by nature. Initial experimentation was first attempted with functionalized HOPG samples. However, vacuum levels of the XPS loading chamber could not be attained with these specimens. It was assumed that the laminar substructure of the HOPG was impregnated with solvent that was slowly degassing and prevented proper vacuum from being established. To solve this issue, graphene substrates were used as replacement with the following procedures.

The above synthesized pyrene–NTA conjugate was dissolved to form a 10mM DMF solution to be subsequently used for all experimental trials. Graphene grown on copper foil via chemical vapour deposition purchased from Ted Pella was gently cut with shears to roughly 1cm * 1cm dimensions and used without further modification. The graphene/copper foils were immersed in the pyrene–NTA solution for the following incubation times: 2min, 1hour, 17hours. After incubation all samples were washed in DMF and allowed to dry in ambient conditions. A positive control sample was fabricated by allowing 10μL of conjugate solution to dry in place without further washing. A negative control sample of an untreated graphene/copper foil was also

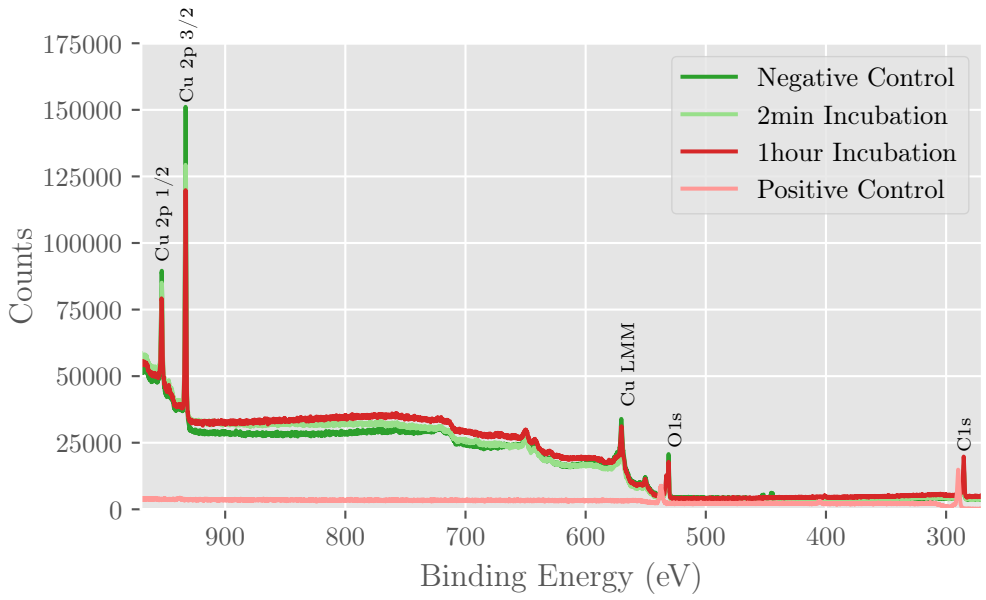


Figure 5.9: XPS survey scan of all pyrene–NTA functionalization trials of graphene on copper.

prepared. After functionalization all samples were pumped down to $10^{-10}$ mbar and XPS measurements were carried out utilizing monochromatic Al K$\alpha$ X-ray radiation at 0.05 eV energy steps. All XPS spectra were analysed and deconvoluted with CasaXPS.

From the preliminary survey scan presented in Figure 5.9 three copper peaks from the substrate can be easily seen, the largest of which (Cu 2p 3/2) was used to align all spectra. Prior to further analysis and deconvolution, all energy spectra were aligned to the Cu 2p peak and then fitted with a U2 Tougaard background. The 0.05 eV step size provided an exceptionally clean spectra for which no further smoothing was required. Deconvolution was performed without background subtraction or additional spectral alteration. All plotted data were normalized to flat energies strictly for display purposes. Examining the complete spectrum seen in Figure 5.9, it can be seen that the entire positive control spectrum is distinctively red shifted by approximately 5 eV, this red shift is seen throughout the entire positive control spectrum and is most likely the signal of an oxidization product from excessive charging of the thick layer of conjugate purposefully left on the graphene. The nitrogen peak is the most telling as there should not be any nitrogen signal on the graphene surface prior to incubation and thus indicates with some certainty that the base of the tri-acetic acid moiety is fixed on the surface.

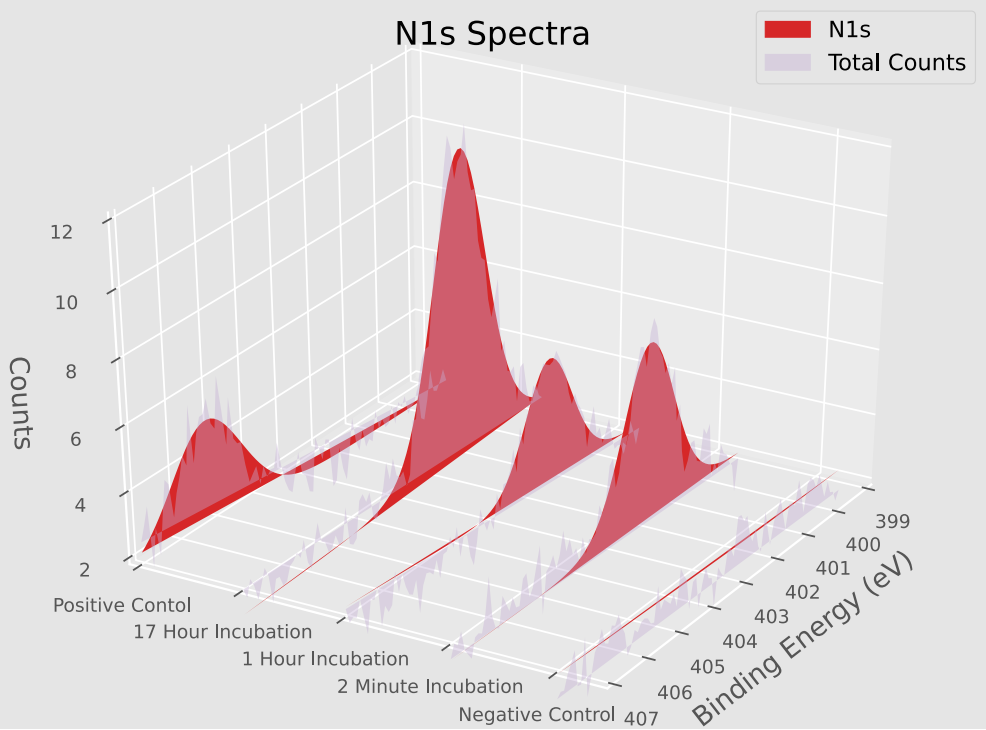


Figure 5.10: N1s spectra of all pyrene–NTA functionalization trials.

As seen in Figure 5.10 there exists little to no nitrogen signal in the untreated sample, with all other trials providing nitrogen peaks at approximately 400 eV. In Figure 5.10, the 405 eV peak seen in the positive control sample is possibly a signal coming from $NO^{-4}$ or possibly other nitrogen oxide states [85]. Looking at the Cu 2p peaks in Figure 5.9 it can be seen that the signal coming from the positive control sample is completely attenuated and hugging the x-axis of the plot. From this information, further credence is given to the prior assumption that N1s signals of the positive control are coming from the dried conjugate on the upper most surface of the sample. There was no correlation with nitrogen peak intensity to incubation time as one might expect, this non-time dependant behaviour is also seen in both O1s and C1s spectra. Possible explanations for this phenomenon could be due to the structure, thickness, and surface coverage of the ligand. It is possible that over-crowding of the ligand attenuates the nitrogen signal as additional pyrene's bind over existing ligands. As only one nitrogen exists in the ligand, it is most sensitive to attenuation from other atomic signals with might explain the why longer incubation times can result in diminishing signal. The

Table 5.1: Deconvoluted N1s peak positions and relative sensitivity factor (RSF) areas.

| Sample | Nitrogen | |
|---|---|---|
| | Position (eV) | Area (RSF) |
| Negative Control | 339.93 | 0 |
| 2 Minute Incubation | 401.16 | 3.71 |
| 1 Hour Incubation | 401.07 | 2.43 |
| 17 Hour Incubation | 400.73 | 6.40 |
| Positive Control | 405.21 | 2.97 |

essential proof of principal for ligand binding comes from the N1s spectra as there is negligible nitrogen presence in native CVD graphene. In addition, there are no other elemental signals in the N1s spectrum from either the ligand or the native graphene thus confirmation of the ligand's presences is effectively binary, the same cannot be stated for C1s and O1s spectra.

Analysis of the O1s peak is complicated by native oxides that ever-present in the graphene/Cu substrate [86]. Graphene synthesis is never 100% exact, and removing both external impurities and lattice defects from epitaxial grown graphene for large scale production has remained a stumbling block for commercialization [87]. Relevant defects and chemical adsorption that seen in graphene XPS spectra originate from adventitious $sp^3$ bound carbon (BE = 285.4 eV), hydroxides C–OH (BE = 286.7 eV) [88], and esters O–C=O (BE = 288.3 eV) [89]. Analysis of the negative control sample did in fact have all the above species represented with spectra closely resembling that found in highly cited literature [90]. Signals introduced into the C1s spectra that are not present in the native graphene system come from that of acetic groups –COOH (BE = 288.8 eV) [91]. The introduction of the –COOH signal presented complications as such a peak wouldn't maintain its energy position throughout the deconvolution of each trial. Complications like those experienced were expected to happen with such a crowded spectrum. With careful calibration and signal referencing of elemental standards using the same radiation one could better deconvolute such signals, however given that binding has been verified with N1s spectra and NMR have already confirmed the original ligand structures such analysis was deemed unnecessary. Only accounting for both carbon signals, hydroxides and esters, it can be seen that introduction of the ligand will generally increase the adventitious

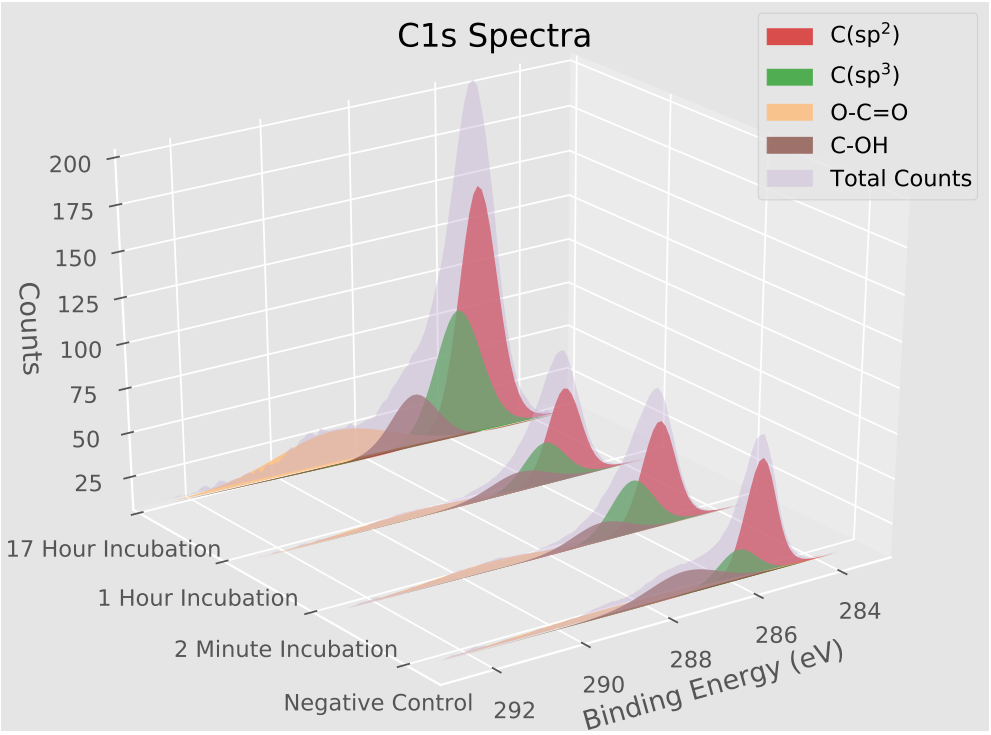


Figure 5.11: C1s spectra of all pyrene–NTA functionalization trials.

$sp^3$ carbon while native esters and hydroxyl groups are attenuated. While not completely clear, this can be interpreted as the ligand moieties covering the graphene surface and its associated defects seen in the negative control. Besides an obvious increase in adventitious carbon which is reasonable and indicative of ligand binding, not much can be said about hydroxyl groups with absolute certainty.

The O1s spectrum for native CVD graphene grown on copper will contain many oxidization states of carbon [91] within the C1s spectrum, namely: carbonyls C=O (BE = 531.1 eV), hydroxyl's C–O–H (BE = 532.3 eV), esters O–C=O (BE = 533.3 eV) and carboxyl's –COOH (BE = 534.2 eV). Like the C1s spectrum, it was possible to associate all of the above states to the negative control, however maintaining these energies peaks throughout each trial spectrum was difficult. From Figure 5.12, both C=O and C–OH peaks are very apparent in the spectrum and were the only signals deconvoluted from the data. As before it may have been possible to carefully fit additional peaks, however their energies would shift from sample to sample. With only two peaks a gross interpretation of generally increasing oxygen species can

Table 5.2: Deconvoluted C1s peak positions and area percentages.

| Sample | Binding Energy (eV) | | | | | | | |
|---|---|---|---|---|---|---|---|---|
| | 284.6 $C(sp^2)$ | | 285.4 $C(sp^3)$ | | 286.7 C–OH | | 288.3 O–C=O | |
| | Position (eV) | Area (%) | Position (eV) | Area (%) | Position (eV) | Area (%) | Position (eV) | Area (%) |
| Neg. Control | 285.09 | 44.43 | 285.61 | 15.45 | 286.86 | 21.54 | 288.26 | 18.59 |
| 2Min Incubation | 285.21 | 44.49 | 285.83 | 28.6 | 286.56 | 13.74 | 289.12 | 13.18 |
| 1Hr Incubation | 285.24 | 44.29 | 285.72 | 25.74 | 286.31 | 16.83 | 288.78 | 13.13 |
| 17Hr Incubation | 285.15 | 42.73 | 285.64 | 27.3 | 286.71 | 11.56 | 288.62 | 18.42 |

be seen especially when comparing the negative control to the 2 minute incubation. In general, the O1s shows a definitive increasing oxygen signal with the peak intensities of C=O bonds slowly equating to those of C–OH with higher incubation times.

As seen with all the spectra before, the 2 minute incubation presented signals with the best signal intensity and clearest peaks. Possibly the increased signal clarity of the 2 minute trial could be caused by non-homogeneous surface flatness or roughness which could provide a random signal boost to this sample, alternatively it could be that ligand stoichiometry provides an optimal signal with short incubation times. That is, with higher ligand concentration the signal will become attenuated by carbon which comprises the molecular bulk of the bound moiety. Finally, it could also be the case that excessive surface moieties contribute to deleterious surface charging that is not seen in the negative control or 2 minute incubation trial. It must be noted that incubations longer then several minutes are not that norm and were carried out as to rule out the possibility of insufficient incubation time.

Overall, we have proved the existence of nitrogen moiety's have bound to the graphene surface with XPS. This gives credibility that such binding will also take place on SWCNTs as the binding chemistries are identical for both these carbon allotropes. This work provides confidence for future selective binding experiments.

In conclusion, the synthesis of a pyrene–NTA–$Ni^{+2}$ selective binding ligand has been carried out in-situ on SWCNT EM grids and also in solution, with the later structures being verified via NMR. Binding of the pyrene–

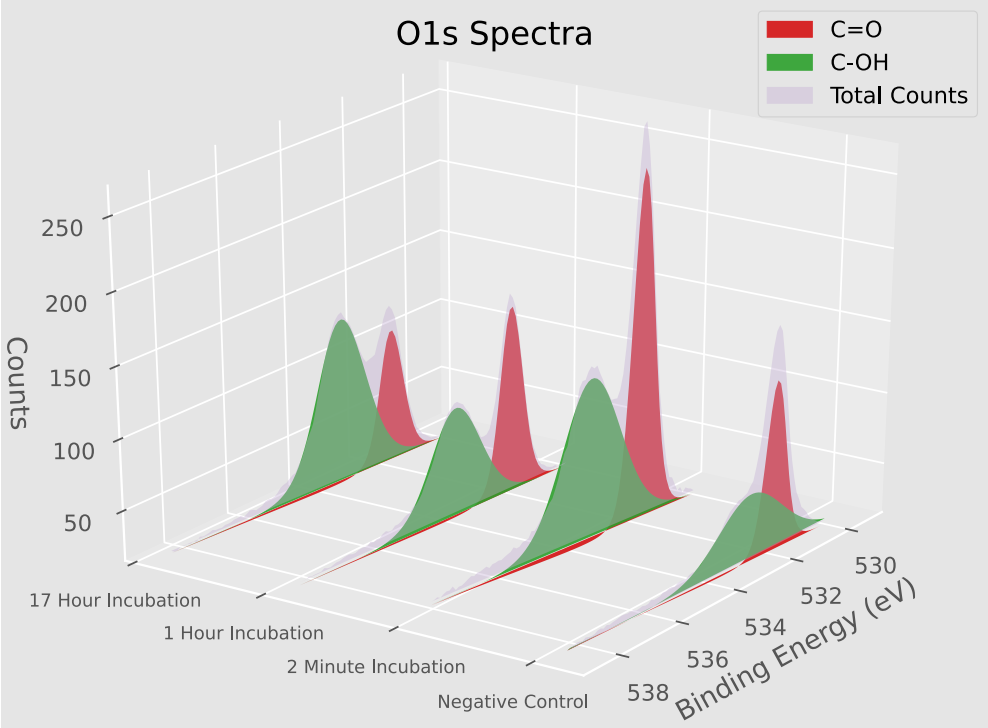


Figure 5.12: O1s spectra of all pyrene–NTA functionalization trials.

NTA ligand on $sp^2$ carbon was verified with XPS. Finally, selective capture behavior of HIS-tagged GFP proteins was observed with on-grid, in-situ synthesized pyrene–NTA–$Ni^{+2}$ ligands.

Table 5.3: Deconvoluted O1s peak positions and area percentages.

| Sample | Binding Energy (eV) | | | |
|---|---|---|---|---|
| | 531.1 C=O | | 532.3 C–OH | |
| | Position (eV) | Area (%) | Position (eV) | Area (%) |
| Negative Control | 530.95 | 40.96 | 531.8 | 53.5 |
| 2 Minute Incubation | 530.95 | 44.04 | 532.72 | 55.96 |
| 1 Hour Incubation | 531 | 43.99 | 532.9 | 56.01 |
| 17 Hour Incubation | 530.81 | 28.72 | 532.48 | 71.28 |

# Chapter 6

# Conclusion

In such unprecedented times the need to conduct structural biological studies cannot be underestimated. Modern cryoEM has radically changed the scientific landscape allowing for the atomic mapping of biological molecules without the need for crystallization or the utilization of large facilities such as synchrotrons or free electron lasers. The development of purpose-built low energy cryogenic microscopes promises to further lower capital barriers for research and thus it is imperative to further develop and improve cryoEM methodologies. This body of research aimed to study the role that SWCNTs can play in reducing beam-induced motion and also streamlining sample preparation with selective chemical probes.

The principal hypotheses within this project were that the inclusion of SWCNTs within the vitreous meniscus of a cryoEM sample would attenuate beam-induced motion due to mechanical reinforcement and also inhibited preferential orientation. Both these hypotheses were found to be true. Particle motions from experiments with both nanoparticles and proteins were found to have less motion when using SWCNT networks compared to control trials without. Euler angle distributions of particles within SWCNT networks were also found to have less preferential orientation then those of the control according to distance correlations. The reduction in beam-induced motion resulted in greater B-factor weightings of the first frames indicating that more information from the first several frames were utilized to build the map. On account of known experimental errors the increased information use of the first frames did not yield resolution enhancement, but it is likely that revisiting this experiment will provide favourable results. Subsequently, the same SWCNT networks were functionalized with a pyrene–NTA moiety such that HIS-tagged proteins would undergo selectively binding to the network. Pyrene–NTA moieties were synthesized using two separate methods with the later structures being verified by NMR. Binding of the pyrene–NTA moiety

to a SWCNT homologue, graphene, was verified with XPS. In addition a refined description of beam-induced charging and motion of cryoEM samples was described.

This body of work presents a repository of engineering protocols which can be enhanced through further experimentation. Such experimentation includes the controlled deposition of SWCNT networks utilizing printing methods, along with computational approaches to filter out SWCNTs making it possibly utilized proteins conjugated to SWCNT. Synthesis methods explored in this work can also be applied in the fabrication of chemical moieties with longer linkers in conjunction with stronger selective binding chemistries such as biotin. With fine tuning and refinement the techniques and methods explored here could be utilized within a standard cryoEM workflow as means to reduce beam-induced motion whilst allowing expedient sample preparation through selective binding.

# Appendix A

# Data Manipulation Scripts

## A.1 CryoSPARC Metadata Harvesting

The below script was utilized to pull both local and global motions from within cyroSPARC's internal job directories than normalize for global motion and output a three dimensional NumPy array containing every particles x,y coordinates (in pixels) for each frame and is formatted as such: [frame, coordinates(x,y),particle]. With these standardized NumPy arrays, datasets from different experiments can be easily manipulated and evaluated.

```python
#!/usr/bin/env python3
# -*- coding: utf-8 -*-
"""
Created on Mon Oct  1 14:37:38 2018
@author: borsa_c
"""

import matplotlib.pyplot as plt
import numpy as np
import os

plt.close('all')

#Input Directories for Trajectory Data BELOW
ExperimentDescription = "Fiducials-EXPORT_woCNTs60degrees"
WholeFrameM_path = "/Users/borsa_c/Dropbox/Fiducials/EXPORT_woCNTs60degrees/J16"
LocalMotion_path = "/Users/borsa_c/Dropbox/Fiducials/EXPORT_woCNTs60degrees/J34"

#Data Entry and Conditioning
Motion={}

#Finding Local Trajectory Files
for root, dirs, files in os.walk(LocalMotion_path):
    for name in files:
        if name.endswith(".npy"):
          Motion[name[0:19]]=[np.load(root+'/'+name)]

#Finding Global Trajectory Files
for root, dirs, files in os.walk(WholeFrameM_path) :
    for name in files:
        if name.endswith(".npy") and name[0:9] in Motion.keys() :
            movie=name[0:9]
            Motion[movie].append(np.load(root+'/'+name))
            Motion[movie].append(Motion[movie][0]- Motion[movie][1])

#Stacking Numpy array
for key in Motion:
    try: #Exception to form first instance of the array
        array
    except NameError:
        array=Motion[key][2]
    else:
        array=np.vstack((Motion[key][2],array))

#Swapping Numpy Axis for each array in Motion and put into a numpy array
array = np.rollaxis(array,0,3)

# %% Saving Numpy Array to output file
np.save(ExperimentDescription,array)
```

## A.2 STAR File Parsing I

Parsing STAR files, crystallographic CIF or CSV files is best done using dedicated parsers; this project made extensive use of the cif.read() method from the CIF toolbox of the GEneral MacroMolecular I/O (GEMMI) Python library. The cif.read() method returns a data module that can be converted to a JSON file which is then passed to a Python dictionary and then subsequently to a pandas dataframe. The resulting structure is a dictionary where each data block of the STAR file hashes to a dataframe. While somewhat clumsy this allows for seamless parsing of most STAR files. However, the CIF parser is sensitive to non-conforming STAR files and will return runtime errors when trying to parse them.

```
1.  #!/usr/bin/env python3
2.  # -*- coding: utf-8 -*-
3.  """
4.  Created on Wed Mar 18 10:40:10 2020
5.  @author: borsa_c
6.  """
7.  import json
8.  import pandas as pd
9.  from gemmi import cif
10. # %% StarFile Parse
11. cf = cif.read('/Users/borsa_c/Desktop/downloads/J29/local_motion_corrected_particle
    s.star')
12. dic=json.loads(cf.as_json())
13. df=pd.DataFrame.from_dict(dic['images'])
```

## A.3 STAR File Parsing II

On occasion, RELION will output non-conforming STAR files that contain large blank spaces resulting in run time faults of GEMMI's CIF parser. The script below was originally developed early in the project before stumbling upon dedicated parsing tools and as such was relegated as obsolete. However, the code below is useful for parsing non-conforming STAR files for which cif.read() will return runtime errors. Much like the nominal parsing routine described before, it returns a dictionary for each data block in the STAR file that are each hashed to a panadas dataframe. Whilst bulky and memory inefficient, the below script is robust.

```
#!/usr/bin/env python3
# -*- coding: utf-8 -*-
"""
Created on Sat Mar  9 15:33:00 2019
@author: borsa_c
"""
import pandas as pd
import matplotlib.pyplot as plt
import numpy as np
plt.close('all')

STARfile = "/Users/borsa_c/Desktop/s2nAveraging/2019-05-17-Averaged-
Control/job186/run_it024_half2_model.star"

##################Data Parsing and Conditioning#################################
STARfileData=[line.strip().split() for line in open(STARfile)]
data=[]
dfdic={}
block=False

for i in range(0,len(STARfileData)):
    if STARfileData[i]==[] and block==False: #dealing with blank lists
        continue
    elif STARfileData[i]==[] and block==True:
        if loop==False:
            dfdic[title]=pd.DataFrame(data, index=header).astype('float',errors='ig
nore')
            block=False
        elif loop==True:
            dfdic[title]=pd.DataFrame(data, columns=header).astype('float',errors='
ignore')
            block=False

    elif STARfileData[i][0].startswith("data_")==True:
        title=STARfileData[i][0] #title=movie+'_'+STARfileData[i][0] -
> This is the key entry which must be altered when downloading multiple files
        loop=False
        header=[]
        data=[]

    elif STARfileData[i][0].startswith("loop_")==True:
        loop=True

    elif STARfileData[i][0].startswith("_rln")==True and loop==False:
        header.append(STARfileData[i][0])
        data.append(STARfileData[i][1])
        block=True

    elif STARfileData[i][0].startswith("_rln")==True and loop==True:
        header.append(STARfileData[i][0])
        block=True

    else:
        data.append(STARfileData[i])
```

# Appendix B

# Green Fluorescent Protein Sequence

The following genetic sequence comprises the GFP proteins that were obtained as by products from Jaeger et Al. [83] and used for affinity grid validation. The models produced by I–TASSER utilized the below sequence beginning from the right of 3C protease cutting site.

3C Protease cutting site
C-terminus of CCR7
eGFP
Linkers
His-Tag

LGCLSGGRLEVLFQ/GPAAGSGEFKGEELFTGVVPILVELDGDVNGHKFSVSGEGEGDATYGKLTLKFICTT
GKLPVPWPTLVTTLTYGVQCFSRYPDHMKRHDFFKSAMPEGYVQERTISFKDDGNYKTRAEVKFEGDTLV
NRIELKGIDFKEDGNILGHKLEYNYNSHNVYITADKQKNGIKANFKIRHNIEDGSVQLADHYQQNTPIGDGP
VLLPDNHYLSTQSALSKDPNEKRDHMVLLEFVTAAGITHGMDELYKASGHHHHHHHHHH*

# Appendix C

# NMR Data

## C.1 Simulated Spectra

Proton NMR spectras of the final pyrene-NTA moiety in deuterated DMSO were obtained by the ETH NMR service centre. The obtained spectrum is in good agreement with that which is simulated in ChemNMR and verify the presence of the desired product.

ChemNMR $^{1}$H Estimation

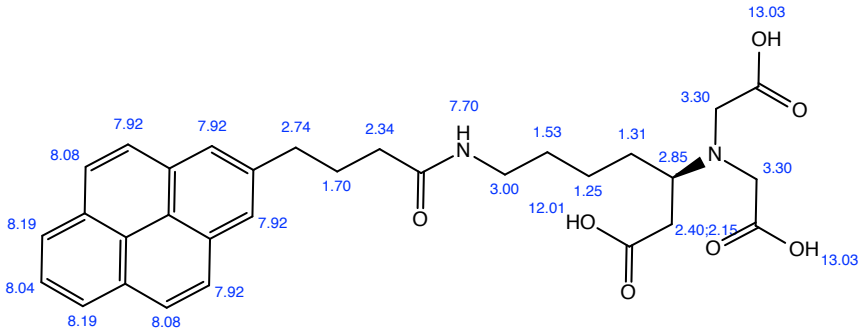


Estimation quality is indicated by color: good, medium, rough

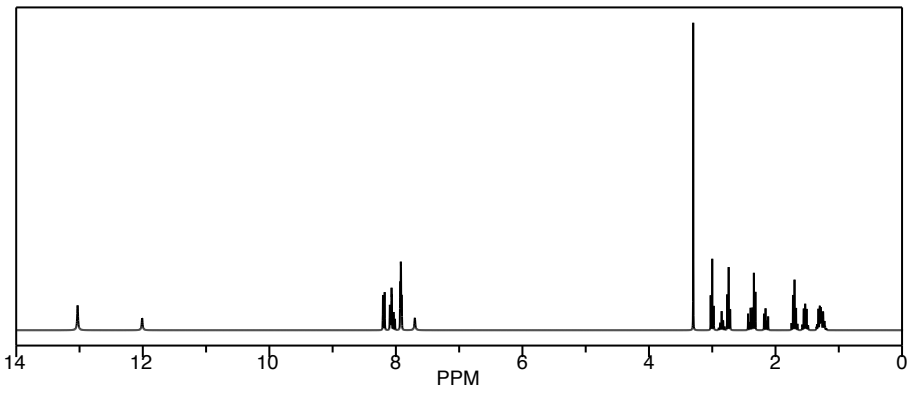

Protocol of the H-1 NMR Prediction (Lib=SU Solvent=DMSO 300 MHz):

| Node | Shift | Base + Inc. | Comment (ppm rel. to TMS) |
|---|---|---|---|
| OH | 13.03 | 11.00 | carboxylic acid |
| | | 0.00 | 1 -C |
| | | 2.03 | general corrections |
| OH | 13.03 | 11.00 | carboxylic acid |
| | | 0.00 | 1 -C |
| | | 2.03 | general corrections |
| OH | 12.01 | 11.00 | carboxylic acid |
| | | 0.00 | 1 -C |
| | | 1.01 | general corrections |
| NH | 7.70 | 7.00 | sec. amide |
| | | 0.50 | 1 -C |
| | | 0.00 | 1 -C from sec. amideC |
| | | 0.20 | general corrections |
| CH | 7.92 | 8.12 | phenanthrene |
| | | -0.08 | 1 -CC from 1-benzene |
| | | -0.12 | general corrections |
| CH | 8.19 | 7.88 | phenanthrene |
| | | 0.31 | general corrections |
| CH | 7.92 | 7.88 | phenanthrene |
| | | -0.08 | 1 -CC from 1-benzene |
| | | 0.12 | general corrections |
| CH | 7.92 | 7.71 | phenanthrene |
| | | 0.21 | general corrections |
| CH | 8.08 | 7.71 | phenanthrene |
| | | 0.37 | general corrections |
| CH | 7.92 | 7.71 | phenanthrene |
| | | 0.21 | general corrections |
| CH | 8.08 | 7.71 | phenanthrene |
| | | 0.37 | general corrections |
| CH | 8.19 | 8.12 | phenanthrene |
| | | 0.07 | general corrections |
| CH | 8.04 | 7.82 | phenanthrene |
| | | 0.22 | general corrections |
| CH | 2.85 | 1.50 | methine |
| | | 1.13 | 1 alpha -N |
| | | 0.32 | 1 beta -C(=O)O |
| | | -0.10 | 1 beta -C |
| CH2 | 3.30 | 1.37 | methylene |
| | | 1.03 | 1 alpha -N(C)C |
| | | 0.90 | 1 alpha -C(=O)O |
| CH2 | 3.30 | 1.37 | methylene |
| | | 1.03 | 1 alpha -N(C)C |
| | | 0.90 | 1 alpha -C(=O)O |
| CH2 | 3.00 | 1.37 | methylene |
| | | 1.87 | 1 alpha -NC(=O)-C |
| | | -0.06 | 1 beta -C |
| | | -0.18 | general corrections |
| CH2 | 2.74 | 1.37 | methylene |
| | | 1.33 | 1 alpha -1:C*C*2:C*C(*C*C*C*C*2)*C*C*1 |
| | | -0.06 | 1 beta -C |
| | | 0.10 | general corrections |
| CH2 | 2.40;2.145000 | 1.37 | methylene |
| | | 0.90 | 1 alpha -C(=O)O |
| | | 0.06 | 1 beta -N(C)C |
| | | -0.06 | 1 beta -C |
| CH2 | 2.34 | 1.37 | methylene |
| | | 0.85 | 1 alpha -C(=O)N |
| | | -0.06 | 1 beta -C |
| | | 0.18 | general corrections |
| CH2 | 1.31 | 1.37 | methylene |
| | | 0.06 | 1 beta -N(C)C |
| | | -0.06 | 1 beta -C |
| | | -0.06 | 1 beta -C |
| CH2 | 1.53 | 1.37 | methylene |
| | | 0.22 | 1 beta -NC(=O)-C |
| | | -0.06 | 1 beta -C |
| CH2 | 1.70 | 1.37 | methylene |
| | | 0.29 | 1 beta -1:C*C*2:C*C(*C*C*C*C*2)*C*C*1 |
| | | 0.24 | 1 beta -C(=O)N |
| | | -0.20 | general corrections |
| CH2 | 1.25 | 1.37 | methylene |
| | | -0.06 | 1 beta -C |
| | | -0.06 | 1 beta -C |
| | | 0.00 | general corrections |

1H NMR Coupling Constant Prediction

| shift | atom index | coupling partner' | | constant | and vector |
|---|---|---|---|---|---|
| 13.03 | 30 | | | | |
| 13.03 | 25 | | | | |
| 12.01 | 40 | | | | |
| 7.70 | 21 | | | | |
| 7.92 | 4 | | | | |
| | | 11 | | 1.5 | H-C*C*C-H |
| | | 2 | | 1.5 | H-C*C*C-H |
| 8.19 | 16 | | | | |
| | | 15 | | 7.5 | H-C*C-H |
| | | 9 | | 1.5 | H-C*C*C-H |
| | | 14 | | 1.5 | H-C*CH*C-H |
| 7.92 | 2 | | | | |
| | | 10 | | 1.5 | H-C*C*C-H |
| | | 4 | | 1.5 | H-C*C*C-H |
| 7.92 | 10 | | | | |
| | | 9 | | 7.5 | H-C*C-H |
| | | 2 | | 1.5 | H-C*C*C-H |
| 8.08 | 12 | | | | |
| | | 11 | | 7.5 | H-C*C-H |
| | | 14 | | 1.5 | H-C*C*C-H |
| 7.92 | 11 | | | | |
| | | 12 | | 7.5 | H-C*C-H |
| | | 4 | | 1.5 | H-C*C*C-H |
| 8.08 | 9 | | | | |
| | | 10 | | 7.5 | H-C*C-H |
| | | 16 | | 1.5 | H-C*C*C-H |
| 8.19 | 14 | | | | |
| | | 15 | | 7.5 | H-C*C-H |
| | | 12 | | 1.5 | H-C*C*C-H |
| | | 16 | | 1.5 | H-C*CH*C-H |
| 8.04 | 15 | | | | |
| | | 16 | | 7.5 | H-C*C-H |
| | | 14 | | 7.5 | H-C*C-H |
| 2.85 | 33 | | | | |
| | | 32 | | 7.0 | H-C-CH-H |
| | | 34 | | 7.0 | H-C-CH-H |
| 3.30 | 26 | | | | |
| 3.30 | 31 | | | | |
| 3.00 | 37 | | | | |
| | | 36 | | 7.1 | H-CH-CH-H |
| 2.74 | 17 | | | | |
| | | 18 | | 7.1 | H-CH-CH-H |
| 2.27 | 32 | diastereotopic | | -12.4 | H-C-H |
| | | 33 | | 7.0 | H-CH-C-H |
| 2.34 | 19 | | | | |
| | | 18 | | 7.1 | H-CH-CH-H |
| 1.31 | 34 | | | | |
| | | 33 | | 7.0 | H-CH-C-H |
| | | 35 | | 7.1 | H-CH-CH-H |
| 1.53 | 36 | | | | |
| | | 37 | | 7.1 | H-CH-CH-H |
| | | 35 | | 7.1 | H-CH-CH-H |
| 1.70 | 18 | | | | |
| | | 17 | | 7.1 | H-CH-CH-H |
| | | 19 | | 7.1 | H-CH-CH-H |
| 1.25 | 35 | | | | |
| | | 34 | | 7.1 | H-CH-CH-H |
| | | 36 | | 7.1 | H-CH-CH-H |

## C.2 Experimental Spectra

Below are the experimental H-NMR spectra of the final pyrene-NTA synthesis product.

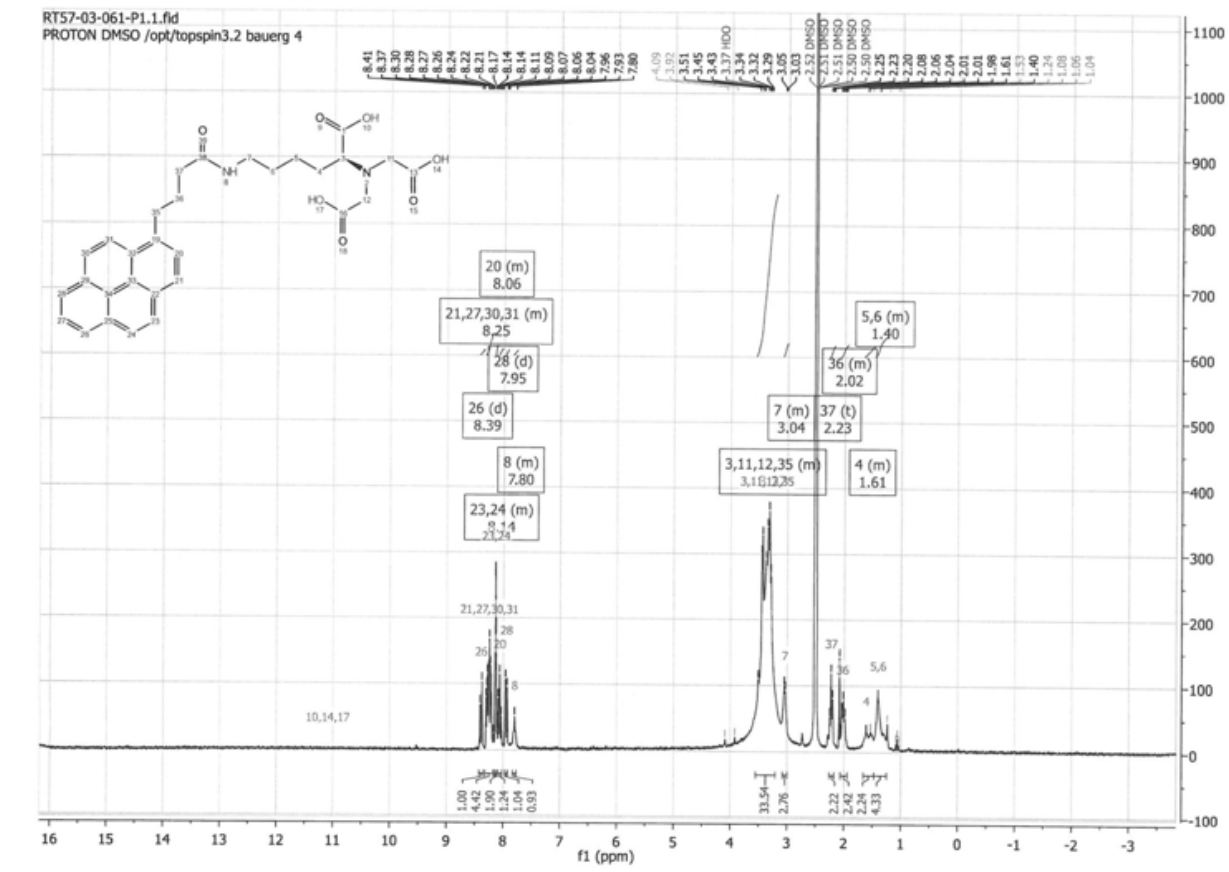

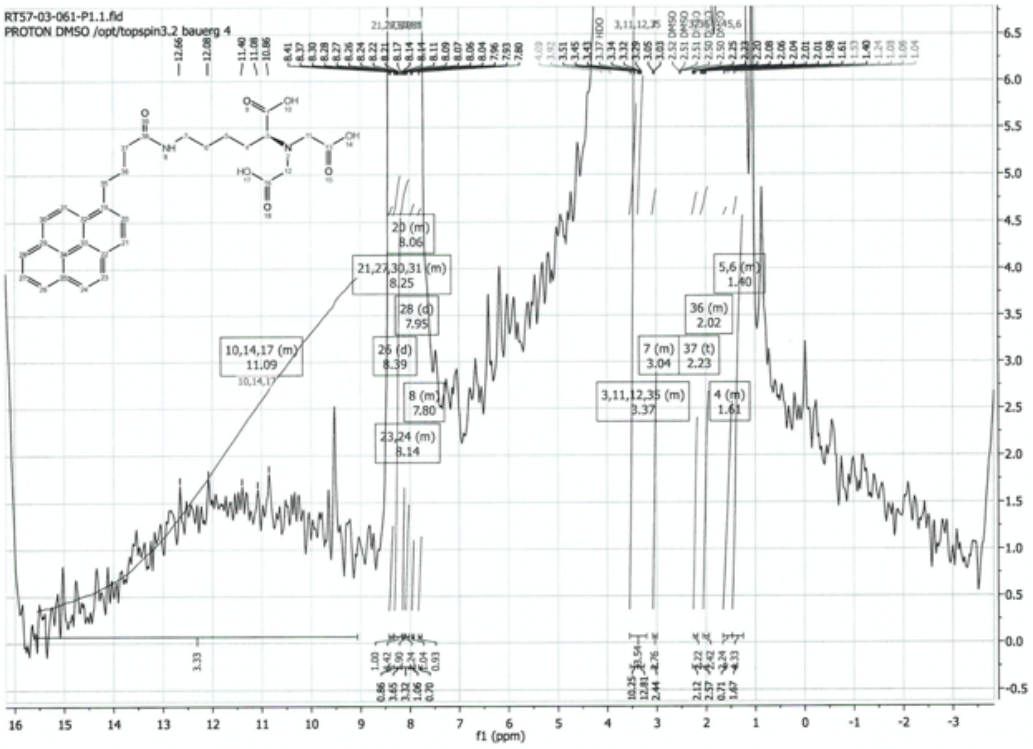
RT57-03-061-P1.1.fid
PROTON DMSO /opt/topspin3.2 bauerg 4
20 (m)
8.06
21,27,30,31 (m)
8.25
28 (d)
7.95
26 (d)
8.39
10,14,17 (m)
11.09
8 (m)
7.80
23,24 (m)
8.14
36 (m)
2.02
7 (m)
3.04
37 (t)
2.23
5,6 (m)
1.40
3,11,12,35 (m)
3.37
4 (m)
1.61
f1 (ppm)

# Bibliography


[1] J. D. Bernal and D. Crowfoot, "X-Ray Photographs of Crystalline Pepsin," en, *Nature*, vol. 133, no. 3369, pp. 794–795, May 1934, ISSN: 1476-4687. DOI: 10.1038/133794b0. [Online]. Available: https://www.nature.com/articles/133794b0 (visited on 01/09/2020).

[2] J. C. Kendrew, G. Bodo, H. M. Dintzis, R. G. Parrish, and H. Wyckoff, "A Three-Dimensional Model of the Myoglobin Molecule Obtained by X-Ray Analysis," *Nature*, vol. 181, pp. 662–666, Mar. 1958, ISSN: 0028-0836. DOI: 10.1038/181662a0. [Online]. Available: http://adsabs.harvard.edu/abs/1958Natur.181..662K (visited on 01/09/2020).

[3] D. J. D. Rosier and A. Klug, "Reconstruction of Three Dimensional Structures from Electron Micrographs," en, *Nature*, vol. 217, no. 5124, pp. 130–134, Jan. 1968, ISSN: 1476-4687. DOI: 10.1038/217130a0. [Online]. Available: https://www.nature.com/articles/217130a0 (visited on 01/17/2020).

[4] R. Henderson and P. N. T. Unwin, "Three-dimensional model of purple membrane obtained by electron microscopy," en, *Nature*, vol. 257, no. 5521, pp. 28–32, Sep. 1975, ISSN: 1476-4687. DOI: 10.1038/257028a0. [Online]. Available: https://www.nature.com/articles/257028a0 (visited on 01/20/2020).

[5] J. Dubochet and A. W. McDowall, "Vitrification of Pure Water for Electron Microscopy," en, *Journal of Microscopy*, vol. 124, no. 3, pp. 3–4, 1981, _eprint: https://onlinelibrary.wiley.com/doi/pdf/10.1111/j.1365-2818.1981.tb02483.x, ISSN: 1365-2818. DOI: 10.1111/j.1365-2818.1981.tb02483.x. [Online]. Available: https://onlinelibrary.wiley.com/doi/abs/10.1111/j.1365-2818.1981.tb02483.x (visited on 06/29/2020).

[6] J. Frank, J. Zhu, P. Penczek, Y. Li, S. Srivastava, A. Verschoor, M. Radermacher, R. Grassucci, R. K. Lata, and R. K. Agrawal, "A model of protein synthesis based on cryo-electron microscopy of the E. coli

ribosome," en, *Nature*, vol. 376, no. 6539, pp. 441–444, Aug. 1995, ISSN: 1476-4687. DOI: 10.1038/376441a0. [Online]. Available: https://www.nature.com/articles/376441a0 (visited on 01/20/2020).

[7] R. Henderson, "The potential and limitations of neutrons, electrons and X-rays for atomic resolution microscopy of unstained biological molecules," en, *Quarterly Reviews of Biophysics*, vol. 28, no. 2, pp. 171–193, May 1995, ISSN: 1469-8994, 0033-5835. DOI: 10.1017/S003358350000305X. [Online]. Available: https://www.cambridge.org/core/journals/quarterly-reviews-of-biophysics/article/potential-and-limitations-of-neutrons-electrons-and-xrays-for-atomic-resolution-microscopy-of-unstained-biological-molecules/D4FD094A3CA68FF6D8BE4878314DC72E (visited on 03/25/2019).

[8] A. R. Faruqi and R. Henderson, "Electronic detectors for electron microscopy," en, *Current Opinion in Structural Biology*, Carbohydrates and glycoconjugates / Biophysical methods, vol. 17, no. 5, pp. 549–555, Oct. 2007, ISSN: 0959-440X. DOI: 10.1016/j.sbi.2007.08.014. [Online]. Available: http://www.sciencedirect.com/science/article/pii/S0959440X07001212 (visited on 02/12/2020).

[9] G. McMullan, A. R. Faruqi, D. Clare, and R. Henderson, "Comparison of optimal performance at 300keV of three direct electron detectors for use in low dose electron microscopy," en, *Ultramicroscopy*, vol. 147, pp. 156–163, Dec. 2014, ISSN: 0304-3991. DOI: 10.1016/j.ultramic.2014.08.002. [Online]. Available: http://www.sciencedirect.com/science/article/pii/S030439911400151X (visited on 02/18/2020).

[10] A. F. Brilot, J. Z. Chen, A. Cheng, J. Pan, S. C. Harrison, C. S. Potter, B. Carragher, R. Henderson, and N. Grigorieff, "Beam-induced motion of vitrified specimen on holey carbon film," *Journal of Structural Biology*, vol. 177, no. 3, pp. 630–637, Mar. 2012, ISSN: 1047-8477. DOI: 10.1016/j.jsb.2012.02.003. [Online]. Available: http://www.sciencedirect.com/science/article/pii/S104784771200055X (visited on 01/09/2018).

[11] K. M. Yip, N. Fischer, E. Paknia, A. Chari, and H. Stark, "Breaking the next cryo-em resolution barrier – atomic resolution determination of proteins!" *bioRxiv*, 2020. DOI: 10.1101/2020.05.21.106740. eprint: https://www.biorxiv.org/content/early/2020/05/22/2020.05.21.106740.full.pdf. [Online]. Available: https://www.biorxiv.org/content/early/2020/05/22/2020.05.21.106740.

[12] R. Henderson and C. J. Russo, "Single Particle CryoEM: Potential for Further Improvement," en, *Microscopy and Microanalysis*, vol. 25, no. S2, pp. 4–5, Aug. 2019, ISSN: 1431-9276, 1435-8115. DOI: 10.1017/S1431927619000758. [Online]. Available: https://www.cambridge.org/core/journals/microscopy-and-microanalysis/article/single-particle-cryoem-potential-for-further-improvement/CC5540E87AC0887A26718B5F9011D5B7 (visited on 10/31/2019).

[13] C. J. Russo and L. A. Passmore, "Ultrastable gold substrates for electron cryomicroscopy," en, *Science*, vol. 346, no. 6215, pp. 1377–1380, Dec. 2014, ISSN: 0036-8075, 1095-9203. DOI: 10.1126/science.1259530. [Online]. Available: http://science.sciencemag.org/content/346/6215/1377 (visited on 01/10/2018).

[14] R. S. Pantelic, W. Fu, C. Schoenenberger, and H. Stahlberg, "Rendering graphene supports hydrophilic with non-covalent aromatic functionalization for transmission electron microscopy," *Applied Physics Letters*, vol. 104, no. 13, p. 134 103, Mar. 2014, ISSN: 0003-6951, 1077-3118. DOI: 10.1063/1.4870531. [Online]. Available: http://scitation.aip.org/content/aip/journal/apl/104/13/10.1063/1.4870531 (visited on 11/25/2016).

[15] R. S. Pantelic, J. W. Suk, Y. Hao, R. S. Ruoff, and H. Stahlberg, "Oxidative Doping Renders Graphene Hydrophilic, Facilitating Its Use As a Support in Biological TEM," *Nano Lett.*, vol. 11, no. 10, pp. 4319–4323, Oct. 2011, ISSN: 1530-6984. DOI: 10.1021/nl202386p. [Online]. Available: http://dx.doi.org/10.1021/nl202386p (visited on 06/20/2017).

[16] C. J. Russo and L. A. Passmore, "Controlling protein adsorption on graphene for cryo-EM using low-energy hydrogen plasmas," En, *Nature Methods*, vol. 11, no. 6, p. 649, Jun. 2014, ISSN: 1548-7105. DOI: 10.1038/nmeth.2931. [Online]. Available: https://www.nature.com/articles/nmeth.2931 (visited on 01/03/2018).

[17] J. Goldstein, D. E. Newbury, P. Echlin, D. C. Joy, A. D. R. Jr, C. E. Lyman, C. Fiori, and E. Lifshin, *Scanning Electron Microscopy and X-Ray Microanalysis: A Text for Biologists, Materials Scientists, and Geologists*, en, 2nd ed. Springer US, 1992, ISBN: 978-1-4612-7653-1. DOI: 10.1007/978-1-4613-0491-3. [Online]. Available: https://www.springer.com/gp/book/9781461276531 (visited on 05/04/2020).

[18] R. Henderson and R. M. Glaeser, "Quantitative analysis of image contrast in electron micrographs of beam-sensitive crystals," *Ultramicroscopy*, vol. 16, no. 2, pp. 139–150, Jan. 1985, ISSN: 0304-3991. DOI:

10.1016/0304-3991(85)90069-5. [Online]. Available: http://www.sciencedirect.com/science/article/pii/0304399185900695 (visited on 12/03/2018).

[19] T. Hudson, *Gold spider sem sample.jpg*, Mar. 2010. [Online]. Available: https://commons.wikimedia.org/wiki/File:Gold_Spider_SEM_sample.jpg.

[20] J. Brink, M. B. Sherman, J. Berriman, and W. Chiu, "Evaluation of charging on macromolecules in electron cryomicroscopy," en, *Ultramicroscopy*, vol. 72, no. 1, pp. 41–52, Apr. 1998, ISSN: 0304-3991. DOI: 10.1016/S0304-3991(97)00126-5. [Online]. Available: http://www.sciencedirect.com/science/article/pii/S0304399197001265 (visited on 10/30/2019).

[21] C. J. Russo and R. Henderson, "Charge accumulation in electron cryomicroscopy," en, *Ultramicroscopy*, vol. 187, pp. 43–49, Apr. 2018, ISSN: 0304-3991. DOI: 10.1016/j.ultramic.2018.01.009. [Online]. Available: http://www.sciencedirect.com/science/article/pii/S0304399117304291 (visited on 10/30/2019).

[22] A. F. Brilot, J. Z. Chen, A. Cheng, J. Pan, S. C. Harrison, C. S. Potter, B. Carragher, R. Henderson, and N. Grigorieff, "Beam-induced motion of vitrified specimen on holey carbon film," en, *Journal of Structural Biology*, vol. 177, no. 3, pp. 630–637, Mar. 2012, ISSN: 1047-8477. DOI: 10.1016/j.jsb.2012.02.003. [Online]. Available: http://www.sciencedirect.com/science/article/pii/S104784771200055X (visited on 05/02/2020).

[23] R. M. Glaeser, "Retrospective: Radiation damage and its associated "Information Limitations"," *Journal of Structural Biology*, JSB 50th Anniversary Issue, vol. 163, no. 3, pp. 271–276, Sep. 2008, ISSN: 1047-8477. DOI: 10.1016/j.jsb.2008.06.001. [Online]. Available: http://www.sciencedirect.com/science/article/pii/S1047847708001482 (visited on 12/03/2018).

[24] R. M. Glaeser and K. H. Downing, "Specimen Charging on Thin Films with One Conducting Layer: Discussion of Physical Principles," en, *Microscopy and Microanalysis*, vol. 10, no. 6, pp. 790–796, Dec. 2004, ISSN: 1435-8115, 1431-9276. DOI: 10.1017/S1431927604040668. [Online]. Available: https://www.cambridge.org/core/journals/microscopy-and-microanalysis/article/specimen-charging-on-thin-films-with-one-conducting-layer-discussion-of-physical-principles/76836A3EEAE90C9A24601094369C232E (visited on 06/18/2019).

[25] C. J. Russo and L. A. Passmore, "Progress towards an optimal specimen support for electron cryomicroscopy," *Current Opinion in Structural Biology*, vol. 37, pp. 81–89, Apr. 2016, ISSN: 0959-440X. DOI: 10.1016/j.sbi.2015.12.007. [Online]. Available: https://www.sciencedirect.com/science/article/pii/S0959440X15001931 (visited on 02/09/2017).

[26] R. E. Thorne, "Hypothesis for a mechanism of beam-induced motion in cryo-electron microscopy," en, *IUCrJ*, vol. 7, no. 3, pp. 416–421, May 2020, Number: 3 Publisher: International Union of Crystallography, ISSN: 2052-2525. DOI: 10.1107/S2052252520002560. [Online]. Available: https://journals.iucr.org/m/issues/2020/03/00/ua5002/ (visited on 06/22/2020).

[27] R. S. Pantelic, J. C. Meyer, U. Kaiser, W. Baumeister, and J. M. Plitzko, "Graphene oxide: A substrate for optimizing preparations of frozen-hydrated samples," *Journal of Structural Biology*, vol. 170, no. 1, pp. 152–156, Apr. 2010, ISSN: 1047-8477. DOI: 10.1016/j.jsb.2009.12.020. [Online]. Available: http://www.sciencedirect.com/science/article/pii/S1047847709003475 (visited on 03/26/2019).

[28] C. J. Benjamin, K. J. Wright, S. C. Bolton, S.-H. Hyun, K. Krynski, M. Grover, G. Yu, F. Guo, T. L. Kinzer-Ursem, W. Jiang, and D. H. Thompson, "Selective Capture of Histidine-tagged Proteins from Cell Lysates Using TEM grids Modified with NTA-Graphene Oxide," en, *Scientific Reports*, vol. 6, p. 32 500, Oct. 2016, ISSN: 2045-2322. DOI: 10.1038/srep32500. [Online]. Available: https://www.nature.com/articles/srep32500 (visited on 04/04/2018).

[29] D. Rhinow, N.-E. Weber, A. Turchanin, A. Gölzhäuser, and W. Kühlbrandt, "Single-walled carbon nanotubes and nanocrystalline graphene reduce beam-induced movements in high-resolution electron cryo-microscopy of ice-embedded biological samples," *Appl. Phys. Lett.*, vol. 99, no. 13, p. 133 701, Sep. 2011, Publisher: American Institute of Physics, ISSN: 0003-6951. DOI: 10.1063/1.3645010. [Online]. Available: https://aip.scitation.org/doi/abs/10.1063/1.3645010 (visited on 05/12/2020).

[30] N. Hu, K. Nunoya, D. Pan, T. Okabe, and H. Fukunaga, "Prediction of buckling characteristics of carbon nanotubes," en, *International Journal of Solids and Structures*, vol. 44, no. 20, pp. 6535–6550, Oct. 2007, ISSN: 0020-7683. DOI: 10.1016/j.ijsolstr.2007.02.043. [Online]. Available: http://www.sciencedirect.com/science/article/pii/S0020768307001114 (visited on 05/14/2020).

[31] J. Scherr, A. Neuhaus, K. Parey, N. Klusch, B. J. Murphy, V. Zickermann, W. Kühlbrandt, A. Terfort, and D. Rhinow, "Noncovalent Functionalization of Carbon Substrates with Hydrogels Improves Structural Analysis of Vitrified Proteins by Electron Cryo-Microscopy," *ACS Nano*, vol. 13, no. 6, pp. 7185–7190, Jun. 2019, ISSN: 1936-0851. DOI: 10.1021/acsnano.9b02651. [Online]. Available: https://doi.org/10.1021/acsnano.9b02651 (visited on 11/04/2019).

[32] H. W. Kroto, J. R. Heath, S. C. O'Brien, R. F. Curl, and R. E. Smalley, "C 60 : Buckminsterfullerene," en, *Nature*, vol. 318, no. 6042, pp. 162–163, Nov. 1985, Number: 6042 Publisher: Nature Publishing Group, ISSN: 1476-4687. DOI: 10.1038/318162a0. [Online]. Available: https://www.nature.com/articles/318162a0 (visited on 07/17/2020).

[33] E. OSAWA, "Superaromaticity," *Kagaku*, vol. 25, pp. 854–863, 1970. [Online]. Available: https://ci.nii.ac.jp/naid/10021261422/ (visited on 07/17/2020).

[34] S. Iijima and T. Ichihashi, "Single-shell carbon nanotubes of 1-nm diameter," en, *Nature*, vol. 363, no. 6430, pp. 603–605, Jun. 1993, Number: 6430 Publisher: Nature Publishing Group, ISSN: 1476-4687. DOI: 10.1038/363603a0. [Online]. Available: https://www.nature.com/articles/363603a0 (visited on 06/02/2020).

[35] K. S. Novoselov, A. K. Geim, S. V. Morozov, D. Jiang, Y. Zhang, S. V. Dubonos, I. V. Grigorieva, and A. A. Firsov, "Electric Field Effect in Atomically Thin Carbon Films," en, *Science*, vol. 306, no. 5696, pp. 666–669, Oct. 2004, Publisher: American Association for the Advancement of Science Section: Report, ISSN: 0036-8075, 1095-9203. DOI: 10.1126/science.1102896. [Online]. Available: https://science.sciencemag.org/content/306/5696/666 (visited on 06/02/2020).

[36] P. R. Wallace, "The Band Theory of Graphite," *Phys. Rev.*, vol. 71, no. 9, pp. 622–634, May 1947, Publisher: American Physical Society. DOI: 10.1103/PhysRev.71.622. [Online]. Available: https://link.aps.org/doi/10.1103/PhysRev.71.622 (visited on 06/03/2020).

[37] A. K. Geim and K. S. Novoselov, "The rise of graphene," in *Nanoscience and Technology*, Co-Published with Macmillan Publishers Ltd, UK, Aug. 2009, pp. 11–19, ISBN: 978-981-4282-68-0. DOI: 10.1142/9789814287005_0002. [Online]. Available: https://www.worldscientific.com/doi/abs/10.1142/9789814287005_0002 (visited on 06/03/2020).

[38] A. E. Karu and M. Beer, "Pyrolytic Formation of Highly Crystalline Graphite Films," *Journal of Applied Physics*, vol. 37, no. 5, pp. 2179–2181, Apr. 1966, Publisher: American Institute of Physics, ISSN: 0021-8979. DOI: 10.1063/1.1708759. [Online]. Available: https://aip.scitation.org/doi/abs/10.1063/1.1708759 (visited on 06/03/2020).

[39] C. Oshima and A. Nagashima, "Ultra-thin epitaxial films of graphite and hexagonal boron nitride on solid surfaces," en, *J. Phys.: Condens. Matter*, vol. 9, no. 1, pp. 1–20, Jan. 1997, Publisher: IOP Publishing, ISSN: 0953-8984. DOI: 10.1088/0953-8984/9/1/004. [Online]. Available: https://doi.org/10.1088%2F0953-8984%2F9%2F1%2F004 (visited on 06/03/2020).

[40] *Carbon monolayer phase condensation on Ni(111) - ScienceDirect*. [Online]. Available: https://www.sciencedirect.com/science/article/pii/0039602879903303 (visited on 06/03/2020).

[41] M. Monthioux and V. L. Kuznetsov, "Who should be given the credit for the discovery of carbon nanotubes?" en, *Carbon*, vol. 44, no. 9, pp. 1621–1623, Aug. 2006, ISSN: 0008-6223. DOI: 10.1016/j.carbon.2006.03.019. [Online]. Available: http://www.sciencedirect.com/science/article/pii/S000862230600162X (visited on 06/03/2020).

[42] C. Lee, X. Wei, J. W. Kysar, and J. Hone, "Measurement of the Elastic Properties and Intrinsic Strength of Monolayer Graphene," en, *Science*, vol. 321, no. 5887, pp. 385–388, Jul. 2008, Publisher: American Association for the Advancement of Science Section: Report, ISSN: 0036-8075, 1095-9203. DOI: 10.1126/science.1157996. [Online]. Available: https://science.sciencemag.org/content/321/5887/385 (visited on 06/03/2020).

[43] R. Zhang, Y. Zhang, Q. Zhang, H. Xie, W. Qian, and F. Wei, "Growth of Half-Meter Long Carbon Nanotubes Based on Schulz–Flory Distribution," *ACS Nano*, vol. 7, no. 7, pp. 6156–6161, Jul. 2013, Publisher: American Chemical Society, ISSN: 1936-0851. DOI: 10.1021/nn401995z. [Online]. Available: https://doi.org/10.1021/nn401995z (visited on 06/03/2020).

[44] M. S. Dresselhaus, G. Dresselhaus, and R. Saito, "Physics of carbon nanotubes," en, *Carbon*, Nanotubes, vol. 33, no. 7, pp. 883–891, Jan. 1995, ISSN: 0008-6223. DOI: 10.1016/0008-6223(95)00017-8. [Online]. Available: http://www.sciencedirect.com/science/article/pii/0008622395000178 (visited on 06/03/2020).

[45] L. Yang, M. P. Anantram, J. Han, and J. P. Lu, "Band-gap change of carbon nanotubes: Effect of small uniaxial and torsional strain," *Phys. Rev. B*, vol. 60, no. 19, pp. 13 874–13 878, Nov. 1999, Publisher: American Physical Society. DOI: 10.1103/PhysRevB.60.13874. [Online]. Available: https://link.aps.org/doi/10.1103/PhysRevB.60.13874 (visited on 05/26/2020).

[46] K. S. Novoselov, A. K. Geim, S. V. Morozov, D. Jiang, M. I. Katsnelson, I. V. Grigorieva, S. V. Dubonos, and A. A. Firsov, "Two-dimensional gas of massless Dirac fermions in graphene," en, *Nature*, vol. 438, no. 7065, pp. 197–200, Nov. 2005, Number: 7065 Publisher: Nature Publishing Group, ISSN: 1476-4687. DOI: 10.1038/nature04233. [Online]. Available: https://www.nature.com/articles/nature04233 (visited on 06/04/2020).

[47] M. S. Dresselhaus and G. Dresselhaus, "Intercalation compounds of graphite," *Advances in Physics*, vol. 51, no. 1, pp. 1–186, Jan. 2002, Publisher: Taylor & Francis _eprint: https://doi.org/10.1080/00018730110113644, ISSN: 0001-8732. DOI: 10.1080/00018730110113644. [Online]. Available: https://doi.org/10.1080/00018730110113644 (visited on 06/05/2020).

[48] J.-H. Chen, C. Jang, S. Xiao, M. Ishigami, and M. S. Fuhrer, "Intrinsic and extrinsic performance limits of graphene devices on SiO 2," en, *Nature Nanotechnology*, vol. 3, no. 4, pp. 206–209, Apr. 2008, Number: 4 Publisher: Nature Publishing Group, ISSN: 1748-3395. DOI: 10.1038/nnano.2008.58. [Online]. Available: https://www.nature.com/articles/nnano.2008.58 (visited on 06/08/2020).

[49] T. W. Ebbesen, H. J. Lezec, H. Hiura, J. W. Bennett, H. F. Ghaemi, and T. Thio, "Electrical conductivity of individual carbon nanotubes," en, *Nature*, vol. 382, no. 6586, pp. 54–56, Jul. 1996, Number: 6586 Publisher: Nature Publishing Group, ISSN: 1476-4687. DOI: 10.1038/382054a0. [Online]. Available: https://www.nature.com/articles/382054a0 (visited on 06/08/2020).

[50] K. Yanagi, H. Udoguchi, S. Sagitani, Y. Oshima, T. Takenobu, H. Kataura, T. Ishida, K. Matsuda, and Y. Maniwa, "Transport Mechanisms in Metallic and Semiconducting Single-Wall Carbon Nanotube Networks," *ACS Nano*, vol. 4, no. 7, pp. 4027–4032, Jul. 2010, ISSN: 1936-0851. DOI: 10.1021/nn101177n. [Online]. Available: http://dx.doi.org/10.1021/nn101177n (visited on 12/07/2017).

[51] R. Purohit, K. Purohit, S. Rana, R. Rana, and V. Patel, "Carbon nanotubes and their growth methods," *Procedia Materials Science*, vol. 6, pp. 716–728, 2014, 3rd International Conference on Materials Processing and Characterisation (ICMPC 2014), ISSN: 2211-8128. DOI: https://doi.org/10.1016/j.mspro.2014.07.088. [Online]. Available: http://www.sciencedirect.com/science/article/pii/S2211812814004532.

[52] M. C. Hersam, "Progress towards monodisperse single-walled carbon nanotubes," *Nature Nanotechnology*, vol. 3, no. 7, pp. 387–394, Jul. 2008, ISSN: 1748-3395. DOI: 10.1038/nnano.2008.135. [Online]. Available: https://doi.org/10.1038/nnano.2008.135.

[53] G. Ao, J. K. Streit, J. A. Fagan, and M. Zheng, "Differentiating Left- and Right-Handed Carbon Nanotubes by DNA," *J. Am. Chem. Soc.*, vol. 138, no. 51, pp. 16 677–16 685, Dec. 2016, Publisher: American Chemical Society, ISSN: 0002-7863. DOI: 10.1021/jacs.6b09135. [Online]. Available: https://doi.org/10.1021/jacs.6b09135 (visited on 06/09/2020).

[54] M. S. Arnold, A. A. Green, J. F. Hulvat, S. I. Stupp, and M. C. Hersam, "Sorting carbon nanotubes by electronic structure using density differentiation," en, *Nature Nanotechnology*, vol. 1, no. 1, pp. 60–65, Oct. 2006, Number: 1 Publisher: Nature Publishing Group, ISSN: 1748-3395. DOI: 10.1038/nnano.2006.52. [Online]. Available: https://www.nature.com/articles/nnano.2006.52 (visited on 06/09/2020).

[55] "Current intelligence bulletin 65: Occupational exposure to carbon nanotubes and nanofibers.," en-us, Oct. 2018. DOI: 10.26616/NIOSHPUB2013145. [Online]. Available: https://www.cdc.gov/niosh/docs/2013-145/default.html (visited on 06/09/2020).

[56] *Grenzwerte am Arbeitsplatz 2016*, de, Jan. 2016. [Online]. Available: https://www.bag.admin.ch/dam/bag/en/dokumente/chem/nanotechnologie/suva-grenzwerte-am-arbeitsplatz-2016.pdf.download.pdf/suva-grenzwerte-am-arbeitsplatz-2016.pdf (visited on 06/09/2020).

[57] K. Jiang, Q. Li, and S. Fan, "Spinning continuous carbon nanotube yarns," en, *Nature*, vol. 419, no. 6909, pp. 801–801, Oct. 2002, Number: 6909 Publisher: Nature Publishing Group, ISSN: 1476-4687. DOI: 10.1038/419801a. [Online]. Available: https://www.nature.com/articles/419801a (visited on 06/10/2020).

[58] K. Jiang, J. Wang, Q. Li, L. Liu, C. Liu, and S. Fan, "Superaligned Carbon Nanotube Arrays, Films, and Yarns: A Road to Applications," en, *Advanced Materials*, vol. 23, no. 9, pp. 1154–1161, 2011, _eprint: https://onlinelibrary.wiley.com/doi/pdf/10.1002/adma.201003989, ISSN: 1521-4095. DOI: 10.1002/adma.201003989. [Online]. Available: https://onlinelibrary.wiley.com/doi/abs/10.1002/adma.201003989 (visited on 06/10/2020).

[59] J. Furer, "Growth of single-wall carbon nanotubes by chemical vapor deposition for electrical devices," eng, Thesis, University of Basel, 2006. DOI: info:doi/10.5451/unibas-003935325. [Online]. Available: http://edoc.unibas.ch/diss/DissB_7505 (visited on 06/10/2020).

[60] C. Verissimo, A. L. Gobbi, and S. A. Moshkalev, "Synthesis of carbon nanotubes directly over TEM grids aiming the study of nucleation and growth mechanisms," en, *Applied Surface Science*, vol. 254, no. 13, pp. 3890–3895, Apr. 2008, ISSN: 0169-4332. DOI: 10.1016/j.apsusc.2007.12.009. [Online]. Available: http://www.sciencedirect.com/science/article/pii/S0169433207017102 (visited on 06/10/2020).

[61] M. S. Dresselhaus, G. Dresselhaus, R. Saito, and A. Jorio, "Raman spectroscopy of carbon nanotubes," en, *Physics Reports*, vol. 409, no. 2, pp. 47–99, Mar. 2005, ISSN: 0370-1573. DOI: 10.1016/j.physrep.2004.10.006. [Online]. Available: http://www.sciencedirect.com/science/article/pii/S0370157304004570 (visited on 06/10/2020).

[62] R. M. Glaeser, "Chapter Two - Specimen Behavior in the Electron Beam," en, in *Methods in Enzymology*, ser. The Resolution Revolution: Recent Advances In cryoEM, R. A. Crowther, Ed., vol. 579, Academic Press, Jan. 2016, pp. 19–50. DOI: 10.1016/bs.mie.2016.04.010. [Online]. Available: http://www.sciencedirect.com/science/article/pii/S0076687916300283 (visited on 03/20/2020).

[63] A. Bartesaghi, D. Matthies, S. Banerjee, A. Merk, and S. Subramaniam, "Structure of β-galactosidase at 3.2-Å resolution obtained by cryo-electron microscopy," *Proc Natl Acad Sci U S A*, vol. 111, no. 32, pp. 11 709–11 714, Aug. 2014, ISSN: 0027-8424. DOI: 10.1073/pnas.1402809111. [Online]. Available: https://www.ncbi.nlm.nih.gov/pmc/articles/PMC4136629/ (visited on 02/28/2018).

[64] X.-c. Bai, I. S. Fernandez, G. McMullan, and S. H. Scheres, "Ribosome structures to near-atomic resolution from thirty thousand cryo-EM particles," *eLife*, vol. 2, W. Kühlbrandt, Ed., e00461, Feb. 2013, Publisher: eLife Sciences Publications, Ltd, ISSN: 2050-084X. DOI: 10.

7554/eLife.00461. [Online]. Available: https://doi.org/10.7554/eLife.00461 (visited on 03/13/2020).

[65] A. Bartesaghi, A. Merk, S. Banerjee, D. Matthies, X. Wu, J. L. S. Milne, and S. Subramaniam, "2.2 Å resolution cryo-EM structure of β-galactosidase in complex with a cell-permeant inhibitor," en, *Science*, aab1576, May 2015, ISSN: 0036-8075, 1095-9203. DOI: 10.1126/science.aab1576. [Online]. Available: http://science.sciencemag.org/content/early/2015/05/06/science.aab1576 (visited on 01/15/2018).

[66] A. Bartesaghi, C. Aguerrebere, V. Falconieri, S. Banerjee, L. A. Earl, X. Zhu, N. Grigorieff, J. L. S. Milne, G. Sapiro, X. Wu, and S. Subramaniam, "Atomic Resolution Cryo-EM Structure of β-Galactosidase," *Structure*, vol. 26, no. 6, 848–856.e3, Jun. 2018, ISSN: 0969-2126. DOI: 10.1016/j.str.2018.04.004. [Online]. Available: http://www.sciencedirect.com/science/article/pii/S0969212618301291 (visited on 02/12/2019).

[67] M. A. Cianfrocco, I. Lahiri, F. DiMaio, and A. E. Leschziner, "Cryoem-cloud-tools: A software platform to deploy and manage cryo-EM jobs in the cloud," en, *Journal of Structural Biology*, vol. 203, no. 3, pp. 230–235, Sep. 2018, ISSN: 1047-8477. DOI: 10.1016/j.jsb.2018.05.014. [Online]. Available: http://www.sciencedirect.com/science/article/pii/S1047847718301382 (visited on 03/23/2020).

[68] P. B. Rosenthal and R. Henderson, "Optimal Determination of Particle Orientation, Absolute Hand, and Contrast Loss in Single-particle Electron Cryomicroscopy," en, *Journal of Molecular Biology*, vol. 333, no. 4, pp. 721–745, Oct. 2003, ISSN: 0022-2836. DOI: 10.1016/j.jmb.2003.07.013. [Online]. Available: http://www.sciencedirect.com/science/article/pii/S0022283603010222 (visited on 10/22/2019).

[69] J. Zivanov, T. Nakane, B. O. Forsberg, D. Kimanius, W. J. Hagen, E. Lindahl, and S. H. Scheres, "New tools for automated high-resolution cryo-EM structure determination in RELION-3," *eLife*, vol. 7, E. H. Egelman and J. Kuriyan, Eds., e42166, Nov. 2018, Publisher: eLife Sciences Publications, Ltd, ISSN: 2050-084X. DOI: 10.7554/eLife.42166. [Online]. Available: https://doi.org/10.7554/eLife.42166 (visited on 04/09/2020).

[70] S. H. Scheres, "Beam-induced motion correction for sub-megadalton cryo-EM particles," *eLife*, vol. 3, W. Kühlbrandt, Ed., e03665, Aug. 2014, Publisher: eLife Sciences Publications, Ltd, ISSN: 2050-084X. DOI:

10.7554/eLife.03665. [Online]. Available: https://doi.org/10.7554/eLife.03665 (visited on 04/07/2020).

[71] G. J. Székely, M. L. Rizzo, and N. K. Bakirov, "Measuring and testing dependence by correlation of distances," EN, *Annals of Statistics*, vol. 35, no. 6, pp. 2769–2794, Dec. 2007, Publisher: Institute of Mathematical Statistics, ISSN: 0090-5364, 2168-8966. DOI: 10.1214/009053607000000505. [Online]. Available: https://projecteuclid.org/euclid.aos/1201012979 (visited on 08/12/2020).

[72] J. Wang, "Carbon-Nanotube Based Electrochemical Biosensors: A Review," en, *Electroanalysis*, vol. 17, no. 1, pp. 7–14, 2005, _eprint: https://onlinelibrary.wiley.com/doi/pdf/10.1002/elan.200403113, ISSN: 1521-4109. DOI: 10.1002/elan.200403113. [Online]. Available: https://onlinelibrary.wiley.com/doi/abs/10.1002/elan.200403113 (visited on 04/11/2020).

[73] N. G. Portney and M. Ozkan, "Nano-oncology: Drug delivery, imaging, and sensing," en, *Anal Bioanal Chem*, vol. 384, no. 3, pp. 620–630, Feb. 2006, ISSN: 1618-2650. DOI: 10.1007/s00216-005-0247-7. [Online]. Available: https://doi.org/10.1007/s00216-005-0247-7 (visited on 04/11/2020).

[74] V. Biju, "Chemical modifications and bioconjugate reactions of nanomaterials for sensing, imaging, drug delivery and therapy," en, *Chem. Soc. Rev.*, vol. 43, no. 3, pp. 744–764, Jan. 2014, Publisher: The Royal Society of Chemistry, ISSN: 1460-4744. DOI: 10.1039/C3CS60273G. [Online]. Available: https://pubs.rsc.org/en/content/articlelanding/2014/cs/c3cs60273g (visited on 04/11/2020).

[75] R. Purohit, K. Purohit, S. Rana, R. S. Rana, and V. Patel, "Carbon Nanotubes and Their Growth Methods," en, *Procedia Materials Science*, 3rd International Conference on Materials Processing and Characterisation (ICMPC 2014), vol. 6, pp. 716–728, Jan. 2014, ISSN: 2211-8128. DOI: 10.1016/j.mspro.2014.07.088. [Online]. Available: http://www.sciencedirect.com/science/article/pii/S2211812814004532 (visited on 04/12/2020).

[76] P. C. Ma, J.-K. Kim, and B. Z. Tang, "Effects of silane functionalization on the properties of carbon nanotube/epoxy nanocomposites," en, *Composites Science and Technology*, Polymer Nanocomposites - Modeling, Mechanical and Functional Properties, vol. 67, no. 14, pp. 2965–2972, Nov. 2007, ISSN: 0266-3538. DOI: 10.1016/j.compscitech.2007.05.006. [Online]. Available: http://www.sciencedirect.com/science/article/pii/S0266353807001959 (visited on 04/12/2020).

[77] Y. Kuang and B. Huang, "Effects of covalent functionalization on the thermal transport in carbon nanotube/polymer composites: A multi-scale investigation," en, *Polymer*, Polymer Foams, vol. 56, pp. 563–571, Jan. 2015, ISSN: 0032-3861. DOI: 10.1016/j.polymer.2014.11.062. [Online]. Available: http://www.sciencedirect.com/science/article/pii/S0032386114010994 (visited on 04/12/2020).

[78] N. Nakashima, Y. Tomonari, and H. Murakami, "Water-Soluble Single-Walled Carbon Nanotubes via Noncovalent Sidewall-Functionalization with a Pyrene-Carrying Ammonium Ion," *Chem. Lett.*, vol. 31, no. 6, pp. 638–639, Jun. 2002, ISSN: 0366-7022. DOI: 10.1246/cl.2002.638. [Online]. Available: http://www.journal.csj.jp/doi/abs/10.1246/cl.2002.638 (visited on 05/18/2017).

[79] P. Hammershøj, P. H. H. Bomans, R. Lakshminarayanan, J. Fock, S. H. Jensen, T. S. Jespersen, T. Brock-Nannestad, T. Hassenkam, J. Nygård, N. A. J. M. Sommerdijk, K. Kilså, T. Bjørnholm, and J. B. Christensen, "A Triptycene-Based Approach to Solubilising Carbon Nanotubes and C60," *Chemistry – A European Journal*, vol. 18, no. 28, pp. 8716–8723, Jul. 2012, Publisher: John Wiley & Sons, Ltd, ISSN: 0947-6539. DOI: 10.1002/chem.201101189. [Online]. Available: https://chemistry-europe.onlinelibrary.wiley.com/doi/abs/10.1002/chem.201101189 (visited on 04/12/2020).

[80] T. Yamamoto, J. Motoyanagi, Y. Murakami, Y. Miyauchi, S. Maruyama, and M. Kato, "Surfactant-Stabilized Single-Walled Carbon Nanotubes Using Triphenylene Derivatives Remain Individually Dispersion in Both Liquid and Dried Solid States," en, *Appl. Phys. Express*, vol. 2, no. 5, p. 055 501, May 2009, Publisher: IOP Publishing, ISSN: 1882-0786. DOI: 10.1143/APEX.2.055501. [Online]. Available: https://iopscience.iop.org/article/10.1143/APEX.2.055501/meta (visited on 04/13/2020).

[81] J. Zhang, S. Kruss, A. J. Hilmer, S. Shimizu, Z. Schmois, F. De La Cruz, P. W. Barone, N. F. Reuel, D. A. Heller, and M. S. Strano, "A Rapid, Direct, Quantitative, and Label-Free Detector of Cardiac Biomarker Troponin T Using Near-Infrared Fluorescent Single-Walled Carbon Nanotube Sensors," en, *Adv. Healthcare Mater.*, vol. 3, no. 3, pp. 412–423, Mar. 2014, ISSN: 2192-2659. DOI: 10.1002/adhm.201300033. [Online]. Available: http://onlinelibrary.wiley.com/doi/10.1002/adhm.201300033/abstract (visited on 03/12/2018).

[82] H.-Y. Chiu, W. Deng, H. Engelke, J. Helma, H. Leonhardt, and T. Bein, "Intracellular chromobody delivery by mesoporous silica nanoparticles

for antigen targeting and visualization in real time," en, *Scientific Reports*, vol. 6, p. 25 019, May 2016, ISSN: 2045-2322. DOI: 10.1038/srep25019. [Online]. Available: https://www.nature.com/articles/srep25019 (visited on 04/12/2018).

[83] K. Jaeger, S. Bruenle, T. Weinert, W. Guba, J. Muehle, T. Miyazaki, M. Weber, A. Furrer, N. Haenggi, T. Tetaz, C.-Y. Huang, D. Mattle, J.-M. Vonach, A. Gast, A. Kuglstatter, M. G. Rudolph, P. Nogly, J. Benz, R. J. P. Dawson, and J. Standfuss, "Structural Basis for Allosteric Ligand Recognition in the Human CC Chemokine Receptor 7," English, *Cell*, vol. 178, no. 5, 1222–1230.e10, Aug. 2019, Publisher: Elsevier, ISSN: 0092-8674, 1097-4172. DOI: 10.1016/j.cell.2019.07.028. [Online]. Available: https://www.cell.com/cell/abstract/S0092-8674(19)30795-0 (visited on 04/11/2020).

[84] J. Yang, R. Yan, A. Roy, D. Xu, J. Poisson, and Y. Zhang, "The I-TASSER Suite: Protein structure and function prediction," en, *Nat Methods*, vol. 12, no. 1, pp. 7–8, Jan. 2015, Number: 1 Publisher: Nature Publishing Group, ISSN: 1548-7105. DOI: 10.1038/nmeth.3213. [Online]. Available: https://www.nature.com/articles/nmeth.3213 (visited on 04/16/2020).

[85] J. Baltrusaitis, P. M. Jayaweera, and V. H. Grassian, "XPS study of nitrogen dioxide adsorption on metal oxide particle surfaces under different environmental conditions," en, *Phys. Chem. Chem. Phys.*, vol. 11, no. 37, pp. 8295–8305, Sep. 2009, Publisher: The Royal Society of Chemistry, ISSN: 1463-9084. DOI: 10.1039/B907584D. [Online]. Available: https://pubs.rsc.org/en/content/articlelanding/2009/cp/b907584d (visited on 04/21/2020).

[86] P. R. Kidambi, B. C. Bayer, R. Blume, Z.-J. Wang, C. Baehtz, R. S. Weatherup, M.-G. Willinger, R. Schloegl, and S. Hofmann, "Observing Graphene Grow: Catalyst–Graphene Interactions during Scalable Graphene Growth on Polycrystalline Copper," *Nano Lett.*, vol. 13, no. 10, pp. 4769–4778, Oct. 2013, Publisher: American Chemical Society, ISSN: 1530-6984. DOI: 10.1021/nl4023572. [Online]. Available: https://doi.org/10.1021/nl4023572 (visited on 04/23/2020).

[87] L. Lin, H. Peng, and Z. Liu, "Synthesis challenges for graphene industry," en, *Nat. Mater.*, vol. 18, no. 6, pp. 520–524, Jun. 2019, Number: 6 Publisher: Nature Publishing Group, ISSN: 1476-4660. DOI: 10.1038/s41563-019-0341-4. [Online]. Available: https://www.nature.com/articles/s41563-019-0341-4 (visited on 04/28/2020).

[88] V. Datsyuk, M. Kalyva, K. Papagelis, J. Parthenios, D. Tasis, A. Siokou, I. Kallitsis, and C. Galiotis, "Chemical oxidation of multiwalled carbon nanotubes," en, *Carbon*, vol. 46, no. 6, pp. 833–840, May 2008, ISSN: 0008-6223. DOI: 10.1016/j.carbon.2008.02.012. [Online]. Available: http://www.sciencedirect.com/science/article/pii/S0008622308000717 (visited on 04/29/2020).

[89] H. Estrade-Szwarckopf, "XPS photoemission in carbonaceous materials: A "defect" peak beside the graphitic asymmetric peak," en, *Carbon*, vol. 42, no. 8, pp. 1713–1721, Jan. 2004, ISSN: 0008-6223. DOI: 10.1016/j.carbon.2004.03.005. [Online]. Available: http://www.sciencedirect.com/science/article/pii/S0008622304001629 (visited on 04/29/2020).

[90] A. Siokou, F. Ravani, S. Karakalos, O. Frank, M. Kalbac, and C. Galiotis, "Surface refinement and electronic properties of graphene layers grown on copper substrate: An XPS, UPS and EELS study," en, *Applied Surface Science*, vol. 257, no. 23, pp. 9785–9790, Sep. 2011, ISSN: 01694332. DOI: 10.1016/j.apsusc.2011.06.017. [Online]. Available: https://linkinghub.elsevier.com/retrieve/pii/S0169433211008786 (visited on 04/23/2020).

[91] U. Zielke, K. J. Hüttinger, and W. P. Hoffman, "Surface-oxidized carbon fibers: I. Surface structure and chemistry," en, *Carbon*, vol. 34, no. 8, pp. 983–998, Jan. 1996, ISSN: 0008-6223. DOI: 10.1016/0008-6223(96)00032-2. [Online]. Available: http://www.sciencedirect.com/science/article/pii/0008622396000322 (visited on 04/28/2020).